CENTRO DE INVESTIGACIÓN Y DE ESTUDIOS AVANZADOS DEL INSTITUTO POLITÉCNICO NACIONAL

Unidad Mérida

DEPARTAMENTO DE FÍSICA APLICADA

"Effect of the selective contacts on the performance of hybrid perovskite solar cells"

a thesis submitted by:

Karen Lizbeth Valadez Villalobos

In partial fulfillment of the requirements for the degree of

Doctor of Science

in

Physical Chemistry

Thesis Advisor:

Dr. Gerko Oskam

Mérida, Yucatán, México June 2019

CENTRO DE INVESTIGACIÓN Y DE ESTUDIOS AVANZADOS DEL INSTITUTO POLITÉCNICO NACIONAL

Unidad Mérida

DEPARTAMENTO DE FÍSICA APLICADA

“Efecto de los contactos selectivos en el desempeño de las celdas solares de perovskita híbrida”

TESIS

Que presenta

Karen Lizbeth Valadez Villalobos

Para obtener el grado de

Doctora en Ciencias

en

Fisicoquímica

Director de Tesis:

Dr. Gerko Oskam

Mérida, Yucatán, México Junio de 2019

AGRADECIMIENTOS

Al Consejo Nacional de Ciencia y Tecnología (CONACYT), por apoyar mi formación a través de los financiamientos otorgado mediante las becas de maestría y doctorado así como mediante la beca de movilidad al extranjero y el programa Fronteras de la Ciencia Grant FDC-2015-110.

Al CINVESTAV Mérida, sus profesores y demás miembros, por haberme brindado las herramientas necesarias para impulsar mi formación.

Al Dr. Gerko Oskam, por su excelente asesoría y por su gran apoyo y paciencia durante todo el doctorado.

Al Dr. Juan Anta y al Dr. Jesús Idígoras, de la Universidad Pablo de Olavide en Sevilla, España y a la Dra. Petra Cameron de la Universidad de Bath, en Reino Unido, por el amable recibimiento que me otorgaron y por el enorme aprendizaje obtenido durante las estancias en sus respectivos grupos de investigación.

Al comité de sinodales compuesto por el Dr. Geonel Rodríguez Gattorno, el Dr. Juan José Alvarado Gil, la Dra. Inés Margarita Riech Méndez y la Dra. Petra Cameron, por sus valiosas aportaciones y comentarios a mi trabajo de tesis doctoral.

A los integrantes del grupo de Nanomateriales por el excelente compañerismo y apoyo profesional.

A mi familia, a Rodrigo y a mis amigos, por el amor, la generosa paciencia y la motivación constante que me han dado durante estos años.

ABSTRACT

Hybrid organic-inorganic metal halides with the perovskite structure are a family of materials that have been studied since the 1970s, however, it was until 2009 when they were first applied as sensitizers in photovoltaic devices, and the field of research dedicated to hybrid perovskite solar cells (PSCs) was born. Since then, the extensive research dedicated to the improvement and understanding of PSCs has resulted in laboratory-scale efficiencies comparable to those of well-established technologies such as silicon and CdTe.

An interesting aspect of the PSC is that high efficiencies have been obtained for a variety of device architecture, including planar, mesoscopic, and triple-stack configurations. In addition, the chemical compositions of the hybrid perovskite has been evolving rapidly, where methyl ammonium lead iodide ($MAPbI_3$) represents the standard structure, but where both methyl ammonium iodide and have been partially replaced by other organic molecules and halides. The hybrid perovskite is the light absorbing material, which is sandwiched between an electron and hole selective contact, respectively, with a transparent conducting oxide (TCO) on one side and a metal contact on the other to complete the solar cell. We can differentiate between two main designs for hybrid perovskite devices as a function of the order in which the selective contacts are deposited: (i) the n-i-p configuration, being the conventional device, where the electron selective contact (ESC), typically a mesoporous or a compact film of TiO_2, is deposited first on the TCO, followed by the perovskite absorber material and the hole selective contact; and (ii) the p-i-n or inverted device, where the hole selective contact is deposited first onto the TCO followed by the perovskite absorber and the ESC.

Although the highest efficiency achieved by PSCs corresponds to conventional mesoporous device, both types of devices have surpassed the 20% of efficiency on the laboratory scale. Despite the impressive efficiencies, the commercialization of PSCs, however, remains hindered by issues related to the chemical instability of the perovskite material under operating conditions and in the presence of humidity. Further improvement of the devices demands a deeper knowledge of the working mechanisms of PSCs. As a part of this effort, the systematic study of the device mechanisms and the role of each of its components are very relevant to impulse this technology to a superior performance and stability.

In this work we have investigated the role of the selective contacts in conventional and inverted PSCs. As a part of this study, different n-type materials were studied as electron selective contacts in the regular n-i-p configuration of mesoscopic PSCs. The materials studied as electron selective contacts were the three crystalline phases of TiO_2 (anatase, rutile and brookite) and zinc stannate (ZTO) synthesized in our laboratory, as well as commercial alumina (Al_2O_3) and zirconia (ZrO_2). For the inverted system, the study was focused on comparing the planar with the mesoporous morphology of the p-type oxide NiO_X, as the hole selective contact.

We have applied electrochemical impedance spectroscopy, a small perturbation technique that allows us to discern between processes taking place at different time constants, to investigate the effect that changing the electron selective contact or the hole selective contact has on the electronic recombination dynamics and low frequency processes observed in these devices.

A curious characteristic of the PSC is the observation of a hysteresis in the current – voltage curve at the typical scan rates used for the characterization of solar cells. In this work, the hysteric behavior of the devices was characterized for conventional and inverted devices, and the results are compared. The results suggest that the different charge separation properties at the electron-selective contact and the hybrid perovskite interface have a strong impact on the hysteresis and the short-circuit current, but that the effect on the open circuit voltage is small, except for less efficient electron selective contacts. For the inverted system, optimized mesoporous and planar devices share a similar performance, and the results suggest that the hysteresis response seems to be related to the configuration of the device. Conventional devices showed a hysteric behavior commonly reported for PSCs, where sweeping the cell voltage from open-circuit conditions to short circuit conditions (reverse scan) presents a higher performance. On the other hand, the inverted devices predominantly showed the opposite behavior, with the best performance is obtained for the sweep performed from short circuit conditions to the open-circuit voltage. From these results we conclude that the configuration of the devices plays an important role in the hysteric behavior, which probably originates from different interactions at the hybrid perovskite - electron selective contact. In the conventional configurations, this is the TiO_2 - MAPI interface, while in the inverted configuration the electron selective contact is PCBM (Phenyl-C61-butyric acid methyl ester).

In conclusion, the effect of electron selective contacts in hybrid perovskite solar cells has been investigated in two different configurations, resulting in information on the electronic processes than dominate recombination, as well as on ion migration processes that determine the hysteretic behavior of the solar cells.

RESUMEN

Los halogenuros metálicos híbridos inorgánicos-orgánicos con estructura tipo perovskita son una familia de materiales que han sido estudiados desde la década de 1970, sin embargo, fue hasta el año 2009 cuando, tras ser aplicados por primera vez como sensibilizadores en dispositivos fotovoltaicos, surgió el campo de investigación dedicado al estudio de celdas solares de perovskitas híbridas (CSP). A partir de entonces, la extensa investigación dedicada a la mejora y el entendimiento de las CSP ha resultado en eficiencias a escala de laboratorio comparables con tecnologías bien establecidas como la del silicio y el CdTe.

Un aspecto interesante de las CSP es la obtención de altas eficiencias para una variedad de arquitecturas de los dispositivos, incluyendo la configuración planar, la configuración mesoscópica y la configuración de triple capa. Adicionalmente, la composición química de la perovskita híbrida ha tenido una rápida evolución a partir de la composición estándar, el yoduro de plomo metilamonio ($MAPbI_3$), comúnmente conocido como MAPI, obtenido mediante la sustitución parcial del metilamonio (MA) y del yoduro con otras moléculas orgánicas y otros haluros. En las CSP, la perovskita híbrida es el material que absorbe la luz, el cual es depositado entre dos capas selectivas que cumplen la función de extracción de electrones y huecos, respectivamente, intercalados entre un óxido conductor transparente (OCT) por un lado y una contacto metálico por el otro. En base al orden en el que los contactos selectivos son depositados, es posible identificar dos diseños para los dispositivos de perovskitas híbridas: (i) la configuración n-i-p, el dispositivo convencional, donde el contacto selectivo de electrones, típicamente una capa compacta o mesoporosa de TiO_2, es depositado primero en el OCT, seguido por la perovskita como material absorbente y el

contacto selectivo de huecos; y (ii) el dispositivo p-i-n, también conocido como el dispositivo invertido, donde el material selectivo de huecos es depositado primero sobre el OCT seguido por la perovskita y el contacto selectivo de electrones.

Aunque la eficiencia más alta alcanzada para CSP corresponde a los dispositivos convencionales mesoporosos, ambos tipos de celdas han superado el 20% de eficiencia a escala de laboratorio. A pesar de las altas eficiencias, la comercialización de las CSP está limitada por problemas relacionados con la inestabilidad química del material de perovskita bajo condiciones de operación y en la presencia de humedad. La mejora adicional de los dispositivos requiere un conocimiento más profundo de los mecanismos de funcionamiento de las CSP. Como parte de este esfuerzo, un estudio sistemático de los mecanismos de funcionamiento y del papel que cada uno de los componentes tiene en el funcionamiento de las celdas solares es de gran relevancia para impulsar esta tecnología hacia una mayor eficiencia y estabilidad.

En este trabajo, hemos investigado el papel de los contactos selectivos en CSP convencionales e invertidas. Como parte de este estudio, diferentes materiales tipo n fueron estudiados como contactos selectivos de electrones en la configuración n-i-p de CSP mesoscópicas. Los materiales estudiados como contactos selectivos de electrones fueron las tres fases cristalinas del TiO_2 (anatasa, rutilo y brookita) y el estanato de zinc, todos ellos sintetizados en nuestro laboratorio, así como la alúmina (Al_2O_3) y la zirconia (ZrO_2), ambos materiales obtenidos de fuentes comerciales. Para el sistema invertido, el estudio se enfocó en la comparación de las morfologías planar y mesoporosa del óxido tipo p, NiO_X, como la capa selectiva de huecos.

Para investigar los efectos de la variación de los contactos selectivos de electrones y huecos en la dinámica de recombinación y en los procesos a baja frecuencia que se observan en las CSP, hemos empleado como técnica de caracterización la espectroscopía de impedancia electroquímica, una técnica de pequeña perturbación que permite discernir entre procesos que ocurren a diferentes constantes de tiempo.

Una característica peculiar de las CSP es la presencia de histéresis en la curva de corriente-voltaje a las velocidades de barridos usualmente utilizadas para la caracterización de celdas solares. En este trabajo, el comportamiento histerético de los dispositivos fue caracterizado para celdas convencionales e inversas y los resultados fueron comparados. Los resultados sugieren que los diferentes efectos asociados a la separación de carga que ocurre en la interfaz entre el contacto selectivo de electrones y la perovskita híbrida, tienen un fuerte impacto en la histéresis y en la corriente de corto circuito, mientras que el efecto en el voltaje de circuito abierto es pequeño, excepto en el caso de los contactos selectivos de electrones menos eficientes. Para el sistema invertido, los dispositivos planos y mesoporosos mostraron un desempeño similar, además de que la histéresis parece estar relacionada con la configuración del dispositivo. Los dispositivos convencionales mostraron un comportamiento histerético comúnmente reportado para CSP, donde el barrido del voltaje desde condiciones de circuito abierto a condiciones de corto circuito (barrido inverso) resulta en un mayor desempeño que el barrido en dirección contraria. Por otro lado, los dispositivos invertidos mostraron predominantemente un comportamiento opuesto, con un mejor desempeño obtenido para el barrido de voltaje desde condiciones de corto circuito a condiciones de circuito abierto. De estos resultados concluimos que la configuración de los dispositivos juega un papel importante en el comportamiento

histerético, el cual tiene un origen probable en las diferentes interacciones entre la perovskita híbrida y el contacto selectivo de electrones. En la configuración convencional esto se refiere a la interfaz TiO_2 – $MAPbI_3$, mientras que en la configuración invertida, el contacto selectivo de electrones es el compuesto PCBM (Fenil-C61-ácido butírico metil éster).

En conclusión, se ha investigado el efecto de los contactos selectivos en dos diferentes configuraciones de celdas solares de perovskita híbrida, resultando en información acerca de los procesos electrónicos que dominan la recombinación así como de los procesos de migración iónica que determinan el comportamiento histerético de estas celdas solares.

TABLE OF CONTENTS

INDEX OF FIGURES

INTRODUCTION

The burning of fossil fuels that supplies more than 80% of the global energy demand has already caused great damage to the environment, and the effects of its accumulation will continue to manifest for decades, even if the most extreme measures against climate change are applied immediately. In addition, the global energy demand continues to increase in an exponential way, making of the fulfilment of this demand in a secure and sustainable way, free of greenhouse gasses emissions, one of the biggest challenges that humanity will face over the next decades. In this respect, the application of scientific research for the exploitation of alternative sources of energy is extremely relevant, along with modifications of environmental policies and international cooperation, as a part of the transition from fossil fuels to clean sources of energy.

Although solar power is one of the fastest growing renewable energies, it remains severely underexploited. In the field of photovoltaics, the current market is dominated by silicon-based devices, a well-established technology that has been studied for decades. Emerging photovoltaic technologies, such as dye-sensitized solar cells (DSSCs) and organic photovoltaics (OPVs), have been studied as an alternative to the high-priced processes of the silicon technology but issues related to long term stability and lower efficiencies have prevented their commercialization to a higher scale.

Recently, a new type of solar cells based on hybrid organic-inorganic metal halides with perovskite structure have gained a great attention. As an emerging technology, it was

attractive due to the relatively simple solution-based methods of fabrication that required low-temperature conditions and cheap abundant materials. A decade after its emergence, the rapid rise in reported efficiencies, actually surpassing the 20%, have placed perovskite solar cells as the leading emerging PV technology.

There are important matters to address before the commercialization of this PSCs, namely the issue of the chemical stability and the anomalous hysteresis in the current-potential curves, which difficults the precise evaluation of their performance, as well as issues related to the toxicity of Pb.

In this work, we have focused on clarifying the effect of the selective contacts that allow for charge separation in PSCs by either varying the composition or the morphology of electron or hole selective contacts in conventional and inverted perovskite devices.

The contents of this work begin with a general overview of the current state of energy supply, climate change, and the transition to renewables in Chapter 1. Chapter 2 is a general chapter of basic concepts related to the field of photovoltaics and a descriptive section of the several generations of photovoltaics. Chapter 3 contains a review of the emergence and evolution of perovskite solar cells as well as a survey of the results and theories developed to explain the working mechanisms and the anomalies of these devices. The methodology followed during the experiments is detailed in chapter 4. The findings and conclusions of the work performed on conventional and inverted perovskite solar cells are described in Chapters 5 and 6, respectively. Finally, a brief summary and general conclusions are contained in the final section.

CHAPTER 1. ENVIRONMENTAL IMPACT AND THE TRANSITION TO SUSTAINABLE SOURCES OF ENERGY.

Introduction

Energy resources are crucial for the survival and development of humankind; historically, the transition to different energy sources has deeply affected the economic dynamics, transforming human societies and modifying the environment.

Comparable to the transformation brought by agriculture to nomadic societies, the industrial revolution caused a deep transformation of our civilization. In 1800, 70% of the total energy demand was still supplied by man.[1] A century later, the internal combustion engine, a machine fueled by oil, was capable of producing the work equivalent of 6000 men. This radical change prompted the beginning of mass production and transformed the economy. A complex set of events related to the changes in economy caused the accelerated growth in the population and promoted an increase in individual energy consumption. Every aspect of quotidian life in Europe was eventually transformed by the industrial revolution during the following decade and, by giving place to the global dominance of fossil fuels as the main source of energy, those transformations eventually extended worldwide. Expressed in numbers, the population went from 1 billion in 1820 to the actual population of 8 billion; as for the increase in energy consumption, Figure 1 shows the increase in the consumption per capita and the related increase in the total net consumption for the last two centuries, evidencing the exponential growth that took place after the industrialization. [2]

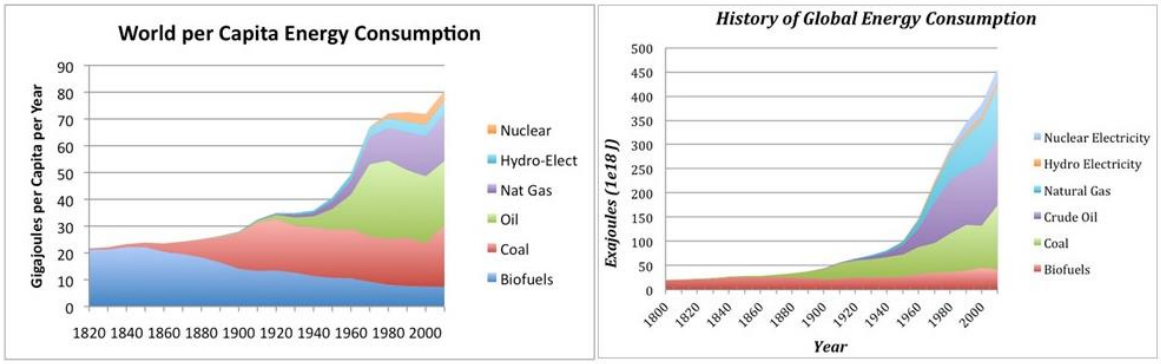

Figure 1. Historical evolution of per capita (left) and global (right) energy demand by energy source (Smil, V. " Energy Transitions: History, Requirements, Prospects″).

Although the sources of energy mainly used today, fossil fuels, are non-renewable, there is proof that there are enough reserves to keep satisfying the projected demand in energy for many decades in the case of oil, and even centuries in the case of coal. However, as described in the next section, rather than the eventual depletion of fossil fuels, the most pressing matter motivating the search of alternative sources of energy is related to the danger they represent to the environment.

1.1 Human activity and global warming

The 20th century was a century of accelerated change. It had taken 2000 years for the population to grow from approximately 200 million people to 1 billion by 1820, and it required only two centuries to reach almost 8 billion people. There was also an unprecedented advancement in science and technology, a certain measure of the increase in public wealth with education and health available to more people.

The frantic changes of the 20th century came without a defined plan for the handling of residues and emissions generated by the growing industry and population, although there were some efforts to create awareness about thresholds in terms of environment alteration

that would set about changes in the conditions that have been prevalent for millennia, the awareness was not integrated into control or contingency plans for the consequences we are facing today.

As the Earth moved out of ice ages over the past million years, the global temperature rose a total of 4 to 7 degrees Celsius over about 5,000 years. In the past century alone, the temperature has climbed 0.7 degrees Celsius, roughly ten times faster than the average rate of ice-age-recovery warming. [3] This is related to the concentration of carbon dioxide in the earth atmosphere (Figure 2).

Weather fluctuations have happened several times throughout the history of the earth without the influence of human activity, however, there is an overwhelming amount of evidence pointing to the human activity as responsible for the current rise in CO_2 concentration levels and the associated global warming due to the greenhouse effect.

The accumulating evidence pointing human activity as a cause for climate change and the present and estimated consequences of continuing in the same fashion have motivated the creation of international forums where hundreds of international leaders strive to agree on collective measures against the advancement of this problem.

In 1988, the International Panel on Climate Change was established, endorsed by the United Nations General Assembly, to deliver periodical evaluations on climate change, its potential impact on economic, environmental and political aspects and to provide possible response options. The periodical reports published by the IPCC are relevant to understand the risk of human-induced climate change, its potential impacts, and options

for adaptation and mitigation by reviewing the available scientific and socio-economic studies available on this matter.

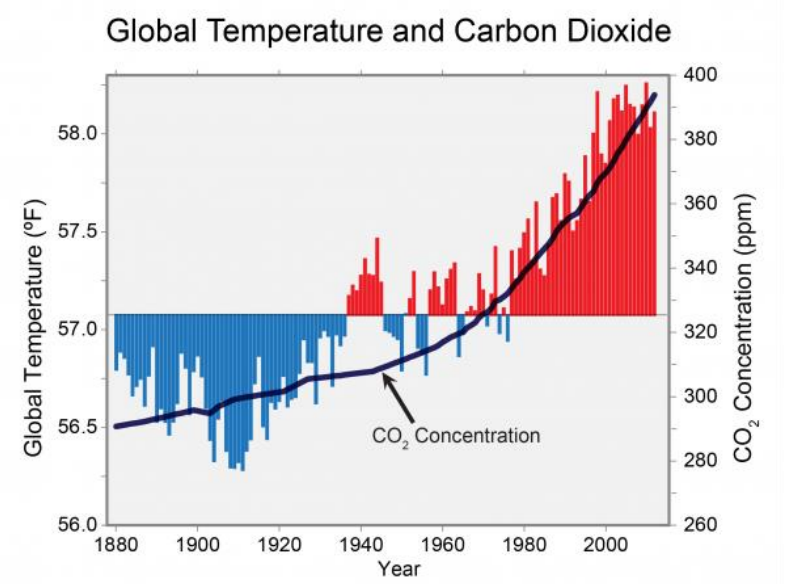

Figure 2. Global annual average temperature (as measured over both land and oceans) has increased by more than 1.5°F (0.8°C) since 1880 (through 2012). Red bars show temperatures above the long-term average, and blue bars indicate temperatures below the long-term average. The black line shows atmospheric carbon dioxide (CO_2) concentration in parts per million (ppm) (Melillo, "*Climate change impacts in the United States: the third national climate assessment"*)

According to the IPCC reports, to limit global warming to 1.5 °C above pre industrial levels, the world would have to curb its carbon emissions by 50% of 2017 levels by 2030 and achieve carbon neutrality by 2050. It is estimated that, if no major reductions in greenhouse gas emissions are made, global warming could reach 1.5 °C in the next 10 to 30 years, and around 3 °C of warming by the end of the century. The narrow margins in temperature have a great impact on our environment. The arctic could experience ice-free Summers once every decade if the temperature rises 2 °C, versus once in a century if the temperature rises 1.5 °C. [5]

Regarding the action taken around the IPCC reports, the Paris agreement was a milestone in international cooperation towards the reduction of carbon dioxide emissions in order to allow for a sustainable future. Under the Paris Agreement, each country must determine, plan, and regularly report on the contribution that it undertakes to mitigate global warming. [6]

The measures suggested by the IPCC to limit global warming to 1.5 °C, include increasing the installation of renewable energy sources such as wind and solar power to provide between 70%-85% of the world´s electricity by 2050. Clean sources of energy are already a part of global consumption, and the percentage of their use has increased in the last decade however, the percentage of global energy demand fulfilled with oil and carbon has remained almost constant for the last 15 years as observed in Figure 3. Mexico presents the same trend for the last fifteen years, with coal and oil providing 85 % of the national energy consumption (Figure 4). This means that the international agreements have not yet resulted in any reduction in the emission of greenhouse gasses and puts more pressure in an immediate transition to clean, renewable sources of energy in order to avoid the aggravation of the environmental impact.

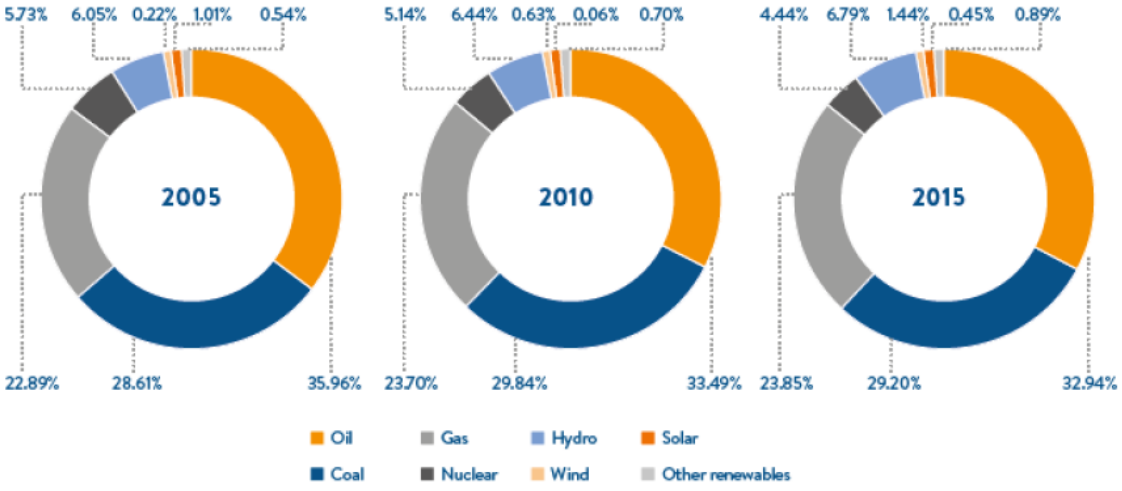

Figure 3. Comparative primary energy consumption over the past 15 years ("*La industria solar fotovoltaica y fototérmica en México," SENER)*.

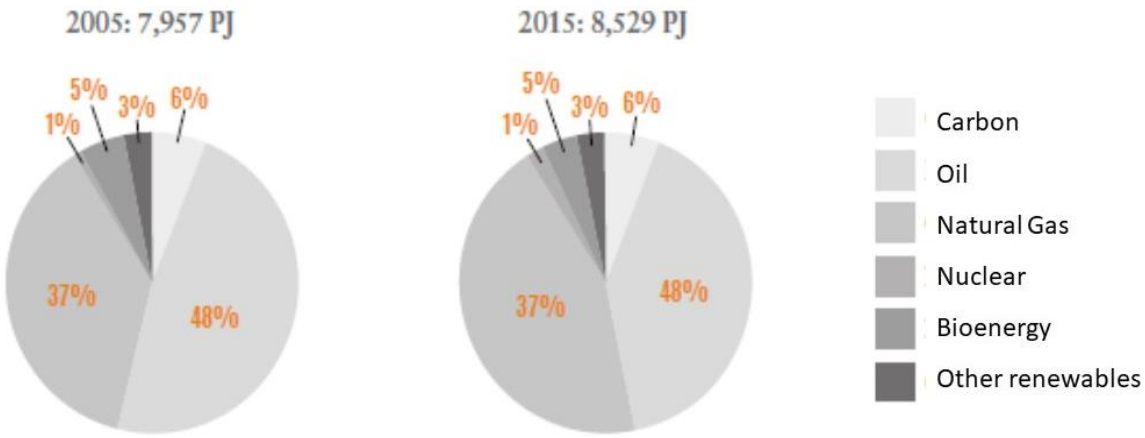

Figure 4. Comparative energy consumption in Mexico during 2005 and 2015 (SENER).

1.2 Solar energy

Among the renewable energy resources, solar energy has the largest potential to satisfy the future global need for energy; it is the most abundant energy source on planet Earth, with the theoretical potential of solar power being estimated at 89,300 TW. However, only a very small proportion (less than 1%) of the global energy supply comes from solar energy.

Large scale placement of solar photovoltaic technologies has been hindered by production costs, material availability and material toxicity.

According to the 2018 United Nations report: Global Trends in Renewable Energy, the investment in solar energy has seen an exponential growth; it accounted for 1% of the electricity used globally in 2015. The major installations correspond to countries with relatively less solar resources while high resources regions like Middle East, Africa and Latin America, remain severely underexploited.

Changes in policy and an increase in the offer of solar panels have resulted in a decrease in prices. Between 2007 and 2014, PV module prices declined by around 79%; the biggest yearly reduction was seen in 2011, of around 40% from 2010[7]. Figure 5 shows that from 2010 to 2015, solar PV technology prices had the highest drop when compared to the rest of renewable energy sources such as wind and solar to thermal conversion.

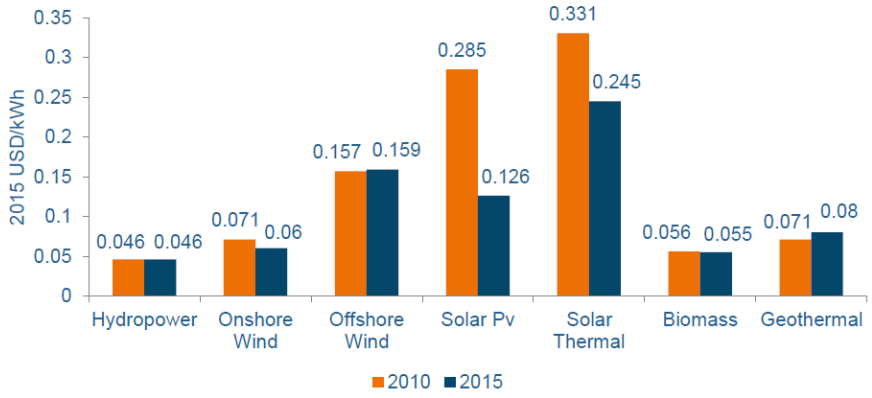

Figure 5. Price changes per source of energy from 2010 to 2015.

In Mexico, the Bureau of Energy (SENER) has established several goals concerning the participation of renewable energies in the following years. According to these goals, 30%

of the total energy consumption in Mexico should be supplied by clean energy sources by 2021 and 35% by 2024. In addition, the Bureau for the Environment and Natural Resources (SEMARNAT) has committed to the reduction of 22% of greenhouse gases and 51% of the black carbon emissions by 2030.[8]

The policy around these goals has included a reform in the regulation of solar energy use that has made it more attractive for the industrial and residential market. An investment of 4,500 million dollars was made in 2015 in a total of 28 contracts for photovoltaic installations. These are expected to begin commercial operation in 2019, increasing the photovoltaic capacity to 3,544 MW. [9]

CHAPTER 2. PHOTOVOLTAICS

2.1 Basic concepts of semiconductors

To understand the principles of the arrangement of atoms in solids, it is useful to look at the more basic case of a molecule. When two atoms come together to form a molecule, their atomic orbitals combine to form pairs of molecular orbitals arranged slightly higher and slightly lower than their original levels. This is called splitting of the energy levels. A solid is conformed by a large number of atoms so that every molecular orbital has to split into a large number of similar energy levels. The energy levels are so closely spaced that they form a continuum called band (Figure 6).[10]

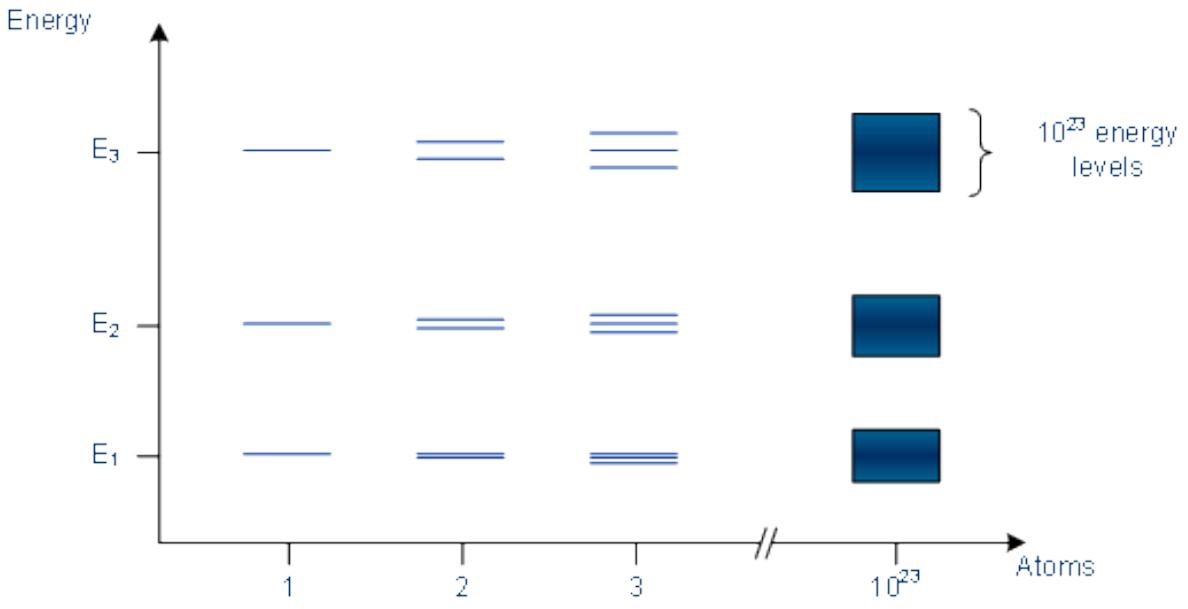

Figure 6. As the number of atoms in a molecule or cluster increases, atomic orbitals split into multiple levels, eventually giving place to bands.

Bands are occupied or not depending upon whether the original level was occupied in the atom. The highest occupied band, which contains the valence electrons, is called the

valence band, while the lowest unoccupied band is called the conduction band. Depending on the distribution of these bands, a material exhibits metallic, semiconductor or insulator properties.

In insulators, the electrons in the valence band (VB) are separated by a large gap from the conduction band (CB); in conductors such as metals, the valence band overlaps with the conduction band; and in semiconductors there is a small enough gap between the valence and conduction bands for thermal or light-induced excitations to bridge the gap.

Figure 7 shows a schematic representation of the different types of materials depending on the width of their band gap (E_g). The Fermi level (E_F) can be modified by the addition of electrons or holes through a process called doping. The addition of electrons, called n-type doping, shifts the E_F closer to the conduction band while the addition of holes or p-type doping shifts the E_F closer to the valence band. The addition of electrons or holes caused by doping increases the carrier concentration and it is therefore a technique used in photovoltaics to improve the properties of some semiconductor materials.

For semiconductors, the onset of the absorption spectrum is at the energy of the bandgap (E_g). In an ideal semiconductor, only photons with energy higher than E_g are absorbed by promoting an electron from the valence to the conduction band and leaving a hole in the valence band.

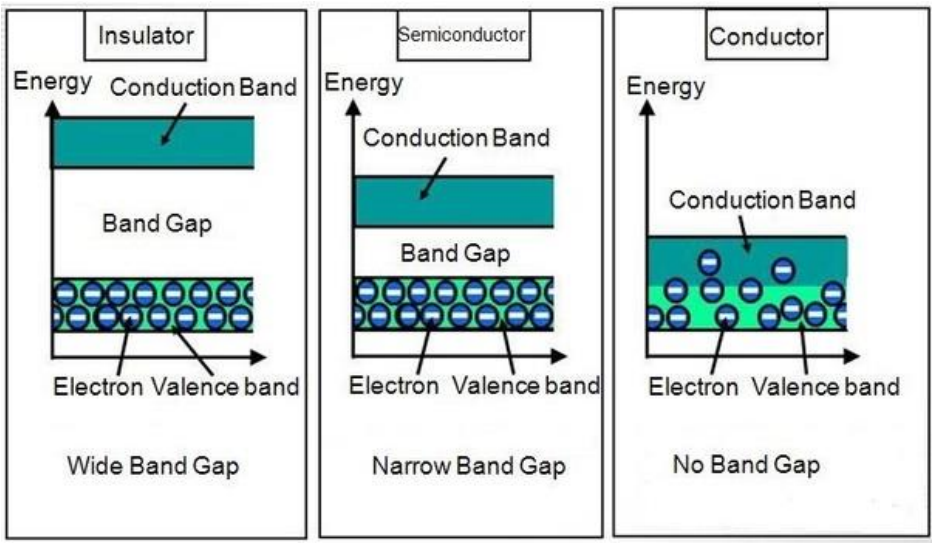

F**igure 7.** Representation of metal, semiconductor and insulator materials according to their band diagram.

2.2. Semiconductors and photovoltaics

Incident photons with lower energies than the E_g are transmitted while absorbed photons with much higher energy than the E_g promote an electron to a level located higher in the conduction band and generate a hole located deeper in the valence band, compared to the band edges. However, the electrons and holes relax quickly, in the scale of picoseconds, to the band edge due to energy transfer to phonons. This fast process assisted by phonons is called thermalization. Consequently, the higher the bandgap, the lower are the overall thermalization losses. When tuning the bandgap to reach high efficiency, there is a trade-off between harvesting as many photons as possible and maximizing the energy of extracted charges.

Although the short-circuit current in a cell is determined by how strongly light is absorbed and the success of the charge carriers photo-generated to reach the electrical contacts, the power output of the cell is determined by the product of the current and the voltage. It is

therefore important to understand the conditions required to reach high voltages and this is related to more complex mechanisms related to the photovoltaic device structure.

2.3 Principles of photovoltaic devices and characterization of their performance.

2.3.1. Light absorption

When light is absorbed by matter, the photon energy is used to excite electrons to higher energy states within the material; the negative charge carrier is the excited electron and the positive charge carrier is the hole left by the electron after excitation; the density of electron-hole pairs depends on the nature of the absorber material.

Not all matter interacts with light to generate charge carriers. For a material to be of potential application in solar cells, it must possess an adequate bandgap. More specifically, its bandgap must be in the order of sunlight energy. A band gap between 1.0 and 1.7 eV makes an effective solar semiconductor. In this range, electrons can be freed without creating too much heat.

There is a trade-off between the number of photons available for absorption and the fraction of the photon's energy which is used in a solar cell. Both are limited by the semiconductor's bandgap. The bandgap of a semiconductor determines the available fraction of the solar spectrum for absorption, while the probability of each electronic transition happening at a given wavelength is described by the material's absorption coefficient.

The standard solar spectrum at the Earth's surface (AM1.5) used for the characterization of solar cells is shown in Figure 8. The attenuation by the atmosphere is quantified by the air mass (AM) factor AM1.5 corresponds to the Sun's elevation angle of 42 º. The Sun's spectrum (AM1.5) can be approximated by the black body radiation spectrum at 5760 K. The AM1.5 spectrum is normalized to match the irradiance of 1000 W/m^2.

The theoretical maximum current density (J_{max}) achievable by each absorbing material can be derived from the following equation.

$$J_{max} = q \int_{E_g}^{\infty} \Phi_{ph}^{\mathrm{AM1.5}}(E) dE \qquad (2.1)$$

where q is elemental charge and $\Phi_{ph}^{\mathrm{AM1.5}}(E)$ is photon flux density at a given wavelength.

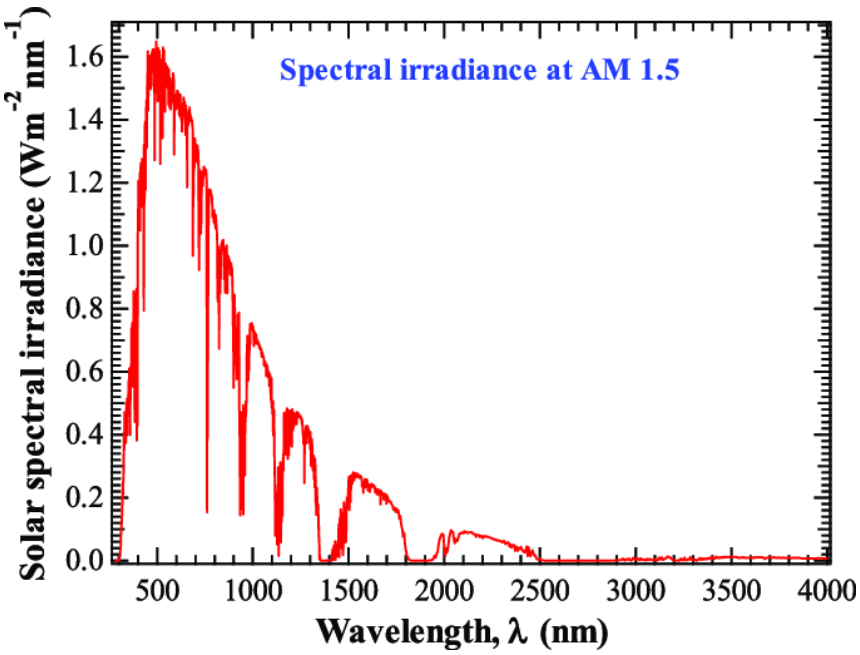

Figure 8. Solar spectrum for direct global irradiance (AM1.5).

The thickness of a semiconductor layer required to completely absorb all the photons with an energy equal to or higher than the semiconductor bandgap is a function of the semiconductor absorption coefficient. This characteristic of the semiconductor determines the thickness required to absorb enough light; increasing the thickness of a material introduces additional challenges to efficient transport and collection of photogenerated charges so that a material with a high absorption coefficient is desirable.

Following light absorption, electron-hole pairs called excitons can be formed. In an exciton, the charge carriers remain bound by Coulombic attraction. The binding energy of the coupled charges varies between materials and primarily depends on the dielectric constant of the semiconductor. Inorganic crystalline semiconductors, such as silicon, or gallium arsenide (GaAs) have high dielectric constants (11.9 and 13.1 for Si and GaAs, respectively), which allows for effective screening of the electrostatic attraction between bound electron and hole and hence a small exciton binding energy.[11]

2.3.2 Charge separation and recombination

In a photovoltaic device, the absorber material is connected to an external circuit in an asymmetric manner.[12] The asymmetry of the configuration allows for charge separation. The asymmetry in photovoltaics devices is achieved through a heterojunction where the active material is sandwiched between two uniform layers of a charge selective material that acts as electron and hole selective contact, respectively. The selectivity is provided by choosing a material of appropriate energy bandgap and electron affinity, which allows only one type of carrier to be efficiently transferred across the interface towards the electrode, while blocking the other type of carrier.

A good alignment of the Fermi levels between the light harvesting materials and the selective contacts is key to achieve a good performance of the devices. If charge extraction is not very effective, carriers build up at the interface, which leads to increased recombination. The adequate selection of selective contacts is vital to minimize charge losses.

Recombination is a limiting factor to the performance of solar cells and refers to the loss of photogenerated carriers that are not extracted from the device as photocurrent. Some recombination processes relate to the thermodynamic principles of the solar cell and are unavoidable even in an ideal device. An example of these processes is the radiative form of recombination called photoluminescence. This process occurs by direct recombination between an electron in the conduction band and a hole in the valence band, where the excess energy produced by this interaction is released as a photon.

Charge recombination rate. A longer carrier recombination lifetime is needed for larger open circuit voltage, $V_{OC,}$ because it enables a higher carrier concentration (or a larger quasi-Fermi level splitting) for solar cells under illumination. The charge recombination in a semiconductor material can be described by the following equation:[13]

$$\frac{dn}{dt} = G - k_1 n - k_2 n^2 - k_3 n^3 \qquad (2.2)$$

where G is the charge generation rate, k_1 is the monomolecular charge recombination rate constant, k_2 is the bimolecular charge recombination rate constant, k_3 is the Auger charge recombination rate and n is the charge density.

Auger recombination is another intrinsic process where electron and hole interact with each other, resulting in annihilation of both carriers and an increase in the kinetic energy of a third carrier. This type of recombination is relevant for low bandgap materials and becomes dominant at high charge densities. The Auger charge recombination is generally weak compared with other recombination channels at normal solar cell operating conditions (that is, under 1 sun illumination with a carrier concentration of 10^{15}–10^{16} cm^{-3}).

The avoidable recombination processes are usually related to the existence of electronic trap states within the absorber and at the interfaces between the absorber and charge-selective contacts. The origin of these trap stated can be crystallographic defects or surface states. Shallow trapped carriers can engage in a large number of trapping and detrapping cycles, influencing the mobility of the carriers; this is detrimental for the efficiency of charge extraction. Deeply trapped carriers are permanently immobilized, and eventually recombine with oppositely charged carriers in a non-radiative process, giving away the excess of energy as heat. For a good solar cell operation, non-radiative recombination should be limited to the minimum.[11]

2.3.3 Solar cell performance

Solar cells behave like a diode in the dark, displaying rectifying behavior, which means that the current flow only occurs in one direction when forward bias is applied (V is higher than 0); the current is blocked under reverse bias conditions (V is less than 0). The dark current in an ideal case is described by the ideal diode equation given below:

$$J_d(V) = J_0\left(e^{qV/k_BT} - 1\right) \quad (2.3)$$

where J_0 is a saturation current, k_B is the Boltzmann constant, T is the absolute temperature and V is a voltage bias applied to the electrodes. Under illumination, when a load is applied to the cell terminals, the potential difference between the electrodes opposes the electrochemical potential gradient resulting from the photogeneration. The reverse current driven by the potential bias can be approximated by the diode's dark current. Therefore, the net current produced by the solar cell is the difference between the photocurrent and the dark current and for an ideal diode model, this is given by the following equation:

$$J = J_{SC} - J_d(V) = J_{SC} - J_0\left(e^{qV/k_BT} - 1\right) \quad (2.4)$$

where J_{SC} is a short-circuit current density.

When there is no load applied (V=0 and J_d=0), the net current of the device comes only from the photogenerated charges, and this is called the short-circuit current density (J_{SC}). When the applied bias is high enough, the photocurrent is equal to the dark current, and the cell is in open-circuit condition. The voltage required to cancel out the electrochemical potential gradient of charge carriers in the device induced by illumination is termed open-circuit voltage (V_{OC}), and can be described by Equation:

$$V_{OC} = \frac{k_BT}{q}\ln\left(\frac{J_{SC}}{J_0} - 1\right) \quad (2.5)$$

An example of the solar cell's current density-voltage (*JV*) characteristics, in dark and under illumination, is shown in Figure 9. The parameters that are used for assessing photovoltaic performance, and that can be extracted from the *JV* curve include: J_{SC}, V_{OC}, fill factor (*FF*), and power conversion efficiency (*PCE*).[12]

$$FF = \frac{J_{max}V_{max}}{J_{SC}V_{OC}} \quad (2.6)$$

where J_{max} is current density at the maximum power point, and V_{max} is the voltage at the maximum power point.

$$PCE = \frac{P_{max}}{P_i} = \frac{J_{SC}V_{OC}FF}{P_i} \quad (2.7)$$

where P_{max} is the device's maximum power, and P_i is a power of incident light[12]. The shape of the *JV* curve and magnitude of the *FF* is influenced by the loss mechanisms that occur in the device.

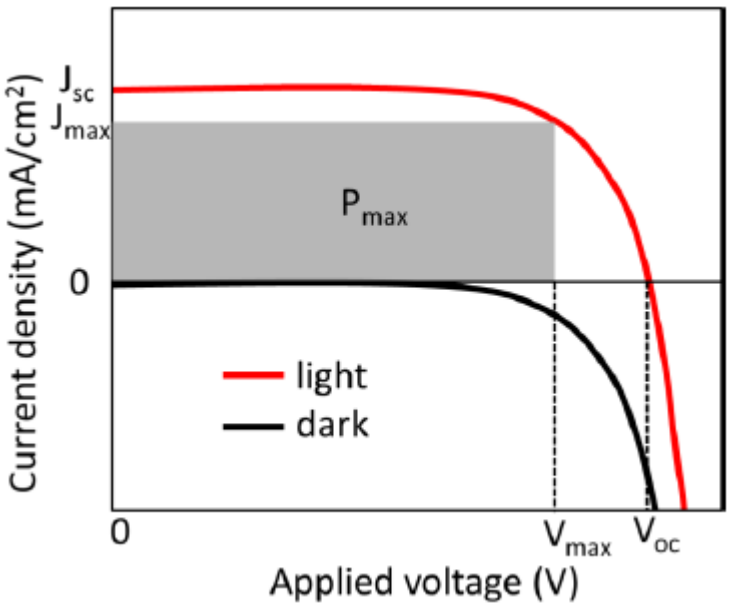

Figure 9. Example of a current-voltage curve with the representation of the main parameters, P_{max}, V_{max}, V_{OC}, J_{SC} and J_{max}.

2.4 Generations of solar cells

Reports on the photovoltaic effect exist since the beginning of the 19th century when the photovoltaic effect was discovered. Although there were subsequent reports on materials that exhibited the photovoltaic effect, none of the earlier technologies reported transcended towards optimization and actual application.

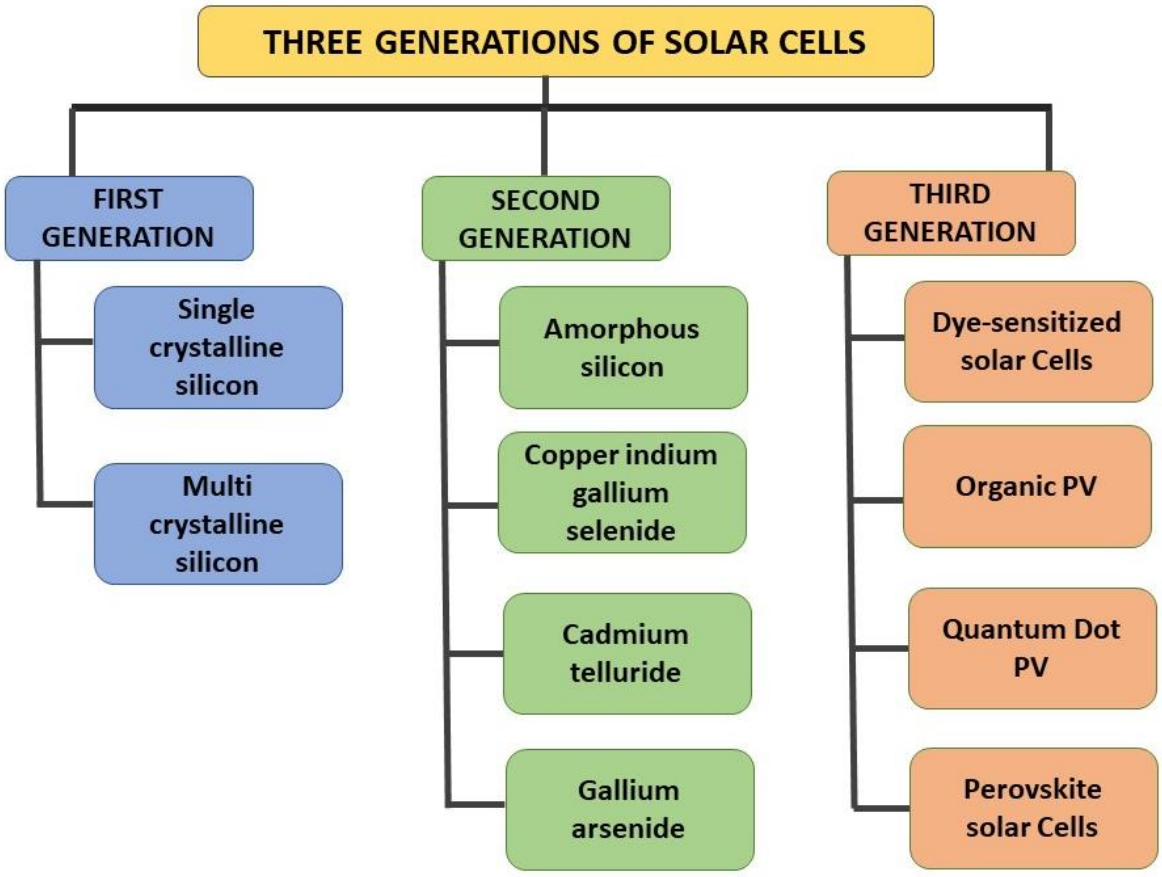

Figure 10. Generations of photovoltaic devices.

It was until the 1950s when the first silicon solar cell was fabricated, and the first generation of solar cells was born. The first generation of solar cells comprehends both

monocrystalline and polycrystalline silicon. This technology has transitioned from initial efficiencies of around 10% in the 1960s to current efficiencies higher than 25% at the laboratory scale. Presently, the photovoltaics market is dominated by silicon technology, with more than 95% of the global market in 2017.[14]

The first generation of photovoltaics is characterized by the expensive requirements of high vacuum and high temperature processes. This motivated the search for cheaper alternatives. In this search, the use of thin films in photovoltaic devices has founded the second generation of solar cells. The studies related to this technology started to take place back in the 1970s and the main materials studied were amorphous silicon, GaAs, CdTe, CdS and copper indium gallium (di)selenide (CIGS) photovoltaic. Moreover, the materials employed for the fabrication of these devices are widely available and the techniques are solution-based and at low-temperature, making them a potentially inexpensive photovoltaic technology. Many challenges remain before this technology can be commercialized. This is mainly related to their low thermal stability, low resistance to moisture in the presence of humidity and the toxicity of the lead component. [19,20]

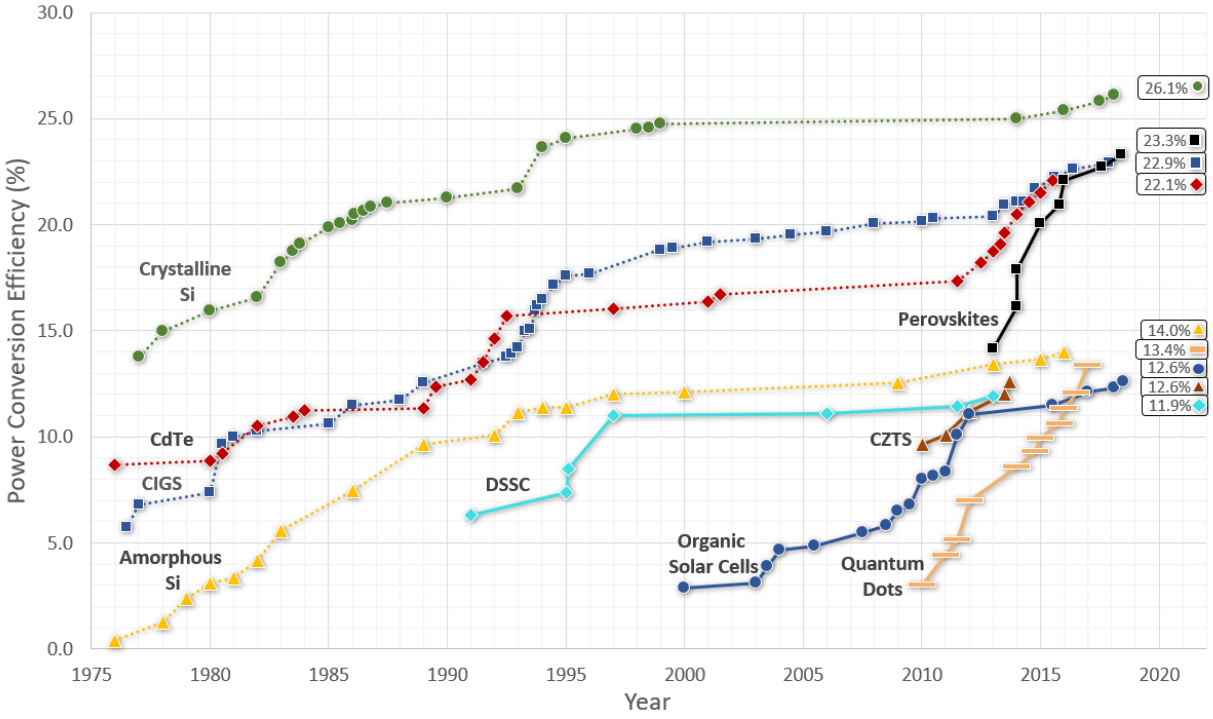

Figure 11. Evolution of research-cell efficiencies over the last 4 decades. PSCs have had an unprecedented increase in their efficiency in only a decade of research development, positioning on top of the rest of emerging technologies.

CHAPTER 3. PEROVSKITE SOLAR CELLS

3.1 Properties of the perovskite material

Perovskite materials share the crystal structure with that of calcium titanium oxide. They are defined as any ABX_3 compound with a network of corner-sharing BX_6 octahedra surrounding a larger A-site cation, where the cations, A and B, can span the periodic table and the anion, X, is typically oxygen or halogen. Figure 12 shows the crystal structure of perovskite with the usual components employed for the organic-inorganic metal halides currently applied in photovoltaics.

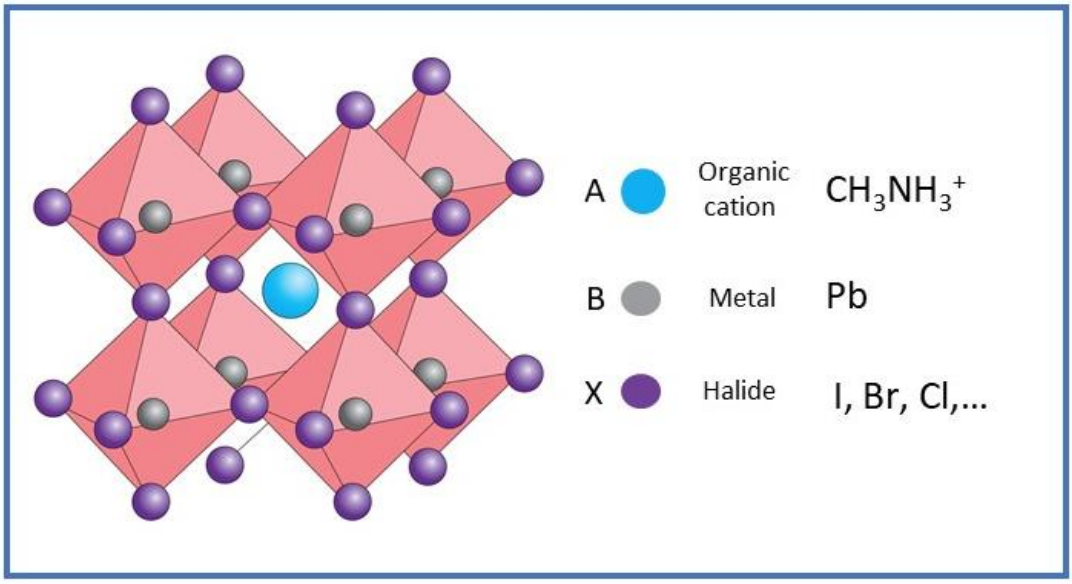

Figure 12. Perovskite crystal structure.

The organic-inorganic lead halides with perovskite structure that have become so relevant in photovoltaics were first studied back in the 1970s. Weber first reported the synthesis of the $CH_3NH_3PbX_3$ (X = Cl, Br, I) and the $CH_3NH_3SnBr_{1-x}I_x$ alloy with perovskite structure

and, since then, the chemical and physical properties of these materials have been studies. [21,22,23]

Among the discoveries made by the studies of the perovskite materials, three different phases for the crystal structure were identified: orthorhombic, tetragonal and cubic, in order of increasing temperature (Figure 13).[24] The orthorhombic perovskite structure is the low temperature ground state of MAPI and maintains its stability up to 165 K. At 165 K, the perovskite goes through a first-order phase transition from the orthorhombic to the tetragonal phase, which undergoes a second-order phase transition to the cubic phase at 327 K. [25]

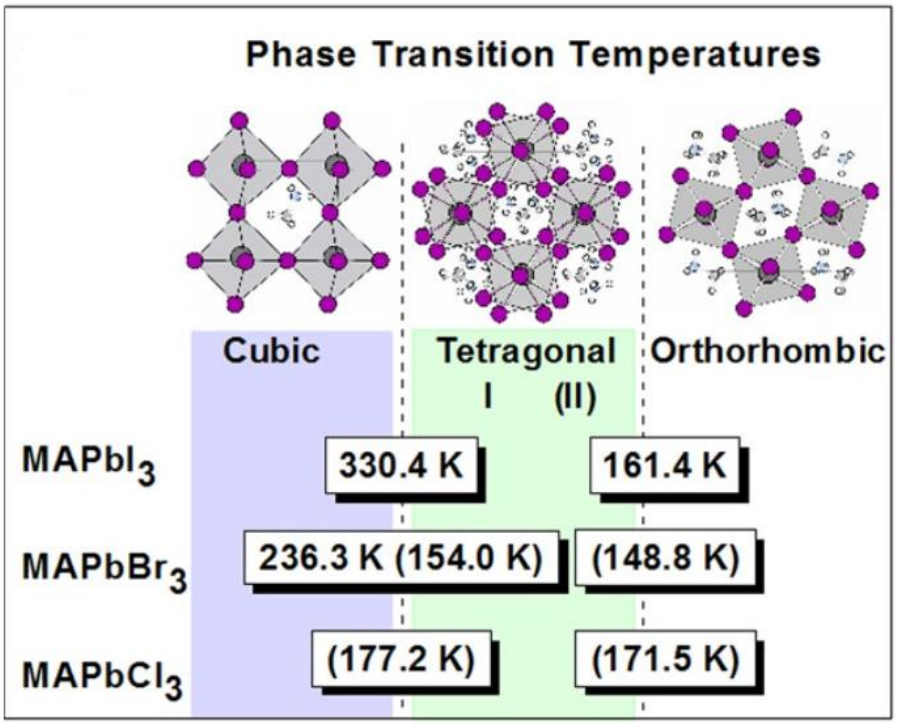

Figure 13. Phase transitions versus temperature of different halide compositions of organic-inorganic lead-halide perovskites (Niemann et al., Halogen effects on ordering and bonding of $CH_3NH_3^+$ in $CH_3NH_3PbX_3$ (X= Cl, Br, I) hybrid perovskites: a vibrational spectroscopic study."

Since the report of their application in photovoltaics, broader attention has been paid to the detailed study of these materials. They exhibit high optical absorptivity; the absorption coefficient of MAPI, (>3.0 × 10^4 cm^{-1} in the visible light region) is more than one order of magnitude higher than that of silicon, therefore, thinner films are required to effectively harvest solar radiation. The reported thickness of MAPI varies between 0.3 to 0.6 µm contrasting with the 2 to 300 µm required in the case of silicon.[26–28] This represents the use of less material and avoids issues related to the use of thicker films.

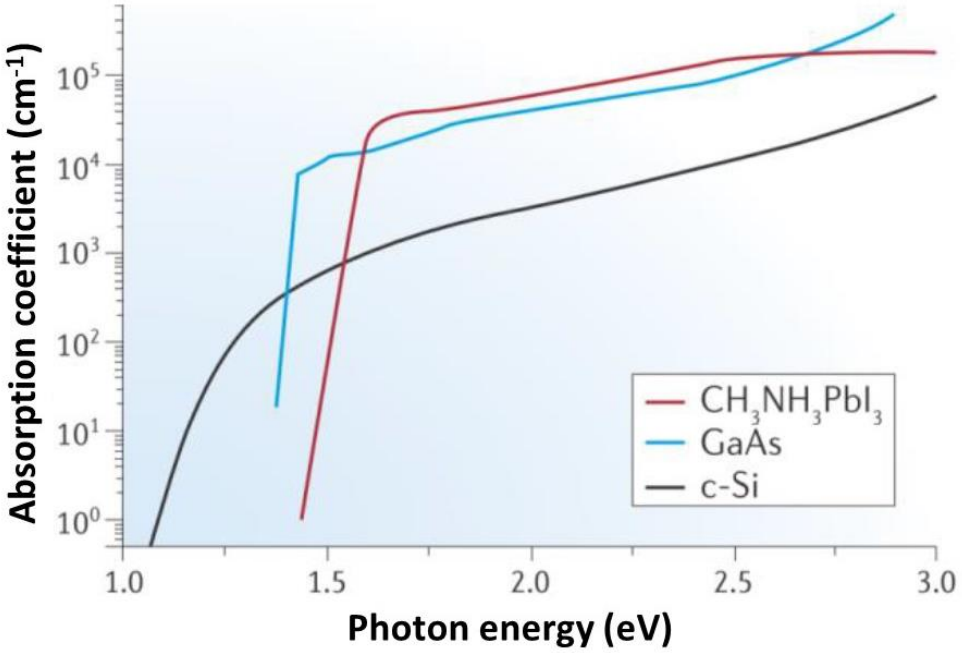

Figure 14. Absorption coefficient of MAPI ($CH_3NH_3PbI_3$), crystalline silicon and gallium arsenide.

As indicated in Figure 15, perovskite material has a great versatility in terms of composition and its optical properties can be tuned accordingly. Bandgap tuning is one of the main reasons that perovskite is an extensively explored material for solar cell fabrication.

The bandgap of the organic-inorganic metal halide perovskites can be tuned from 2.3 eV to 1.17 eV. There are two reported ways to achieve this: by replacing the methylammonium cation with other organic cations; organic cations in A position of ABX_3 can modify the gap by altering the M − X − M bond length and bond angle and without modifying the band maximum.[29] A reduction of about 0.07 eV in the bandgap has been achieved, when MA is replaced with formamidinium (FA, $[HC(NH_2)_2]^+$) resulting in an increase of the absorption wavelength by approximately 40 nm. [30]

The bandgap can also be altered by modifying the proportion of Pb to Sn. When Pb^{2+} in $CH_3NH_3PbI_3$ is partially substituted by Sn^{2+}, the gap in band reduces from 2.3 eV to 1.17 eV.[31]

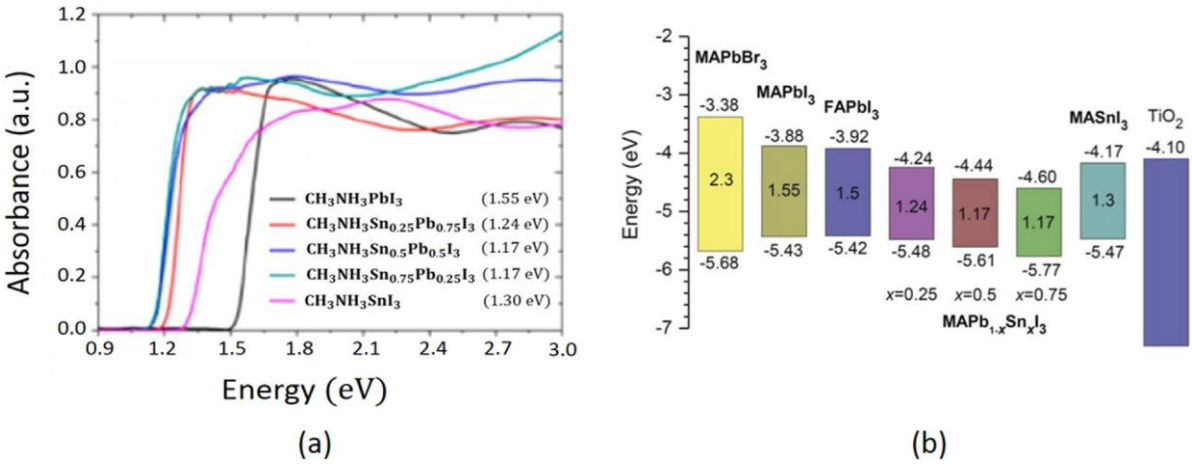

Figure 15. (a) Electronic absorption spectra of $MAPb_{1-x}Sn_xI_3$, (b) graphical sketch of energy level for $MAPbBr_3$, $MAPbI_3$, $FAPbI_3$, $MAPb_{1-x}Sn_xI_3$, $MASnI_3$ and TiO_2.[32](Ansari et al., "Frontiers, opportunities, and challenges in perovskite solar cells")

The dynamics of the A cation have been described as liquid-like molecular reorientations that screen the Coulomb potential of the charge carriers and thus slow down their recombination within the lattice.[33] Furthermore, the A^+ dynamics coupled to deformation of

the lattice have been associated to several local effects, such as the formation of transient nanoscale ferroelectric domains and the localization of conduction and valence band edge in spatially separate regions.[34] All these effects can be associated to extremely low electron-hole recombination and significantly suppressed charge carrier trapping, which are the underlying reasons for the exceptionally good photovoltaic performance of ABX_3 perovskites.

Although the composition of the perovskite plays a key role in the exceptional performance of the devices based on these materials, it also contributes to their complexity. Many studies indicate that temperature, light and the presence of electric fields change the dynamics of the mobile ions present in the perovskite material, generating complex and anomalous behavior in the devices.[35] The ion migration phenomena, and the hysteresis that has been associated with it, will be reviewed in more detail in subsequent sections.

3.2 Perovskite film optimization

The rapid improvement in the performance of PSCs came mainly from the optimization of the perovskite film. In order to achieve this, a remarkable effort has been put into understanding the crystallization process of the perovskite, the effects of annealing and the impacts of solvent and concentration of the precursor solutions.

The initial approach was the synthesis of the perovskite film in a single step, where the lead salt and the organic salt were mixed in a single organic solvent: γ-butyrolactone (GBL), dimethylformamide (DMF), dimethyl sulfoxide (DMSO) or a mixture of the last two. An increase in efficiency was achieved when novel methods for the deposition of the

perovskite were developed, and the control of phase transitions lead to smoother films[36] with larger grain size such as two-step deposition [37], solvent engineering[38,39] and thermal evaporation[40].

A sequential deposition method was developed where the inorganic compound is deposited first and transformed to the perovskite phase later by the addition of the organic constituent. This improved the film coverage and increased the crystallite size, which reflected in higher performance than obtained for the available one-step methods.[37]

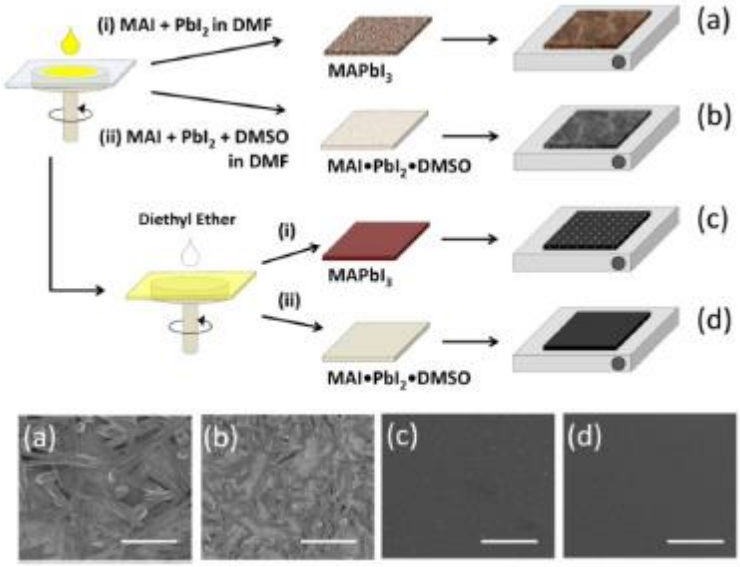

Figure 16. The study of several solvents and antisolvents to aid in the deposition of the perovskite film has facilitated the obtention of smoother films. (Ahn et al., "Highly Reproducible Perovskite Solar Cells with Average Efficiency of 18.3% and Best Efficiency of 19.7% Fabricated via Lewis Base Adduct of Lead(II) Iodide".)[38]

An important drawback in the synthesis of the perovskite films has been the detrimental effect of humidity in the synthesis of optimal films and in the stability of the devices fabricated. Recently, a better understanding of the combined effect of solvents and the effect of water molecules, present in the environment during the synthesis of the film, has

led to the development of robust methods capable of being calibrated as a function of the environment humidity, delivering high quality perovskite films and devices with higher stability than those fabricated under dry conditions.[41-42]

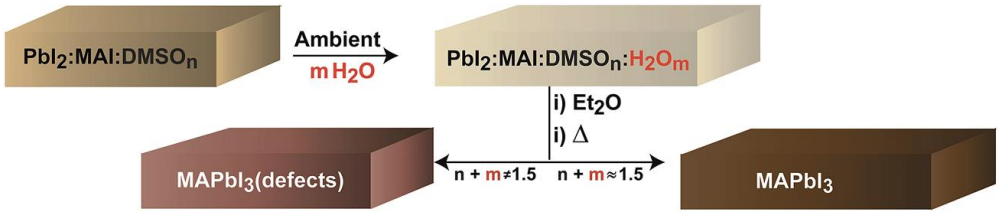

Figure 17. Schematic representation of key steps during the one-step fabrication process that takes into account the effect of ambient for photovoltaic cells. In this report, $CH_3NH_3PbBr_3$ and $CH_3NH_3PbI_3$ are used as light sensitizers in a structure otherwise identical to the one used for dye-sensitized solar cells, with an 8-12 µm TiO_2 film as the photoelectrode (anode), an electrolyte solution and a Pt-coated FTO glass as the counter electrode (cathode). They obtained an efficiency of 3.81%, which was significantly higher than those obtained to that date with non-organic sensitizers and quantum dots. [43]

Although it started with modest efficiencies and the device had a short lifetime of seconds before the perovskite was dissolved in the electrolyte solution, the material showed promising characteristics that hold to this day: it is composed of abundant elements, has the advantageous optoelectronic properties detailed in the previous section and the synthesis of the perovskite absorber and the fabrication of the rest of the device can be achieved with relatively easy solution-based synthesis methods. This unprecedented combination has led to photovoltaic devices that can be processed at room temperature and achieve performance levels similar to industry giant polycrystalline silicon of up to 23.7% for record devices.[44] This steep improvement is unprecedented, taking into account that the starting point was 3.8% in 2009.[43]

The evolution of the design of the devices has resulted in the current study of mainly four types of devices shown in Figure 18. The first design studied is the n-i-p mesoporous device, where the perovskite film is deposited over a mesoporous film of TiO_2 that acts as the electron selective contact (Figure 18-a); the organic compound Spiro-MeOTAD is employed as the hole selective contact.

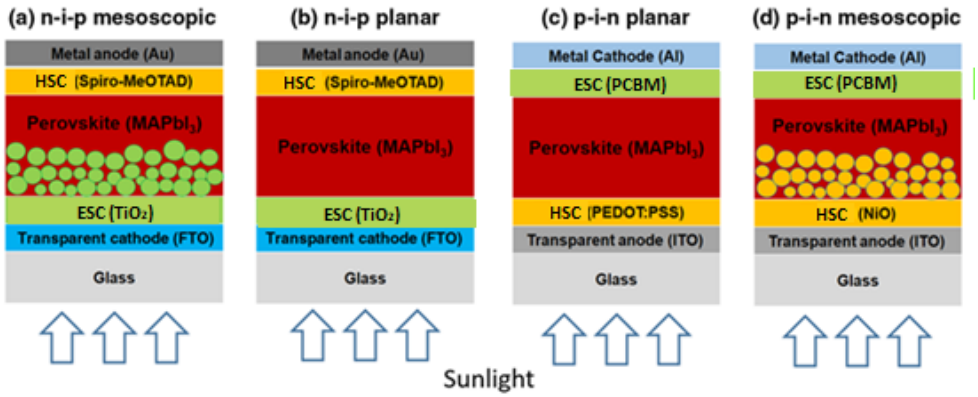

Figure 18. Perovskite solar cells different configurations depending on the order in which the Electron Selective Contact (ESC) and the Hole Selective Contact (HSC) are deposited and, additionally, on their mesoporous or planar nature.

In planar n-i-p devices (Figure 18b) the mesoporous film is omitted, and the perovskite is deposited over a planar compact layer of TiO_2. Long carrier diffusion lengths, L_D, found for perovskite materials exceed the absorption depth of sunlight in the perovskite absorber layer enabling the deposition of thick enough films to obtain a good performance in planar devices.[27]

The capacity of the perovskite material to transport both charge carriers, usually denominated as an ambipolar character, gives place to working devices where one of the selective contacts is absent or takes the form of an insulator scaffold, as is the case for the alumina and zirconia-based PSCs.[27,45,46] This type of devices usually displays a lower and less stable performance than the four device designs depicted in Figure 18, but they are

useful for the study of the working mechanisms of the devices and to better understand the properties of the perovskite absorber.

The versatility of the PSCs configuration extends as well to the order in which the selective contacts are deposited. Under these criteria, conventional and inverted configurations of PSCs are defined.

The conventional hybrid perovskite solar cell design consists of a conductive transparent oxide contact (FTO or ITO); a compact, thin layer of an oxide, generally SnO_2 or TiO_2; a mesoporous film as an electron selective contact (ESC), typically TiO_2 – in planar PSC, this mesosporous film is not present, and the compact, thin layer acts as the EEL; a perovskite film that fills the mesoporous film and forms capping layer of about 400 nm; an organic hole selective contact of about 200 nm, generally spiro-MeOTAD; and a metallic contact, generally gold or silver. In the inverted system, the order of films is different: the hole selective contact (HEC) is deposited first and consists of a p-type material, generally NiO_X or PEDOT:PSS; the hybrid perovskite absorber film is deposited on top of the HEC, followed by an organic electron selective contact, usually with PCBM; finally a metallic contact, usually Ag, is evaporated on top of the PCBM.

While the conventional configuration resulted from the introduction of perovskite as a sensitizer in quantum dot solar cells, the p-i-n or inverted configuration was the result of exploring if the perovskite absorber would also work in a structure similar to the structure of organic solar cells, where PEDOT:PSS usually acts as a hole selective contacts and PCBM as the electron selective contact.[47,48] Although the first efficiencies were under

10%[47], studies focused on the improvement of the selective contacts/ perovskite interface, have already achieved efficiencies around 20%.[49,50]

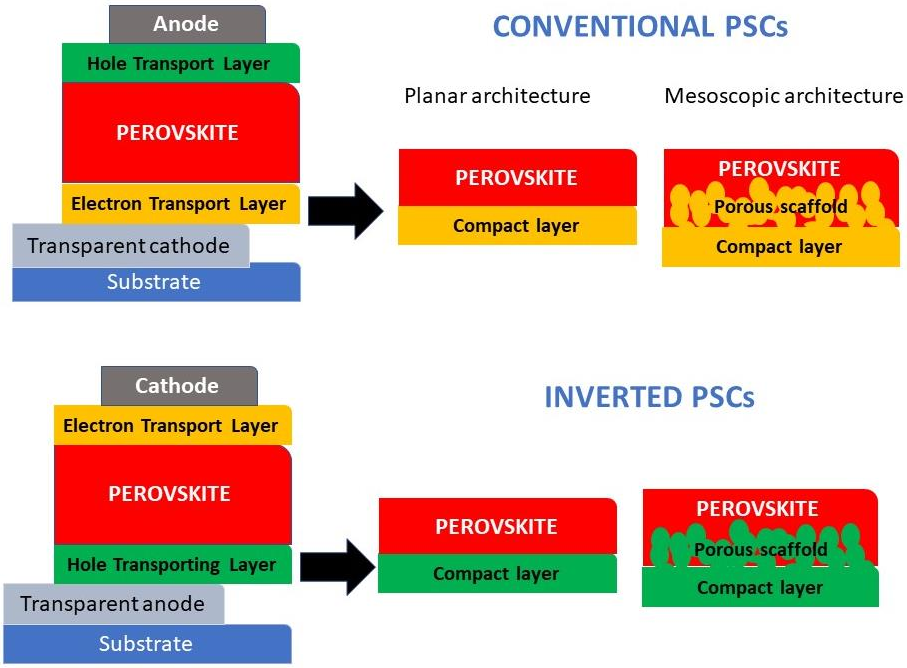

Figure 19. Schematic representation of the conventional and inverted configurations of PSCs.

3.4 Selective contacts

As stated before, photovoltaic conversion involves the following processes: carrier photogeneration and charge separation within the perovskite material, and charge extraction by the selective contacts. Many studies have focused on the exact mechanisms of charge generation and separation occurring in the perovskite layer and on measuring the diffusion length and carrier lifetime.[45,51–53] As relevant and necessary as it is to study the intrinsic properties of the perovskite active layer and their impact on the device performance, charge separation is also an important process that occurs in the selective contacts. An effective

charge extraction is crucial for good device performance and the study of the roles of the selective contacts is necessary to get an insight into the impact of interfacial recombination and efficient charge extraction on the final performance of the solar cell.

The most commonly used selective contact materials for electrons and holes in conventional perovskite solar cells are TiO_2 and spiro-MeOTAD, respectively. However, other materials have been studied and shown to work as selective contacts. Inorganic materials such as CuI and CuSCN have been used as hole selective contacts[54,55] while studies focused on the effect of the electron selective contact have reported the replacement of TiO_2 with materials like alumina, zirconia, SnO_2 and ZnO.[56–58]

The most efficient perovskite solar cells still employ a thin mesoporous TiO_2 layer. These cells have a thick perovskite capping layer. The porous oxide facilitates crystallization of the perovskite film with superior properties. Furthermore, meso-TiO_2 seems to be making excellent electronic contact with the perovskite, where charges are efficiently collected across the interface with minimal resistive losses. Planar heterojunction cells devoid of metal oxide are not lagging far behind in record efficiency, but more work on interfacial engineering and structural optimization of the perovskite layer is required to achieve PCEs exceeding 20%.

For the inverted configuration of perovskite solar cells, PEDOT:PSS was the first material to be applied as hole selective contact; however, the hygroscopic nature and acidity of this material proved detrimental to the stability of the devices. Nickel oxide has become the main alternative to PEDOT:PSS. Although NiO_X presents disadvantages related to its low conductivity, doping and morphology control of the NiO_X film have improved the

efficiencies of NiO_X-based inverted PSCS close to those of the conventional devices. [48,59,60] Figure 20 presents a summary of the wide arrange of perovskite absorber compositions and selective contacts used in conventional and inverted devices.

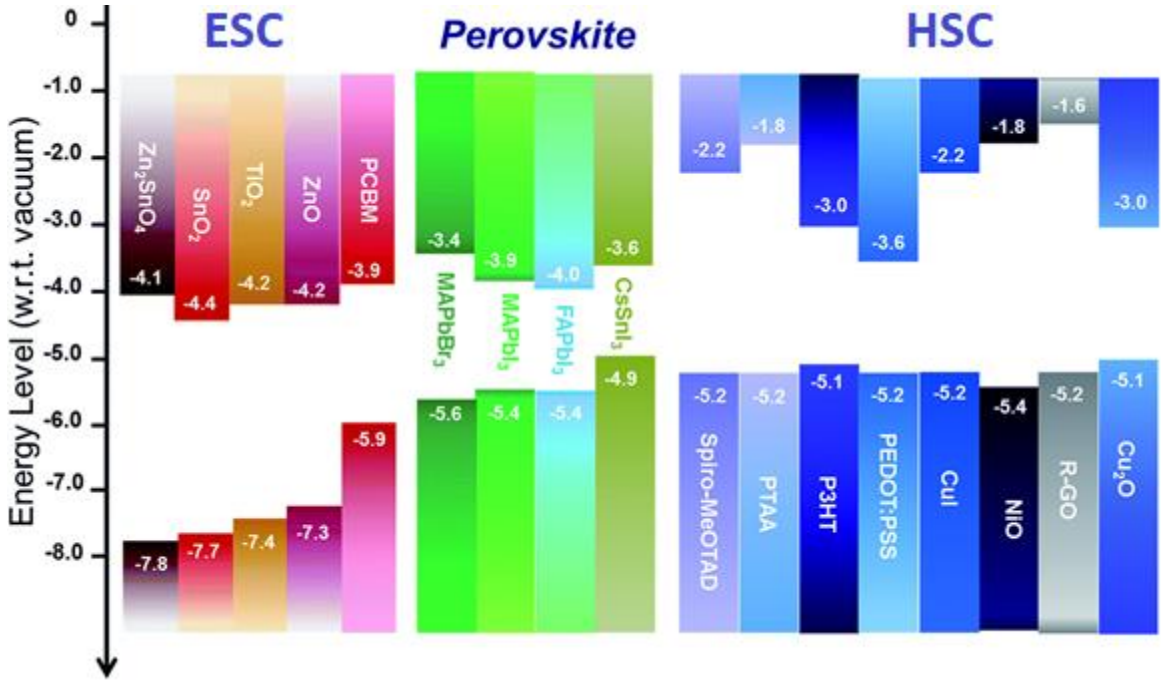

Figure 20. Perovskite absorbers and materials applied as electron selective contacts (ESC) and hole selective contacts (HSC) in conventional and inverted PSCs.

3.5 Working mechanisms of perovskite solar cells

The basic principles of hybrid perovskite semiconductor solar cells are shared with other photovoltaic technologies, however, there are particularities regarding the behavior of the absorber material and its carrier dynamics. The following section contains a summary of the progress made concerning the study of the working mechanisms and the carrier dynamics in perovskite solar cells. Some of these topics are still under debate and the main proposed theories offered as possible explanations are presented.

3.5.1 Generation of charge carriers

During the initial stages of the study of perovskite solar cells, the hybrid nature of the perovskite material brought the question of whether its behavior regarding the generation of carriers corresponded to that of inorganic or organic materials. To answer this question, studies of the exciton binding energy (E_B) were performed. As mentioned in the section for the charge generation in PV devices, the binding energy is a determinant factor in the dynamics of charge generation in the form of excitons and charge carriers.

In the case of the perovskite material, a consensus has been reached that the direct generation of free charges dominates the conversion process from photons to the photocurrent. The exciton binding energies were obtained from characterizations in the form of dielectric constant measurement[61], optical spectroscopy [62] and magneto-absorption spectroscopy.[63] The values obtained vary from 2 MeV to 75 MeV; [62–66] these values are specific to the perovskite absorber composition and depend on the crystal size of the perovskite. Higher values of the binding energy were found for larger crystals and exciton generation was found more pronounced in samples with larger grains.[62] Excitons were more likely generated at locations with higher crystallinity, and free charges were found at the center of grains with many small domains. The values obtained for the binding energies were later used to investigate the predominant charge species generated after light absorption. The results suggest that free charges are predominant over excitons under solar cell operating conditions, even when the highest values of E_B are considered.

3.5.2 Recombination

After charges have been formed and separated, electrons and holes have to reach the anode and cathode respectively. If during their path electrons make contact with holes they recombine immediately, resulting in losses since generated charges were not collected at the electrodes.

The concentration of charges (both electrons and holes) as a function of time, under operating conditions, is expressed by the general continuity equation:

$$\frac{d\rho_N}{dt} = G - k_1\rho_N + k_2\rho_N^2 + k_3\rho_N^3 \qquad (3.1)$$

Where ρ_N represents charge carrier density in number of particles per volume (either electrons or holes), meanwhile G is the charge generation term, $k_1\rho_N$, $k_2\rho_N^2$ and $k_3\rho_N^3$ are the terms related with monomolecular, bimolecular and trimolecular recombination mechanisms, respectively.

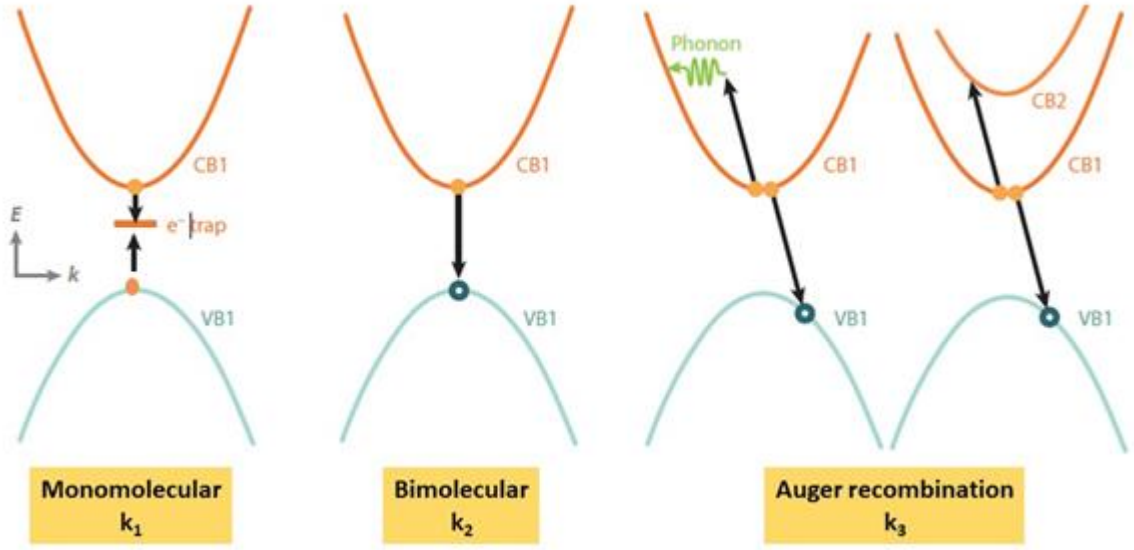

Figure 21. Schematic diagram indicating recombination mechanisms active in organic-inorganic metal halide perovskites. (*a*) Trap-assisted recombination is a monomolecular process involving the capture of either an electron or a hole in a specific trap state; (*b*) bimolecular recombination may occur between electrons and holes and (*c*) Auger recombination is a higher-order process involving at least three particles. Abbreviations: CB, conduction band; CBM, conduction band minimum; VB, valence band; VBM, valence band maximum (Herz, L.M., "Charge-Carrier Dynamics in Organic-Inorganic Metal Halide Perovskites"). [67]

Monomolecular recombination (*k1*). Non-radiative, trap-assisted recombination. It is the principal mechanism in PSC[68] and has a strong dependence on processing conditions. A variety in the nature and depth of traps has been reported, which is expected given the great variety of processing methods that lead to films with different characteristics. The dynamics of this type of recombination is also specific to the composition of the perovskite films, and may vary spatially, becoming faster at the grain boundaries. Therefore, the effect is different depending on the crystallite size of the perovskite. [69–72]

Bimolecular recombination (*k_2*). Recombination between electrons and holes puts a limit on the diffusion length of the charge carriers. Under the Langevin model it is assumed that recombination between electrons and holes will occur when both charge carriers move within their joint capture radius; within this assumption a limit of the ratio between k_2 and

the mobility (μ) is predicted. Materials with k_2/μ values that are short of the Langevin limit are desirable for PV applications since they allow for long charge carrier diffusion lengths (L_D). It has been found that MAPI and $MAPbI_{3-x}Cl_x$ fall short of the Langevin limit by at least four orders of magnitude.[73–75] This is consistent with the large L_D values found for perovskite materials, ranging from 100 nm to several micrometers.[51]

Auger recombination **(k_3).** Auger recombination is a many-body process that involves recombination of an electron with a hole, accompanied by energy and momentum transfer to a third participant, either an electron or a hole, potentially also involving phonon absorption or emission. Less attention has been paid to the Auger recombination in perovskite materials. This is probably because the Auger rate constant (k_3) values calculated for perovskite materials suggest that it is unlikely to have a relevant effect on the performance of the devices under standard sunlight.

3.6 Hysteresis

A discrepancy between the current density-voltage (J-V) curves of perovskite solar cells manifests when they are obtained from opposite scan directions. Usually, the reverse scan (from open-circuit to short-circuit conditions) delivers a J-V curve with superior performance than the one obtained in the forward scan (Figure 22). This anomalous behavior is described as hysteresis and it is an important issue that hinders the development of this technology.

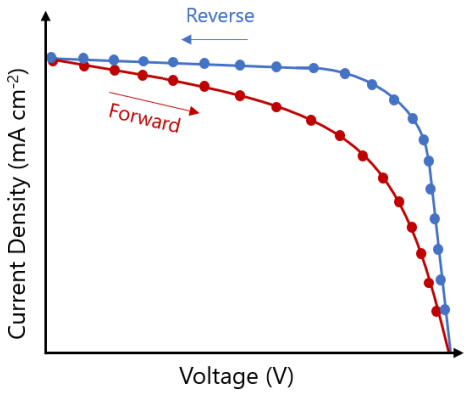

Figure 22. J-V curve representing the hysteresis usually found in perovskite solar cells, where a higher performance is found for the reverse scan.

The time scale of the hysteresis is on the order of seconds, which is in contrast with the typical charge generation/recombination processes occurring in the scale of nanoseconds in PSCs.[73,76] Identifying the origin of this anomalous phenomenon has proven challenging since it seems to be affected by a variety of factors: the device configuration, the perovskite composition, fabrication conditions and measurement conditions such as the scan rate, the amplitude of the external electrical field, scanning direction and pre-scanning conditions.[77–80]

Three mechanisms have been proposed to explain the origin of hysteresis: ferroelectricity, charge trapping/ detrapping and ionic migration. A brief review of these proposed mechanisms is given in the following section.

Ferroelectricity: The theory of ferroelectricity is mostly based on studies performed on single crystals of $CH_3NH_3PbI_3$ that place the possible alignment of the organic dipole with lattice polarization as indirect evidence of hysteresis in the solar devices.[81,82] The current-voltage sweeps performed on single crystals of $CH_3NH_3PbI_3$ resemble a ferroelectric loop.

The argument against this theory is that time scales of the ferroelectric hysteresis in single crystal materials are incompatible with the times scale in which hysteresis is manifested in perovskite solar cell devices. Additionally, NMR studies show a fully disordered distribution of organic dipoles even at room temperature for Cl^-, Br^-, and I^- based hybrid halide perovskites. [22]

Charge Trapping/Detrapping. The facile and low-temperature synthesis of perovskite films that is so valuable for the fabrication of the devices has the disadvantage of inevitably involving the generation of defects, which potentially impact the charge separation/ recombination and charge transport.[79] Among the possible defects are: 1) defects located energetically at the CB/VB band edge following an exponential decrease distribution; 2) deep-level defects within the bandgap. For the first type, the evidence suggests that the energetic width of the defect states near the band edge, i.e., Urbach tail energy, ranges between 20 and 40 meV, depending on the fabrication methods.[83] This value is much smaller than in many typical inorganic semiconductor materials, e.g., Si, copper indium gallium (di)selenide (CIGS), CdS, etc.[84] For the second type, these defects lay deep within the bandgap and can serve as potential trap sites for the charge carriers, being responsible for non-radiative (Shockley–Read–Hall) recombination.[69] Filling and releasing charges at these trap sites could modulate the components of the perovskite materials is more likely to engage in migration. It has been found that the species more likely to migrate are methylammonium cations and iodide anions. [34,91]

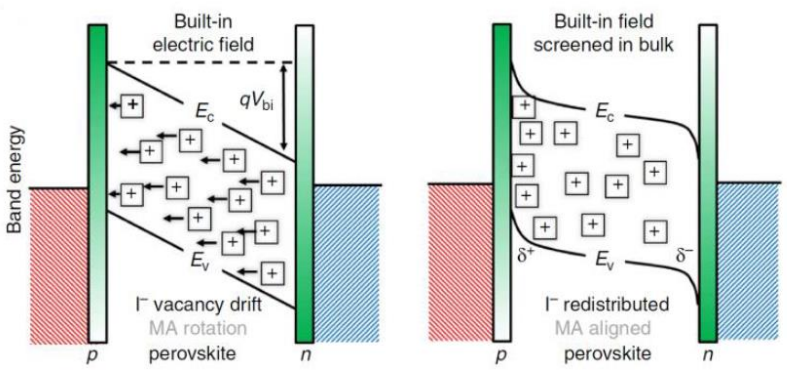

Figure 23. Schematic representation indicating the influence of migrating ions on the band structure under external electrical field. (a) Before migration, the voltage drops across the perovskite film uniformly. (b) After the redistribution of ions, the internal field is shielded by the accumulated ions at the interfaces (Eames, C. et al., "Ionic transport in hybrid lead iodide perovskite solar cells").[88]

Computational studies have estimated a diffusion coefficient for the migrating species responsible for the measured hysteresis. Van Reenen et al. estimated the diffusion coefficient of the ion species responsible for the measured hysteresis at 10^{-11} cm^2/s.[92] In another study, Eames et al. obtained a similar diffusion coefficient of 10^{-12} cm^2/s.[88]

Some of these studies subsequently estimated the diffusion coefficient for the different ionic species. In the case of methylammonium (MA), the value found was 10^{-16} cm^2/s, which is four to five orders of magnitude smaller than the predicted coefficient. Meanwhile, the coefficient of iodide ions is within this estimated value, which suggests that iodide ions play a more important role in the hysteresis compared with MA ions.[92] However, there is no conclusive study and both methylammonium and iodide ions are still considered possible candidates for ion migration.

3.7 Electrochemical impedance response of PSCs

Electrochemical Impedance Spectroscopy (EIS) is measured by applying a small perturbation signal (1 to 10 mV) to an electrochemical cell and measuring the resulting current response. The small perturbation is applied in order to maintain a linear system. In a linear system, the current response to a sinusoidal potential will also be sinusoidal at the same frequency but may be shifted in phase. This characterization technique has proved useful for the study of different types of solar cells. By using time-dependent and frequency-dependent measurements, different processes taking place at different time constants can be accessed in an operating solar cell. This can improve the understanding of the solar cell device, by clarifying dynamic processes that occur in different frequency domains, and their relationship to the device structure.

Perovskite solar cells have proven challenging for the EIS characterization due to the complication of several processes occurring within similar time domains. This section covers the state of interpretation of the electrochemical impedance response for perovskite solar cells and the insights this technique can give on the effect of the bulk process and processes at the contacts specifically related to recombination and transport time constants.

There are at least two processes identified at different frequencies in perovskite solar cells, with some devices exhibiting up to three different time constants. Pockett et al. identified three processes happening at different frequencies through EIS and Intensity Modulated Voltage Spectroscopy (IMVS) (Figure 24-A) with the mid-frequency (MF) process more easily identified in the IMVS measurements.[76] They attributed the semicircle observed at high frequency (HF) to a geometric capacitance of the perovskite solar cell and the

resistance calculated from this semicircle as a measure of recombination. Their conclusions are based on the dependence of the capacitance extracted from the HF semicircle on light intensity and photovoltage. This is consistent with the thickness of the perovskite layer as Guerrero et al. subsequently demonstrated by showing a direct relation between the capacitance and the thickness of the perovskite layer.

With respect to the high-frequency resistance (R3) of the samples, a qualitative trend can be observed in which the size of the high-frequency arc decreases by decreasing the thickness of the perovskite layer, which indicates a relationship of R3 with the transport resistance of the perovskite layer.

Since the HF semicircle has been related to recombination processes in the perovskite solar devices, there have been several studies where the device structure or the materials used have been related to responses in the recombination dynamics. In a study by Contreras et al., the relation between the chemical composition of the perovskite absorber and the hole selective contact with the recombination dynamics was studied using electrochemical impedance spectroscopy. In this study, they performed the impedance measurements with two different illumination wavelengths, blue and red. The absorbance in the blue light part of the spectrum is much more intense than in the red light part of the spectrum for perovskite materials (Figure

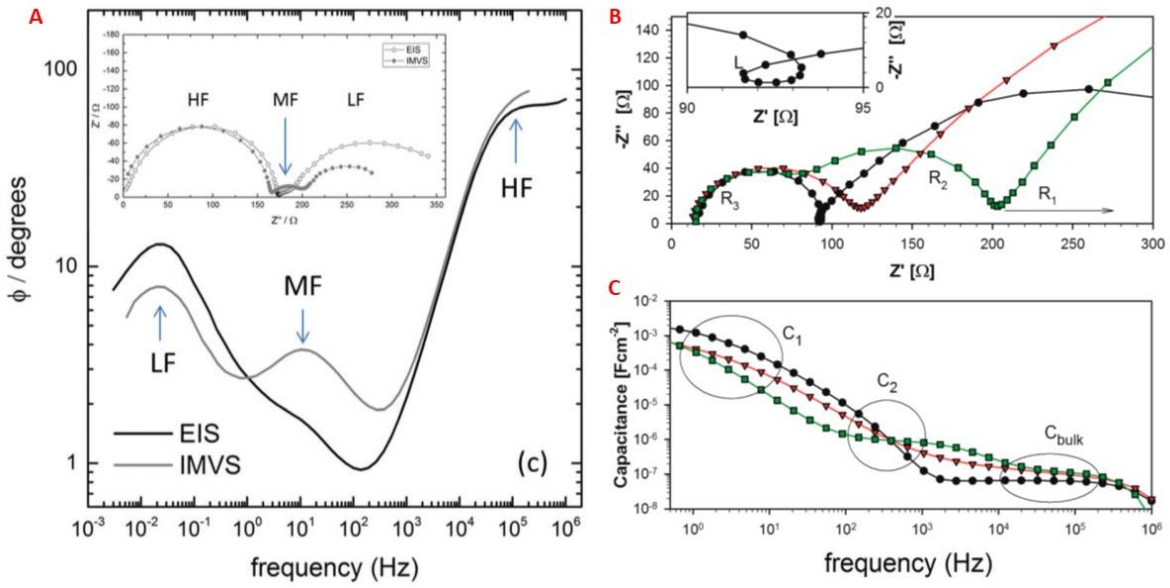

Figure 24. (A) Nyquist and Bode plots show the three processes identified at three frequencies found by Pocket et al. from EIS and IMVS measurements performed on PSCs (Reproduced from Pockett et al., Microseconds, milliseconds and seconds: Deconvoluting the dynamic behaviour of planar perovskite solar cells). (B) Guerrero et al. identified two semicircles and a loop at intermediate frequencies. (C) The three processes are better represented in the graph of the apparent capacitance versus frequency (Guerrero et al. "Properties of Contact and Bulk Impedances in Hybrid Lead Halide Perovskite Solar Cells Including Inductive Loop Elements").

25a); this makes possible to control the penetration of the optical excitation inside the perovskite layer and, in consequence, the generation profile of charge carriers, by using different illumination wavelengths. This has the potential to allow the detection of possible spatial inhomogeneities in the recombination kinetics or a more important contribution of the interface between the perovskite layer and the selective contacts.[93]

The impedance response was the same, independent of the different illumination wavelength, which was interpreted as an indication that the profile generation closer to the interface between the organic selective contact and the perovskite has no effect on the recombination kinetics and that, therefore, recombination is mainly dominated by the bulk of the perovskite absorber. This has also been confirmed by other studies where despite

using different hole selective contacts, the voltage and the values of the resistance to recombination remain the same.

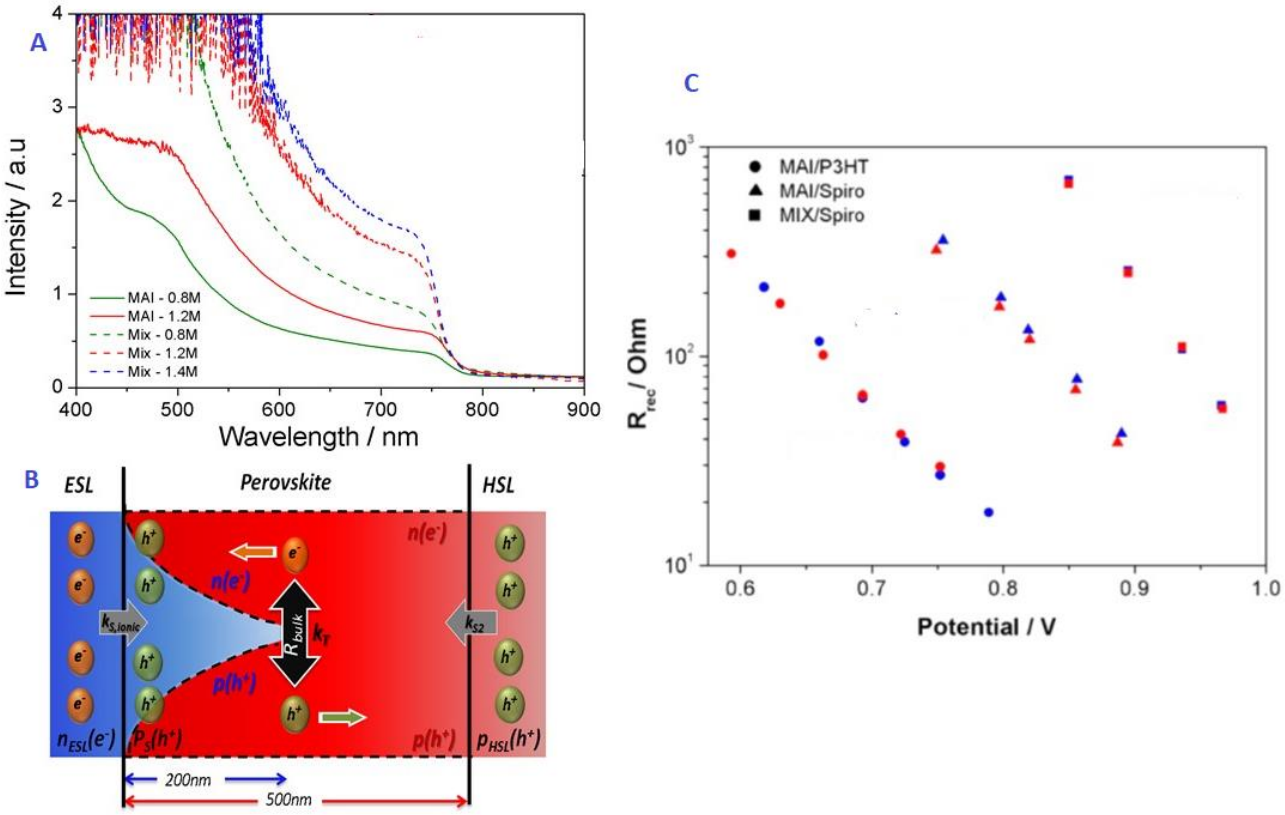

Figure 25. (A) UV-Vis spectra of different concentrations of perovskite and mixed cation perovskites, showing a stronger absorbance in the blue range (<500 nm) of the visible spectra for all compositions. (B) Light-induced (wavelength-dependent) electron−hole generation and bulk- and surface-mediated recombination processes (C) High frequency resistance versus open-circuit potential as extracted from fits of the impedance spectra using the two excitation wavelengths (blue and red) for configurations with different hole selective contact or perovskite composition (Contreras et al., "Origin and Whereabouts of Recombination in Perovskite Solar Cells"). [94]

On the other hand, the low-frequency (LF) semicircle has been attributed to phenomena related with ionic motion and surface charging phenomena. Evidence regarding the activation of these processes with temperature and the calculation of activation energies that are in agreement with ionic motion activation energies support this argument. [76,95]

The mid-frequency (MF) process identified by Pockett et al. in the EIS and IMVS spectra has been less known and studied. Pocket el al ascribe it to the same phenomena related to ionic motion since a dependence on temperature was also found, but the fact that this semicircle is often convoluted with the other two and not always appears in the impedance spectra, makes it difficult to establish its behavior in relation with illumination, voltage and temperature. It has also been suggested that the presence of a MF semicircle corresponds to a surface recombination process provoked by the poor electron injection efficiency.[96]

So far, only the HF and LF semicircles are the ones with plausible phenomena ascribed to them. The measurement of the low-frequency response as a function of temperature has allowed the estimation of an activation energy with a value between 0.55 eV and 0.68 eV, which is consistent with computationally predicted values for thermally activated ion movement. [76,88]

CHAPTER 4. METHODOLOGY

The experiments carried out for this study are divided between those studies performed in (i) conventional mesoporous perovskite solar cells and (ii) those performed in the inverted configuration. In this chapter, details regarding the synthesis of materials, fabrication of the devices and characterization techniques are provided.

For the first part, a study on different n-type contacts was carried out to explore the role of the electron selective contact in the performance of the mesoporous devices. Some of these materials applied as electron selective contacts were synthesized in our laboratory while others were obtained from commercial sources. Details on the synthesis of the materials and the deposition of the electron selective contacts are included in the following section.

For the second part of the work, where the p-type contact in inverted perovskite solar cells was studied, planar and mesoporous NiO_X films were prepared using the techniques of spin coating and spray pyrolysis.

4.1 Fabrication of conventional mesoporous PSCs with different electron selective contacts.

Figure 26 shows the configuration of the cells fabricated for this part of the study and the materials studied are divided between those synthesized and those obtained from commercial sources. The devices were composed by a fluorine-doped tin oxide (FTO) coated substrate on top of which a blocking layer of TiO_2 was deposited either by spray pyrolysis or atomic layer deposition (ALD). After the blocking layer, a film of

approximately 200 nm of different n-type oxides was deposited by spin coating to work as the electron selective contact.

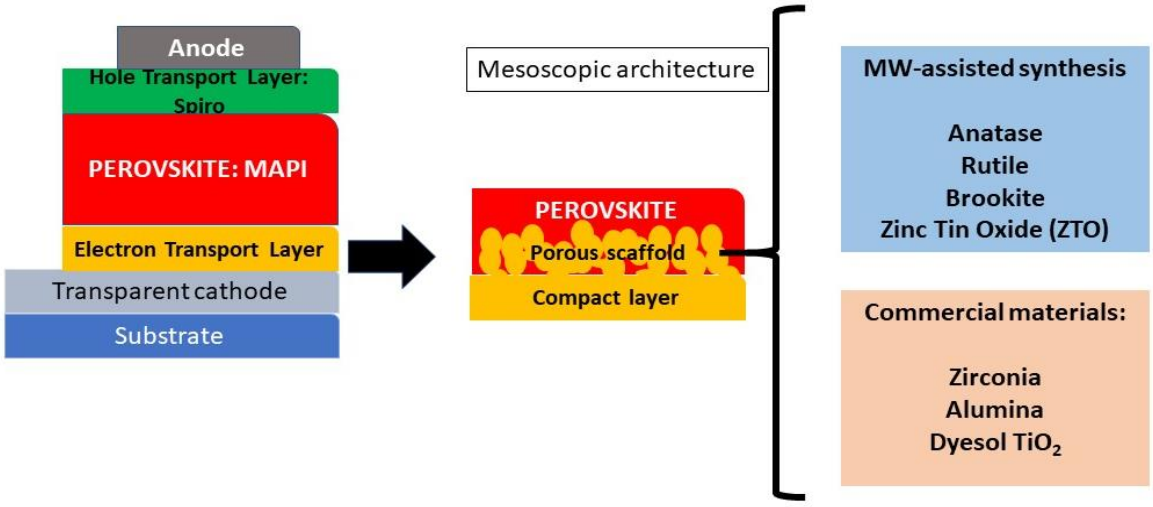

Figure 26. Electron selective materials studied in conventional mesoscopic perovskite solar cells.

4.1.1 Blocking layers of TiO_2

The devices were prepared on FTO coated glass (25 × 25 mm, Pilkington TEC15) with laser patterned etching (Figure 27). The substrates were cleaned with soap (Hellmanex), rinsed with Milli-Q water and subsequently washed with ethanol, isopropanol and acetone in an ultrasonic bath. The clean FTO substrates were heated at 450°C for 30 minutes to eliminate any organic residues.

Spray pyrolysis. In the case of the films prepared by spray pyrolysis, a precursor solution of titanium diisopropoxide bis(acetylacetonate) (75% in isopropanol, Sigma-Aldrich) diluted in ethanol (1:19 v/v) was deposited at 450 °C, using oxygen as the carrier gas. The

precursor solution was sprayed in 3 steps, waiting 30 seconds between each step. After the spraying process, the films were kept at 450 °C for 30 min.

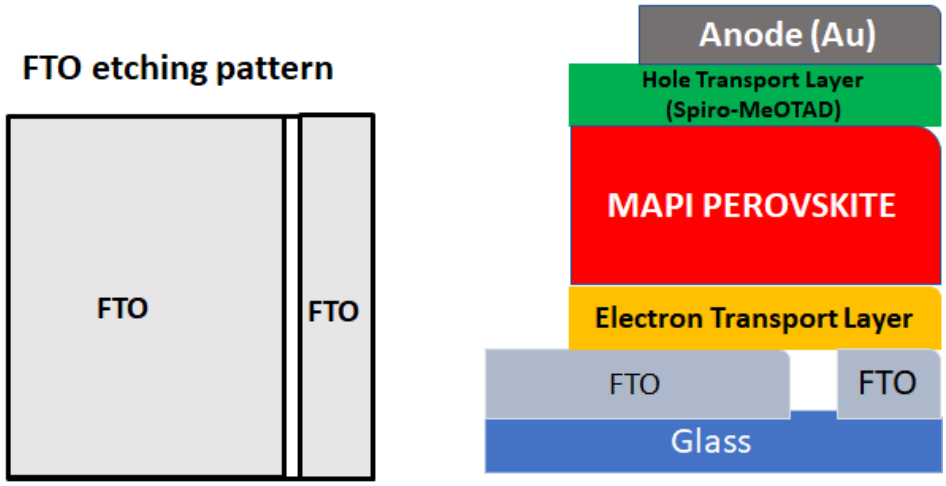

Figure 27. (Left) The FTO was partially etched to avoid short circuit (Right) Schematic illustration of the solar cell fabricated on top of the etched FTO. Four solar cells were deposited per FTO substrate.

ALD. For the blocking layers deposited by ALD, deionized water and the compound tetrakis (dimethylamido) titanium(IV) (TDMAT) acted as the precursors. The dosing time was 0.1 s for TDMAT and 0.015 s for water. The carrier gas used to transport the precursors was nitrogen; nitrogen was also used to purge the chamber for 10 s between the dosing pulses. The deposition was performed at a substrate temperature of 100 °C.

Since the blocking layers deposited by spray pyrolysis were exchanged by blocking layers deposited by ALD during the study of the electron selective contact, a preliminary experiment was carried out to evaluate the effect on the performance of the devices. The results are included in Appendix of this chapter. It was found that the average performance was very similar for devices with spray pyrolysis blocking layers and ALD blocking layers.

The main difference was a lower standard deviation in the average efficiency in the case of the devices prepared with ALD.

4.1.2 Synthesis and film deposition of the n-type oxides used as electron selective contacts.

The following section provides details on the synthesis of the rutile, brookite and anatase phases of TiO_2 as well as details on the synthesis of zinc stannate and zinc oxide. Details on the preparation of the pastes from the synthesized materials and the deposition of the films from both synthesized and commercial materials are also given.

The sol-gel process involves the transition of a system from a liquid "sol" into a solid "gel" phase. Is a technique widely used for the synthesis of semiconducting nanoparticles and has the advantage of producing materials with high purity and with a large surface area. The synthesis of TiO_2 nanoparticles using this method has been reported with a variety of precursor solutions and conditions that render different particle sized that can be tuned for many applications. It has been particularly relevant since the emergence of dye-sensitized solar cells, where the purity and large surface area of the nanostructured semiconductor oxides are crucial for the good performance of the devices.[97]

Microwave synthesis, in the other hand, is an alternative to conventional methods to provide heat and energy into a system with the potential of reducing the reaction time from days to minutes. In the case of semiconducting oxides, the conventional autoclave treatments are usually from 12 hours to several days long. The n-type oxides synthesized to be applied as electron selective contacts in this study were synthesized from a variety of

solution-based techniques. The thermal treatment was provided by microwave irradiation using a MARS 6 microwave digestion system.

As a first step, amorphous titania was synthesized following a method previously reported[98]; this was subsequently used as a starting material for the formation of the three crystal structures by microwave treatment under different experimental conditions. Amorphous titania was prepared by dropwise addition of a solution of 1.14 ml of water (Labconco WaterPro PS; 18 M cm) in 105 ml of 2-propanol (J.T. Baker, 99.9%) to a solution of 5 ml of titanium (IV) isopropoxide (Aldrich, 97%) in 105 ml of 2-propanol (J.T. Baker 99.9%) under stirring at 0 °C. The solution was stirred for 24 h at room temperature and filtered to yield a white paste of amorphous titania. Water was added to the clear filtrate, resulting in a second precipitation product.

Synthesis of the anatase: 0.25 g amorphous titania was dispersed in 30 mL water and sonicated for 20 minutes. The dispersion was introduced in a microwave reactor and treated at 200 °C for one hour with a ramp time of 40 minutes. The power used for the treatment in one reactor was 400 W. A stable pressure of 220 psi was observed during the reaction. The resulting product was washed with water and ethanol several times.

Synthesis of rutile: A 0.1 M solution of amorphous titania in 5 M HCl was treated at 180 °C in a microwave reactor for 10 minutes with a ramp time of 40 minutes.

Synthesis of brookite. A 0.5 M solution of amorphous titania in 3 M HCl was treated at 180 °C in a microwave reactor for 10 minutes with a ramp time of 40 minutes. This synthesis conditions produced a mixture of brookite (>90%) and rutile. The rutile was removed by

washing with water, where rutile tends to precipitate. The brookite was later recovered evaporating the water.

A paste was prepared mixing a suspension of anatase in ethanol with terpineol and a solution of ethyl cellulose in ethanol at a mass ratio of 1:8:0.3 anatase:terpineol:ethyl cellulose. The ethanol was removed using a rotary evaporator. The prepared paste was further diluted with ethanol to 4% wt. in anatase and spin coated at 4500 rpm for 30 seconds.

Synthesis of zinc stannate: Zinc stannate was synthesized following a previous report.[99] In this procedure, $ZnCl_2$ and $SnCl_4 \cdot 5H_2O$ were used as sources of Zn and Sn, while Na_2CO_3 was used as a mineralizer. $ZnCl_2$ and $SnCl_4 \cdot 5H_2O$ were dissolved in water and stirred for 3 hours to obtain a transparent solution. An aqueous solution of Na_2CO_3 was added dropwise until reaching a molar relationship between Zn:Sn:Na_2CO_3 of 2:1:4. A white precipitate was observed after the addition of the mineralizer and the resulting solution was further stirred for one hour before thermal treatment. Thermal treatment was performed in a microwave reactor at 200 °C for 1 hour, at a power of 800 W, reaching a stable pressure of 225 psi.

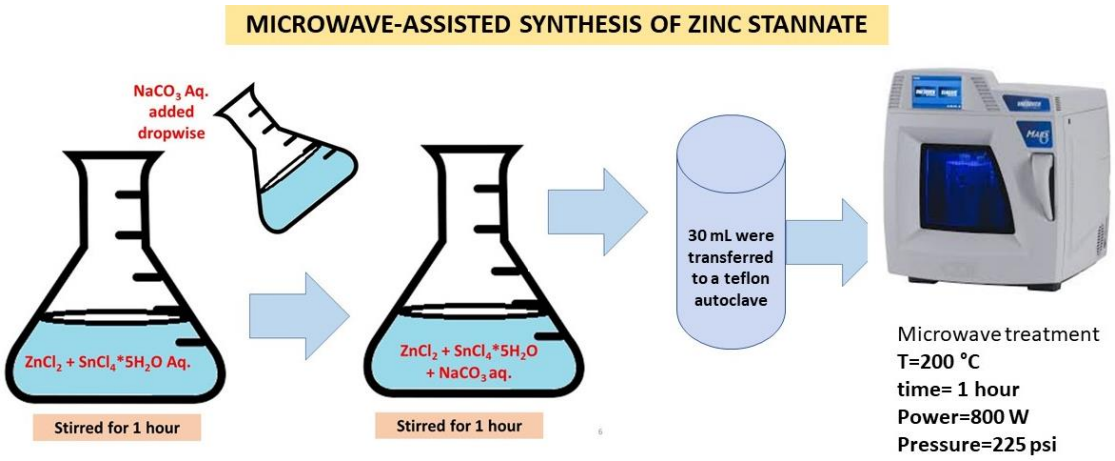

Figure 28. Procedure followed for the microwave synthesis of zinc stannate.

The resulting product was washed once with water and twice with ethanol to separate zinc stannate from other species. An amount of 0.5 g Zn_2SnO_4 in 10 mL ethanol was mixed with 0.15 g ethyl cellulose and 4.5 g terpineol. The ethanol was removed using a rotary evaporator. The resulting paste was diluted with ethanol to 3 % wt. of Zn_2SnO_4 to use for spin coating. Films were spin coated at 4000 rpm for 30 s and sintered at 500 °C for 30 minutes.

4.1.3 Film deposition of the commercial n-type oxides used as electron selective contacts.

Alumina: An amount of 0.5 g Al_2O_3 nanopowder (Sigma Aldrich <50 nm) in 10 mL ethanol was mixed with 3.5 g terpineol and 1 g ethyl cellulose. The resulting paste was further diluted with ethanol to a final proportion of 4% wt of alumina to use for spin coating, films were spin coated at 2000 rpm for 30 s and sintered at 500 °C.

Anatase (Dyesol 18NR-T) and ZrO2 (SOLARONIX): The mesoporous TiO_2 and ZrO_2 layers were deposited by spin coating at 4000 rpm for 10 s using a diluted solution of the DYESOL or SOLARONIX paste in ethanol (16% wt). After drying at 120 °C for 10 minutes, TiO_2 and ZrO_2 mesoporous layers were heated at 500 °C for 30 min and later cooled to room temperature. The thickness was of approximately 200 nm.

4.1.4 Synthesis of the perovskite layer

Precursor solution: Two solutions (A and B) were initially prepared: Solution A consisted of 1.50 mM PbI_2 (Sigma-Aldrich, 99%) diluted in a mixture of 1 mL DMF and 95 µL DMSO. This solution was heated to 80 °C until the PbI_2 was completely dissolved. The PbI_2 solution was left to reach room temperature before adding 1.5 mM CH_3NH_3I. For solution B, 157 µL DMSO was mixed with 525.8 µL DMF. Finally, 150 µL of solution A and 68 µL of solution B were mixed to obtain the final perovskite precursor solution.

The MAPI films were deposited in a one-step process, in air, at a relative humidity between 30 and 40% using diethyl ether as antisolvent. A volume of 50 µL of the perovskite precursor solution was deposited on the mesoporous substrate and spin coated at 4000 rpm for 50 s. Diethyl ether was used as antisolvent and it was dispensed during the third second of the spinning cycle. After the deposition step, the substrate was sintered at 100 °C for 3 minutes. The perovskite films were covered with the hole selective contact by spin coating at 4000 rpm for 30 seconds using 50 µL of the following spiro-OMeTAD solution: 1 mL chlorobenzene, 72.3 mg (2,2′,7,7′-tetrakis(N,N′-di-p-methoxyphenylamine)-9,9′-spirobifluorene), 28.8 µL 4-tert-butylpyridine, and 17.5 µL of a stock solution of 520

mg/mL lithium bis- (trifluoromethylsulfonyl)imide in acetonitrile. Finally, a 60 nm gold film was thermally evaporated on top of the device to form the electrode top contact.

4.2 Characterization of conventional mesoporous PSCs.

4.2.1 X-Ray Diffraction

The crystal structure of the synthesized n-type oxides was determined by X-ray diffraction (XRD) using a Siemens D-5000 with CuKα radiation.

4.2.2 Optical characterization

Perovskite films were deposited on the different electron selective contacts for their optical characterization, including UV-Vis and steady-state photoluminescence (PL) spectrophotometry, the latter at an excitation wavelength of 532 nm. The performance of the devices was determined from the current density-voltage curves measured under 1 sun illumination conditions, with a masked area of 0.16 cm^2 at a scan rate of 50 mV/s. Additionally, cyclic voltammetry was performed at different scan rates to study the hysteresis of the devices.

4.2.3 Electrical characterization

The performance of the devices was determined from the current density-voltage curves measured under 1 sun illumination conditions, with a masked area of 0.16 cm^2 at a scan rate of 100 mV/s using a Keithley 2400 source measurement-unit under AM 1.5 G, 100 mW/cm2 illumination from a 450 W AAA solar simulator (ORIEL, 94023 A). This was calibrated using a NREL-certified calibrated monocrystalline silicon solar cell. A black

metal mask (0.16 cm2) was used over the square solar cell active area (0.5 cm^2) to reduce the influence of scattered light. The active area of the masked solar cells was 0.16 cm^2 and the measurements were made at a scan rate of 100 mV/s with a pre-sweep delay of 5 s at 1.2 V).

The effect of the different ESC materials on the recombination dynamics of the devices was probed using impedance spectroscopy (IS). The illumination for the IS measurements was provided by a red and a blue LED (λ_{blue} = 465 nm and λ_{red} = 635 nm) over a range of five DC light intensities. The impedance spectra were obtained applying a 20 mV perturbation in the 10^6 -10^{-2} Hz frequency range superimposed on the open circuit voltage. A response analyzer module (PGSTAT302N/FRA2, Autolab) was utilized to analyze the frequency response of the devices. The degree of hysteresis from the devices was calculated from cyclic voltammetries obtained at four different scan rates (1000 mv/s, 100 mV/s, 10 mV/s and 1 mv/s) under illumination provided by a white LED.

4.3 Fabrication of the inverted perovskite solar cells

For this part of the study, the effect of the p-type NiO_X, contact was studied in the inverted configuration of PSCs. Planar and mesoporous configuration of these cells were studied by changing the morphology of the NiO_X film.

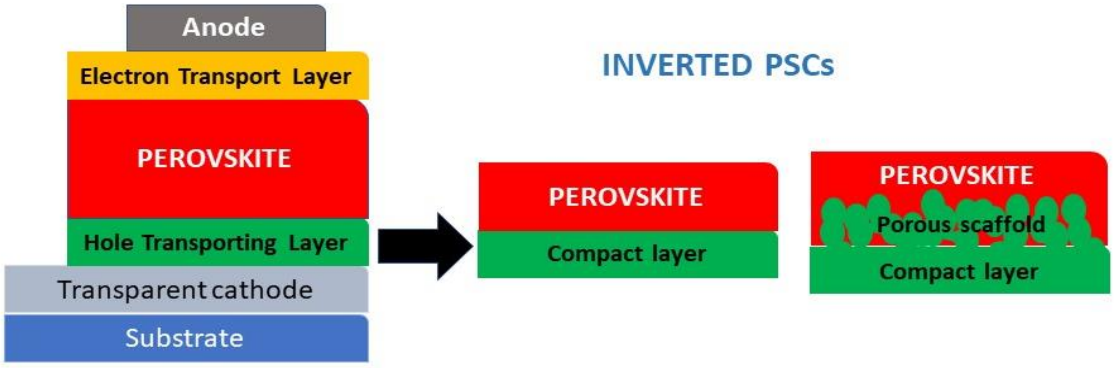

Figure 29. For this part of the work, mesoporous and planar films of nickel oxide were studied as the hole selective contact in p-i-n PSCs.

4.3.1. Deposition of the the NiO_X compact layer

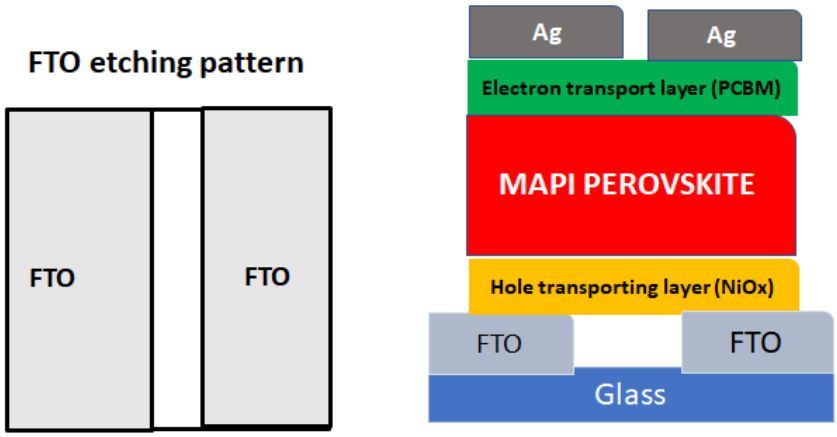

Figure 30. (Left) Etching pattern used to avoid short circuit in the inverted PSCs. (Right) Schematic representation of the devices. Each FTO substrate supported six solar cells.

The inverted devices were fabricated on FTO-coated substrates. The FTO was partially etched as shown in Figure 30 using a 2 M solution HCl and Zn powder. The etched FTO substrates were rinsed with deionized water and sequentially sonicated for 15 minutes at 60 °C with a 2% solution of Hellmanex detergent, water, acetone, ethanol and isopropanol. The clean FTO substrates were treated under irradiation from an ozone lamp for 30 min

(UV/Ozone ProCleaner, Bioforce Nanosciences) immediately before the NiO_X film was deposited.

Compact layer of NiO_X by spin coating. A 0.2 M solution of nickel acetate tetrahydrate (50 mg/ml) in 2-methoxyethanol was prepared as the precursor solution. Once the nickel acetate was dissolved, a small amount of ethanolamine (12 μl/ml) was added to the solution. The solution was filtered using a PTFE syringe filter (45 μm) and deposited onto the FTO substrates at 3000 rpm for 30 seconds. After spin coating, a cleaning swab dipped in 2-methoxyethanol was used to partially remove the NiOx layer in order to allow for contact with the FTO. The deposited films were heated on a hot plate at 500 °C for 30 minutes.

Compact layer of NiO_X by spray pyrolysis. A method was optimized to obtain an effective NiO_X selective contact by spray pyrolysis. The precursor solution consisted of nickel acetylacetonate dissolved in acetonitrile. Concentrations from 5 mM to 20 mM of the precursor solutions were used for the deposition in order to estimate the optimal concentration.

The solution was deposited using a chromatography sprayer and a manual pump. The deposition was performed over clean FTO substrates preheated at 450 °C in cycles of one spray every 30 seconds. Different numbers of cycles were also studied to explore the optimal thickness of the film. After the deposition of the films, the substrates remained in the hot plate for 30 minutes at 450 °C.

Mesoporous NiO_X films. The mesoporous NiO_X films were deposited from a commercial paste of NiO_X distributed by Solaronix. In order to get a thickness <1μm, the paste was diluted in ethanol. Different ratios of ethanol/NiO_X paste were evaluated to optimize the mesoporous film thickness. The paste dilutions were deposited onto the NiO planar films either by spin coating or spray pyrolysis. The deposition was performed at 3000 rpms for 30 s. After deposition, the films were heated on a hot plate at 200 °C for 10 minutes and subsequently transferred to a furnace and heated at 450 °C for 30 minutes.

4.3.2 Synthesis of the perovskite layer.

The perovskite film was deposited onto the NiO_X films by the antisolvent technique inside a dry box where humidity was kept under 20%. The precursor solution of the perovskite consisted of a 1.25:1.25 molar solution of MAI and PbI_2 dissolved in a mixture of 80% volume of DMF and 20% volume of DMSO. The solution was stirred at 60 °C until fully dissolved, then filtered through a PTFE syringe filter (45 μm). A volume of 100 μl of the perovskite precursor solution was spin coated onto the NiO_X sample surface at 4000 rpm for 30 seconds; 6 seconds after the start of the spinning, a volume of 200 μl of ethyl acetate (EA) was deposited directly onto the center of the spinning sample. After spin coating, the sample was transferred to a hot plate at 100 °C and annealed for 10 minutes. The films were deposited by spin coating and then heated on a hot plate at 100°C.

Electron selective material deposition. A 20 mg/ml solution of PCBM in chlorobenzene was prepared and stirred at 60 °C to ensure dissolution. The solution was filtered through a PTFE syringe filter (45 μm). The PCMB film was deposited by spin coating onto the perovskite at 3000 rpm for 30 seconds and dried at room temperature. A 0.5 mg/ml solution

of bathocuproine (BCP) in ethanol was deposited right after the PCBM film at 6000 rpm for 30 seconds and left to dry at room temperature.

Silver contact evaporation. A small area of the perovskite (overlapping with the region of NiO_X that was removed) was removed to allow the silver to contact the underlying FTO. The silver was deposited by evaporation through a shadow mask.

4.4 Characterization of the inverted perovskite solar cells.

4.4.1 Electrical characterization

Current voltage curves of the solar cells were measured with a Keithley 2601A potentiostat under 1 sun illumination intensity. The illumination intensity was calibrated with a certified WPVS monocrystalline silicon reference cell. A 1.2 V was applied to each cell prior to each measurement under illumination. A linear potential scan was applied from 1.2 V to 0 V and immediately from 0 V to 1.2. V at a scan rate of 100 mV/s with a step size of 10 mV. A mask of (0.25 x 0.25) cm^2 was employed to avoid additional contributions of scattered light in the glass. Impedance spectroscopy and hysteresis measurements were performed employing a ModuLab XM PhotoEchem system (Solartron Analytical). Before each measurement, the cell was under a 470 nm LED (Thorlabs M470L3) illumination (4.37 mW/cm^2) for 15 minutes to obtain a stable open circuit potential. The impedance measurements were made under open circuit potential under blue LED illumination and employing a small amplitude perturbation of 10 mV in the 100 kHz to 100 mHz frequency range.

For the hysteresis measurements, the cell was illuminated with a blue LED (Thorlabs 470 nm) at open circuit for 15 minutes or until the open circuit potential became stable. The illumination intensity employed was 4.37 mW/cm^2. 1.2 V are applied prior to each scan rate for 5 seconds. The cell was measured from open circuit conditions (V_{OC}) to short circuit conditions (J_{SC}) and immediately after from J_{SC} to V_{OC}. After each scan rate, the cell is illuminated at open circuit potential for 2 minutes. The scan rates employed are presented in Table 1 in the order in which they were applied.

#	Scan Rate (mV/s)	#	Scan Rate (mV/s)	#	Scan Rate (mV/s)
1	7000	**8**	300	**15**	10
2	5000	**9**	200	**16**	7
3	3000	**10**	100	**17**	5
4	2000	**11**	70	**18**	3
5	1000	**12**	50	**19**	1
6	700	**13**	30		
7	500	**14**	20		

Table 1. The hysteresis index of the devices was calculated from the voltammetries obtained at the different scan rates shown in the table.

The hysteresis index (HI) was calculated from the ratio between the areas under the J-V curves according to the following expression:

$$HI = 100 * \left(\frac{A_{\,reverse\,scan} - A_{\,forward\,scan}}{A_{max}} \right)$$

CHAPTER 5. ELECTRON SELECTIVE CONTACTS IN REGULAR MESOPOROUS PEROVSKITE SOLAR CELLS.

Introduction and background

Initial studies on perovskite solar cells were exclusively on devices where, analogous to DSSCs, the electron selective contact consisted of a mesoporous film of TiO_2. In these initial stages, the perovskite absorber layer was thought to merely play the role of the sensitizer.

The long charge carrier diffusion lengths of the perovskite material gave place to the fabrication of efficient planar devices; in these devices, the mesoporous TiO_2 was omitted and a compact TiO_2 layer worked as the electron selective contact. Further modifications of the device architecture and the experimentation with different selective contacts lead to the discovery of the ambipolar behavior of the perovskite material, this is, its capacity to transport electrons and holes without the presence of a selective contact. This made the study of working devices possible, where one or both of selective contacts were omitted. In a seminal work by Lee et al.[27], it was demonstrated that even a mesoporous Al_2O_3 insulating film on top of compact TiO_2 layer is sufficient to extract the full potential of a perovskite film, however, in this case the compact TiO_2 layer is the electron-selective contact. Several studies reported PSCs without hole selective contact with efficiencies surpassing the 10%. [46,100,101]

Although the devices without selective contacts delivered a lower performance than conventional devices, these studies were useful to illustrate that the perovskite material was

not a mere sensitizer. In addition to work as an absorber material, perovskite materials exhibit an ambipolar character that gives them the capacity to transport charge carriers.

Although the existence and study of devices without electron selective contacts is of interest to study specific properties and dynamics of the perovskite solar cells, selective contacts should be carefully chosen to ensure an adequate band offset and good transport properties. These characteristics guarantee a good performance by ensuring that the large number of electron-hole pairs photogenerated within the active layer are not lost via surface or bulk recombination processes, related to bad transport or inadequate band offset. In work by Juárez-Pérez et al.[56] it is shown that a hybrid perovskite film produces no rectifying behavior, and that adding a hole or electron (or both) selective contact is necessary to increase the short-circuit photocurrent (J_{SC}) and the open-circuit photovoltage (V_{OC}).[56]

It is also known that the omission or even the use of an inadequate hole selective contact leads to a substantially lower V_{OC}.[54,55,102,103]

As for the specific role of the selective contacts in efficient devices, Ravishankar and coworkers[104] studied high-efficiency PSCs prepared with FTO, compact TiO_2 and mesoporous TiO_2, and found that the V_{OC} was determined by quasi-Fermi level splitting within the MHP rather than by the work function of the electron selective contact. This suggests that when sufficiently good selective contacts are chosen, interfacial recombination plays no relevant role in the determination of the $V_{OC.}$ It has been found that different morphologies and crystallinities of mesoporous TiO_2 contacts do not lead to substantial differences in V_{OC}, but produce a high impact on the J_{SC} and the hysteresis behavior instead.[96] Numerical modelling showed that this feature arises if the

recombination rate increases for contacts where electron extraction is not sufficiently efficient. Related to this finding, there have been other reports pointing to the fact that different contacts produce a quite distinct hysteresis behavior.[105]

This part of the work is focused on the results and conclusions obtained from the study of the effect of different n-type electron selective contacts (ESC) in the performance of mesoporous methylammonium lead iodide ($CH_3NH_3PbI_3$ = MAPI) perovskite solar cells. In addition to the typically employed ESC, *Dyesol* TiO_2 paste, this study includes the three crystalline phases of TiO_2 (anatase, rutile, and brookite) and zinc stannate (ZTO) synthesized in our lab by microwave assisted techniques, as well as commercial alumina (Al_2O_3) and zirconia (ZrO_2). ESC/MAPI films were characterized by optical absorption and steady-state photoluminescence (PL) measurements, as detailed in the methodology section.

Full devices with the configuration FTO/ blocking TiO_2 compact layer/ mesoporous ESC/ MAPI/ Spiro-MeOTAD/ Au were studied by current-voltage voltammetry and impedance spectroscopy (IS) to investigate trends in the photovoltaic parameters with respect to the nature of the contact and their link to the recombination kinetics. Figure 31 shows the materials studied as ESC. As evidenced by the energy band levels, zirconia and alumina act as insulator scaffolds where electron injection does not occur while titanium dioxide, zinc stannate and zinc oxide act as conventional ESC where electron injection is permitted.

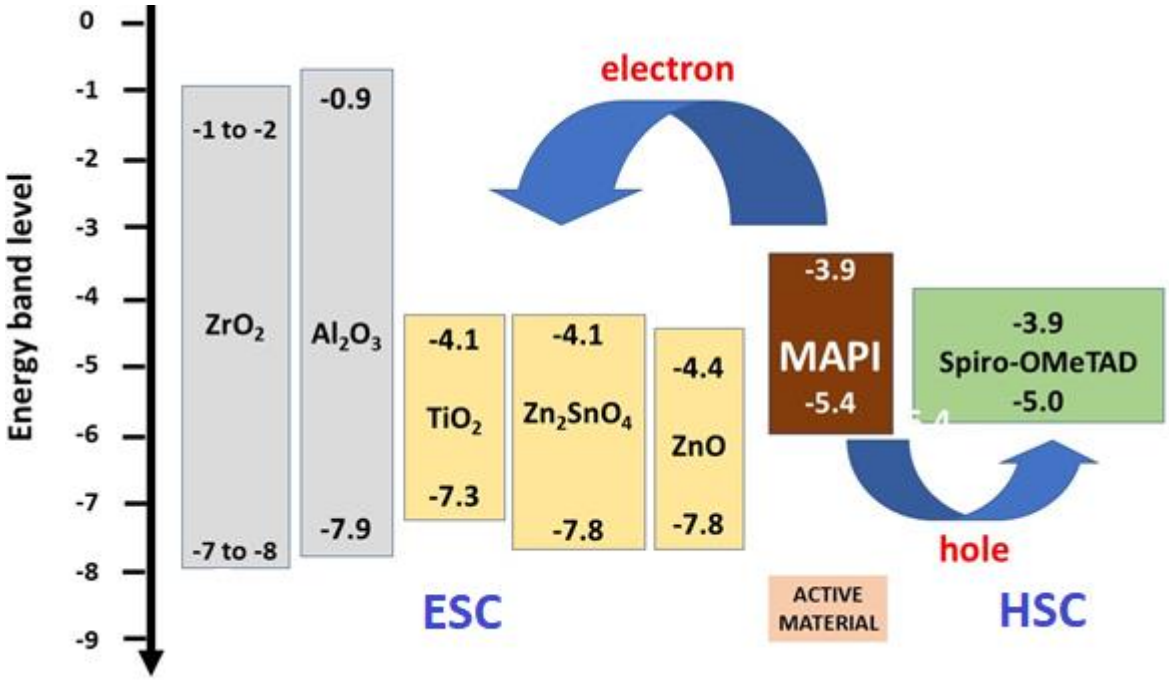

Figure 31. Schematic representation of the contacts studied as electron selective contacts (ESC) and their energy levels in the configuration ESL/MAPI/Spiro-OMeTAD. Electron injection occurs in the case of TiO_2, Zn_2SnO_4 and ZnO while Al_2O_3 and ZrO_2 act as insulating scaffolds where electron injection is prohibited.

Results

The best performance was achieved in the solar cells fabricated with *Dyesol* paste, with the best cell reaching an efficiency of 15.2%. The average performance of the devices fabricated with microwave-assisted sol-gel synthesized anatase was actually very close to the average values obtained for the *Dyesol* paste. This shows that in analogy to dye-sensitized solar cells,[106] where anatase is by far the best performing photoanode, the choice of the right crystalline polymorph of TiO_2 is also critical for good electron selectivity in PSCs. Zinc stannate (ZTO)-based devices showed an average efficiency of around 10%, with the best performance reaching 12.3%. The rest of the materials showed a significantly lower performance. With the exception of alumina, it is a general result that *all* contacts

produce a high V_{OC} close to 1 V. In fact, when the photocurrent is normalized with respect to its short-circuit value, all devices yield the same V_{OC} (with the exception of alumina). Hence, the loss of performance is mainly due to a reduced J_{SC} and fill factor.

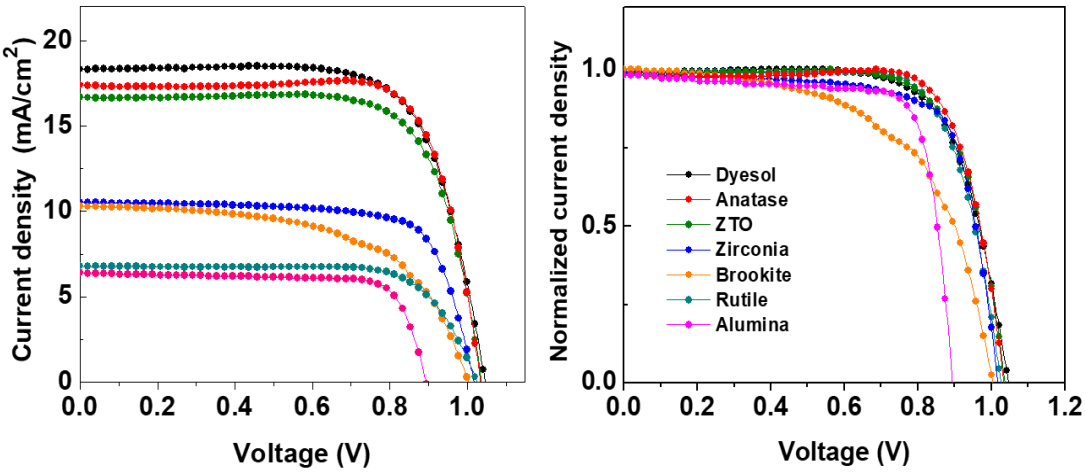

Figure 32. Current-voltage curves for champion MAPI devices (left) and the result of their normalization with respect the short-circuit photocurrent (right). Measurements were carried out under 1-sun AM1.5G standard conditions with a scan rate of 50 mV/s in reverse scan.

Electron Extracting Layer	J_{SC} [mA/cm^2]	V_{OC} [V]	FF	PCE %	
				Average	Highest
Dyesol	18.3 ± 1.9	1.00 ± 0.04	69 ± 3	12.6 ± 1.0	15.2
Anatase	17.1 ± 0.4	1.01 ± 0.04	71 ± 4	12.2 ± 1.1	13.8
Zinc Stannate (ZTO)	13.5 ± 2.2	0.98 ± 0.04	67 ± 6	9.0 ± 1.7	12.6
Zirconia	7.7 ± 1.5	0.93 ± 0.04	54 ± 8	3.8 ± 1.0	7.5
Brookite	10.6 ± 4.1	0.92 ± 0.02	44 ± 12	4.0 ± 1.3	6.2
Rutile	5.4 ± 1.4	0.99 ± 0.05	50 ± 15	2.6 ± 1.0	4.4
Alumina	3.2 ± 1.9	0.89 ± 0.01	43 ± 4	1.7 ± 0.2	2.3

Table 2. Photovoltaic parameters obtained for the freshly prepared PSCs (with $CH_3NH_3PbI_3$ = MAPI) fabricated with the different electron selective contacts. The measurements were performed under standard illumination conditions with a scan rate of 50 mV/s in reverse scan direction. Samples marked in red correspond to the configurations chosen for further studies. Average and standard deviation values correspond to results obtained from 4 to 6 solar cells per material.

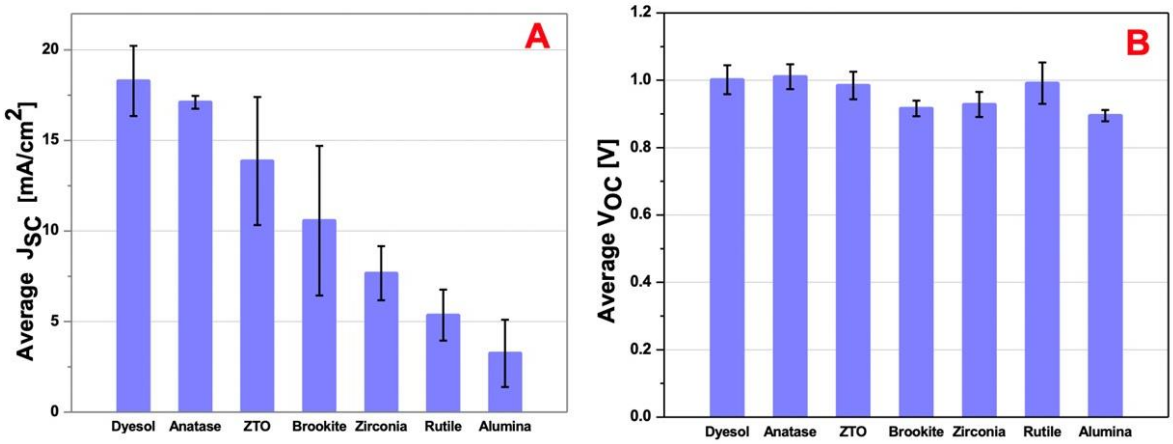

Figure 33. Average J_{SC} (A) and average V_{OC} (B) obtained for 8 devices fabricated with different electron selective contacts.

In order to gain more insight into the origin of these differences in the photovoltaic parameters, further characterization was carried out using optical and IS measurements. To simplify the analysis and work with reliable data, we focus these studies on the four configurations that yield the best performance (marked in red in Table 2). Brookite, rutile and alumina configurations showed significantly smaller efficiencies in addition to limited stability and reproducibility, which complicated the IS analysis.

Figures 34 and 35 display the SEM cross section and the absorbance of MAPI films deposited on the four chosen ESC materials. A similar thickness of the ESC layers and the MAPI perovskite capping layer was obtained for the four materials. The obtained curves for the absorbance of the MAPI films show unambiguously that the nature of the contact does not affect the light-harvesting capabilities of the perovskite active layer. An optical bandgap of 1.6 eV was obtained for the four configurations. This is in accordance with the values reported for MAPI.

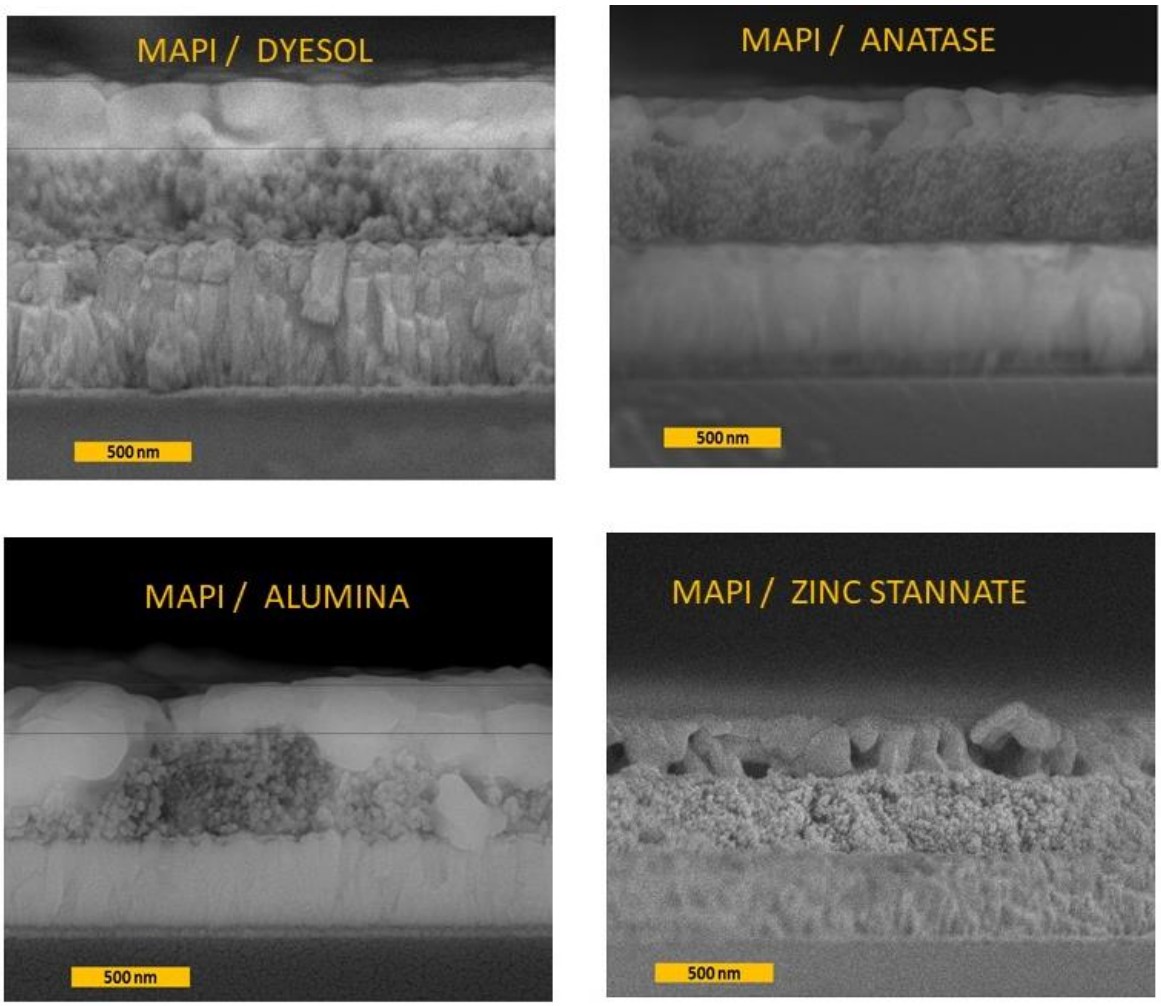

Figure 34. Cross-section of FTO/ compact TiO_2 (not visible)/ mesoporous ESC/ MAPI samples for the four main ESCs studied.

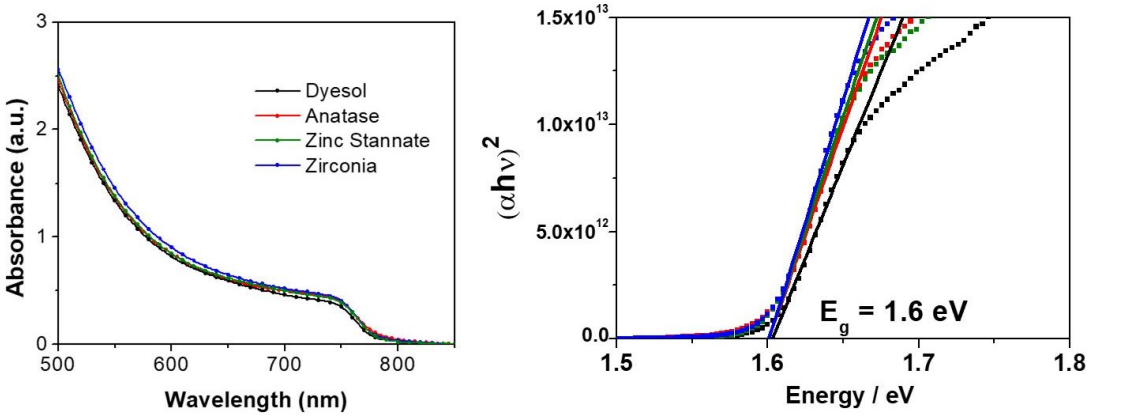

Figure 35 (Right) Absorbance spectra of MHP deposited on the four chosen ESC materials and (left) optical bandgap calculated from the spectra.

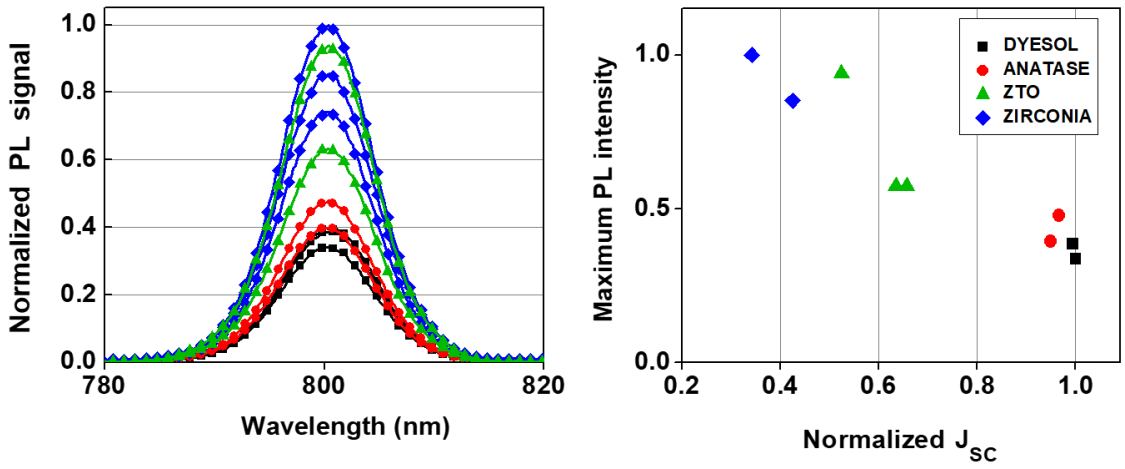

Figure 36. (Left) Normalized photoluminescence spectra of the MAPI films deposited on the different electron selective contacts. **(Right)** The J_{SC} values obtained from the same MAPI films turned into devices is represented against the maximum intensity of the corresponding PL spectrum. Note that, to show the reproducibility of the experiment, data from 2-3 samples of the same configuration are included in the graphs.

The PL spectra feature the typical peak of band-to-band radiative recombination of MHPs with a maximum close to 800 nm.[107,108] The intensity of the peak is a direct measure of the quantum yield for electron injection into the ESC: the lower the peak, the faster the injection kinetics. The results obtained show that *Dyesol* and anatase layers are much more efficient in extracting electrons from the perovskite layer than their ZTO and zirconia counterparts. An inverse correlation (Figure 36, right) was found between the normalized PL intensity at the maximum and the J_{SC} values obtained in the full devices. This correlation, and the independence of the absorbance data with respect to the type of contact, strongly suggests that the lower photocurrent obtained for contacts other than anatase TiO_2 is a direct consequence of poor charge separation due to slow electron injection at the ESC/MAPI interface.

As mentioned above, the nature of the ESC also influences the hysteresis behavior of PSCs. In Figure 37, cyclic voltagramms for the four configurations studied at different scan rates are collected. All devices show “normal” hysteresis, that is, higher fill factor values are

always obtained in the reverse scan, and the difference between reverse and forward scans (hysteresis index) is always larger for faster scan rates. *Dyesol* and anatase exhibit a quite similar hysteresis behavior. In contrast, ZTO and especially zirconia present strong hysteresis. In the latter case, a clear bump is observed at intermediate voltages.

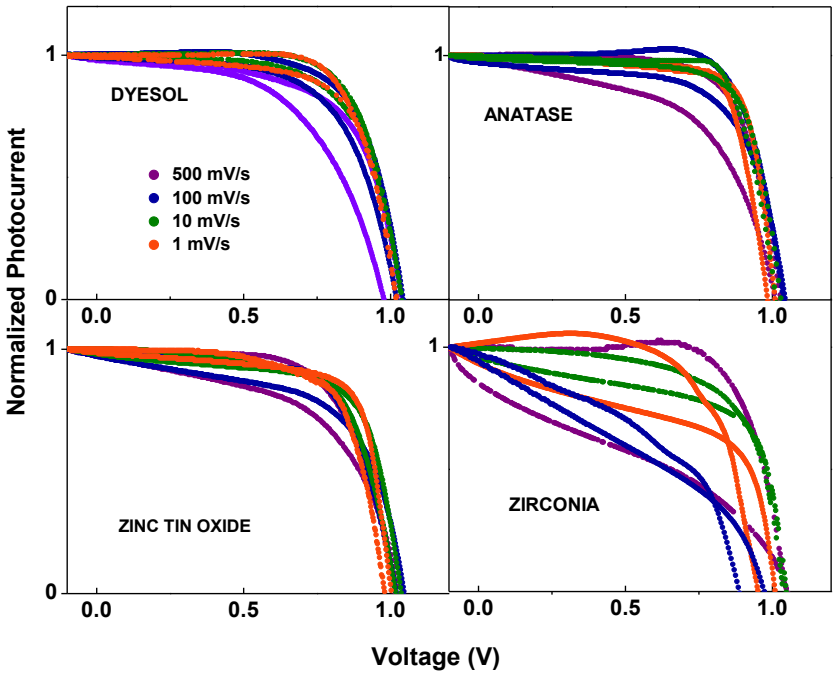

Figure 37. The hysteresis index was calculated from the cyclic voltammetry performed at the different scan rates applying the equation:

$$\boldsymbol{Hysteresis\ Index} = \frac{J_{max\ RS} - J_{max\ FS}}{J_{max\ RS}} \times \mathbf{100} \qquad (5.1)$$

Where $J_{max\ RS}$ and $J_{max\ FS}$ are the values of the current density at the maximum power point in the reverse and forward scan, respectively.

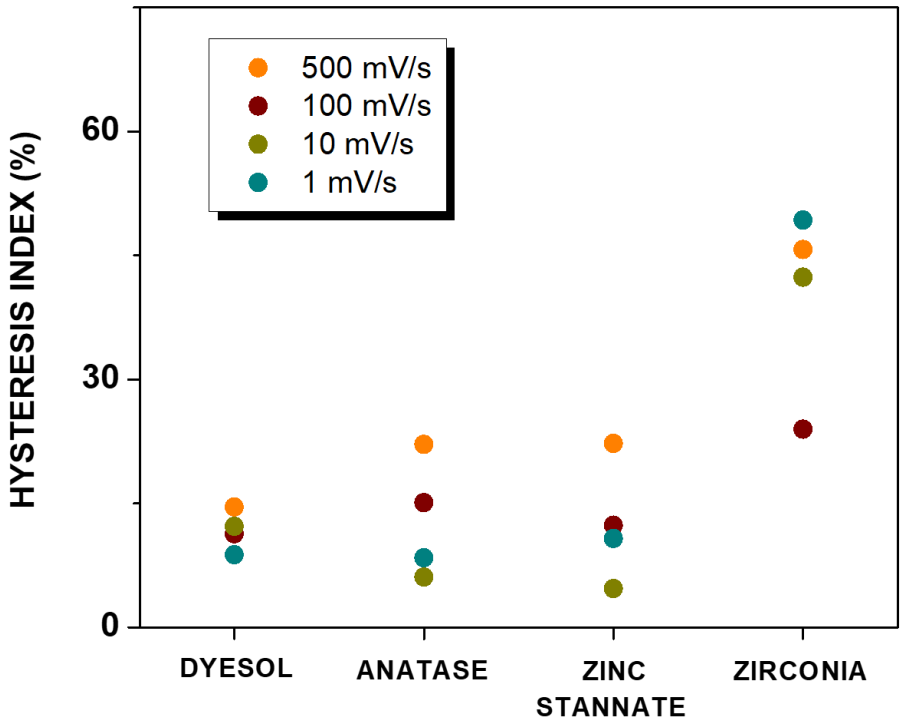

Figure 38. Hysteresis Index obtained from measurements performed at room temperature and at different scan rates: (a) 1 mV/s; (b) 10 mV/s; (c) 100 mV/s; (d) 500 mV/s for the different selective contacts.

Although a precise and unambiguous description of hysteretic phenomena in PSC is still lacking, there is growing evidence that this phenomenon is produced by the combination of the relatively slow motion of the ions[95,109] and interfacial phenomena.[80,110] In these experiments, the perovskite layer is common to all devices and only the electron selective contact is modified. The results show that the nature of the ESC can provoke very different types of hysteresis. The most notorious observation is that for an ESC with a poor electron extraction capacity, such as ZrO_2, the hysteresis is very large. The *J-V* curves obtained for zirconia display a striking resemblance to those obtained before for PSCs with an amorphous TiO_2 contact[96], with substantially lower J_{SC} values and a prominent bump at intermediate voltages. This effect has been previously attributed a poor electron extraction. Interestingly, Wojciechowski and coworkers[107] also found that modifying the TiO_2 surface

to enhance charge separation resulted in devices with higher photocurrents and lower hysteresis.

The short-circuit current density is thus explained to be a consequence of the different extraction capabilities of the devices studied. However, as mentioned before, the photovoltage remains essentially unaltered by the extraction features of the different ESCs. Following previous work,[104,110,111] the device performance under open-circuit conditions was investigated. In Figure 39 the V_{OC} is shown as a function of the temperature of the device. A linear dependence is observed for all four configurations.

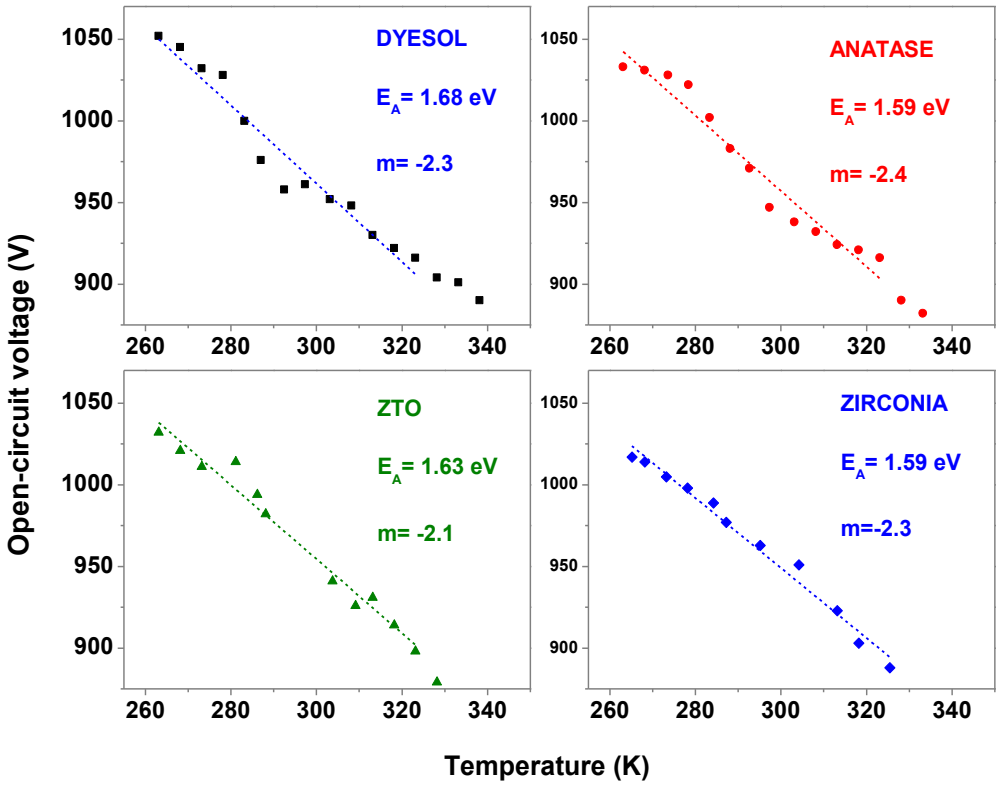

Figure 39. Open-circuit voltage as a function of the absolute temperature for the configurations marked in red in Table 1. In the graph, the results of the fit to Eq. (3) are shown.

$$U_{rec} \approx -\frac{dn}{dt} = k_T p_0 n^{\gamma} \qquad (5.2)$$

where n is the minority carrier concentration in the active layer (electrons for a p-type semiconductor), p_0 is the majority carrier concentration, k_T is a rate constant and γ is the recombination reaction order. It is possible to relate the carrier concentration with the photovoltage, V and the band gap, E_g {Formatting Citation}

$$n = (N_C N_V)^{1/2} exp\left(-\alpha \frac{E_g - qV}{k_B T}\right) \quad (5.3)$$

where N_C and N_V represent the density of states of the conduction and the valence band, respectively. Combining Eqs. (5.2) and (5.3) it is possible to find the recombination rate as a function of open-circuit potential at high injection conditions ($n = p$). Imposing the open-circuit condition (generation rate = recombination rate) one finds from (5.2) and (5.3)[111]

$$V_{OC} = \frac{E_G}{q} - \frac{m k_B T}{q} \ln\left(\frac{J_{00}}{qdG}\right) \quad (5.4)$$

where m, the ideality factor, is given by $m = 1/(\gamma\alpha)$, with $\alpha = 0.5$ for high-injection conditions. Equation (5.4) predicts a linear relationship between V_{OC} and temperature. Figure 39 confirms this prediction and provides an estimation of the band gap of the perovskite. As a matter of fact, all devices yield values very close to the optical band gap of MAPI of 1.61 eV. This outcome indicates that the dominant recombination process quantified by Eq. (5.2) takes place in the bulk of the perovskite or at least it is determined by the perovskite only.[112]

To confirm this interpretation, impedance spectroscopy measurements were carried out under open-circuit conditions. These studies were performed at two optical excitation wavelengths, blue and red light respectively, in order to detect possible spatial

inhomogeneities in the impedance response as was described in more detail in the section "EIS response of PSCs" in Chapter 3. This is especially crucial if we want to assess the impact of the ESC, which is also the front contact. Thus, using blue light (λ_{blue} = 465 nm), most carriers are photogenerated close to and within the mesoporous ESC layer, whereas red light is absorbed throughout the MAPI capping layer. Differences between red and blue light can therefore be a signature of interfacial processes.[96,111]

In Figure 41 impedance spectra for the four selected ESCs are presented. The spectra of the *Dyesol* devices exhibit the typical response[57,76,111,113] of a PSC with two main signals (peaks in the frequency plot or arcs in the Nyquist plot) at low (0.1-10 Hz) and high (10^4-10^5 Hz) frequencies. However, the third signal at mid frequencies shows up for the anatase, ZTO and zirconia devices. Comparison of the "red" and "blue" data reveals that both excitations give in essence the same results for *Dyesol* and ZTO contacts. In contrast, anatase and zirconia reveal clear differences at low and mid frequencies. Given the strong hysteresis observed in devices with anatase and, especially, zirconia contact, this feature and the presence of the mid-frequency signal in the spectra confirms the presence of additional processes in the vicinity of the ESC/MAPI interface. Zirconia gives a larger capacitance with blue light at low frequencies, and the low-frequency limit of the apparent capacitance (Figures 40 and 42) is also larger for zirconia in comparison with the rest of the ESCs. As in Ref.[96], this behavior and the presence of the mid-frequency signal could be related to the poor electron injection efficiency at the zirconia contact. The fact that this shows up at low frequencies combined with the results of the modeling in Ref.[96], points to the important role of ion migration in this process. To quantify and describe this complex interplay between ion migration and surface recombination and the corresponding signature in a small-

perturbation measurement is a challenge that falls outside the scope of this work. However, it is important to stress that the different low-frequency features of the devices do not affect the recombination kinetics that determines the open-circuit photovoltage, which is the main finding of this part of the study. The recombination resistance is the inverse of the voltage derivative of the recombination current derived from Eqs. (5.2) and (5.3)

$$R_{rec} = \left(\frac{\partial J_{rec}}{\partial V}\right)^{-1} = R_{00} exp\left(-\frac{\beta q V_{OC}}{k_B T}\right) \qquad (5.5)$$

with $R_{00} = (k_B T\, J_{00}/\alpha q \gamma)\, \exp(\gamma \alpha E_g/k_B T)$ and $\beta = \gamma\alpha$. From this result, we also get $m = 1/\beta$. This equation predicts an exponential dependence for recombination resistance with respect to open-circuit potential.

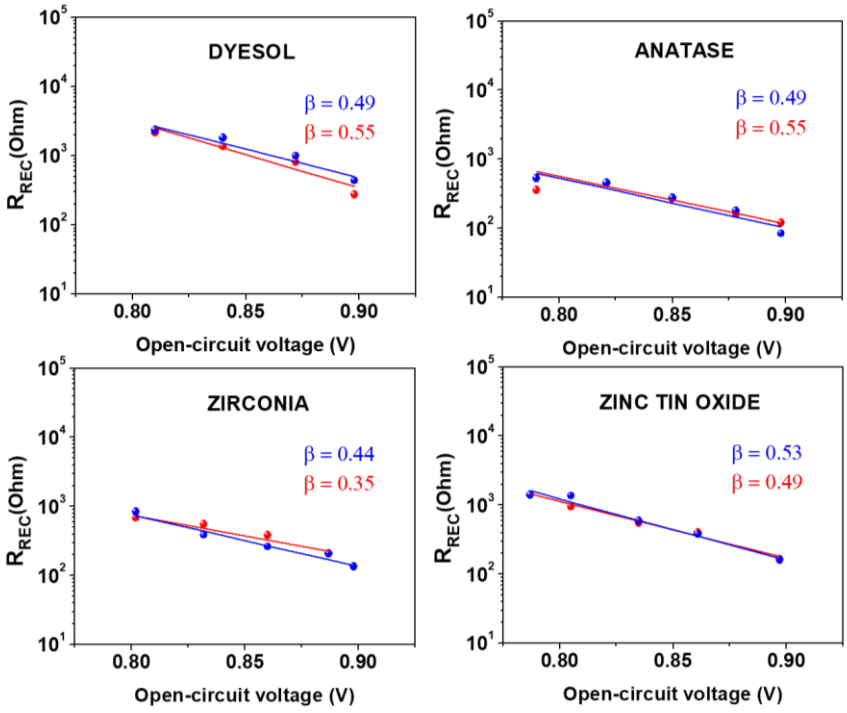

Figure 40. Recombination (high frequency) resistance as a function of the open-circuit potential V_{OC} for the selected configurations marked in red in Table 1, where the V_{OC} is varied by changing the illumination light intensity.

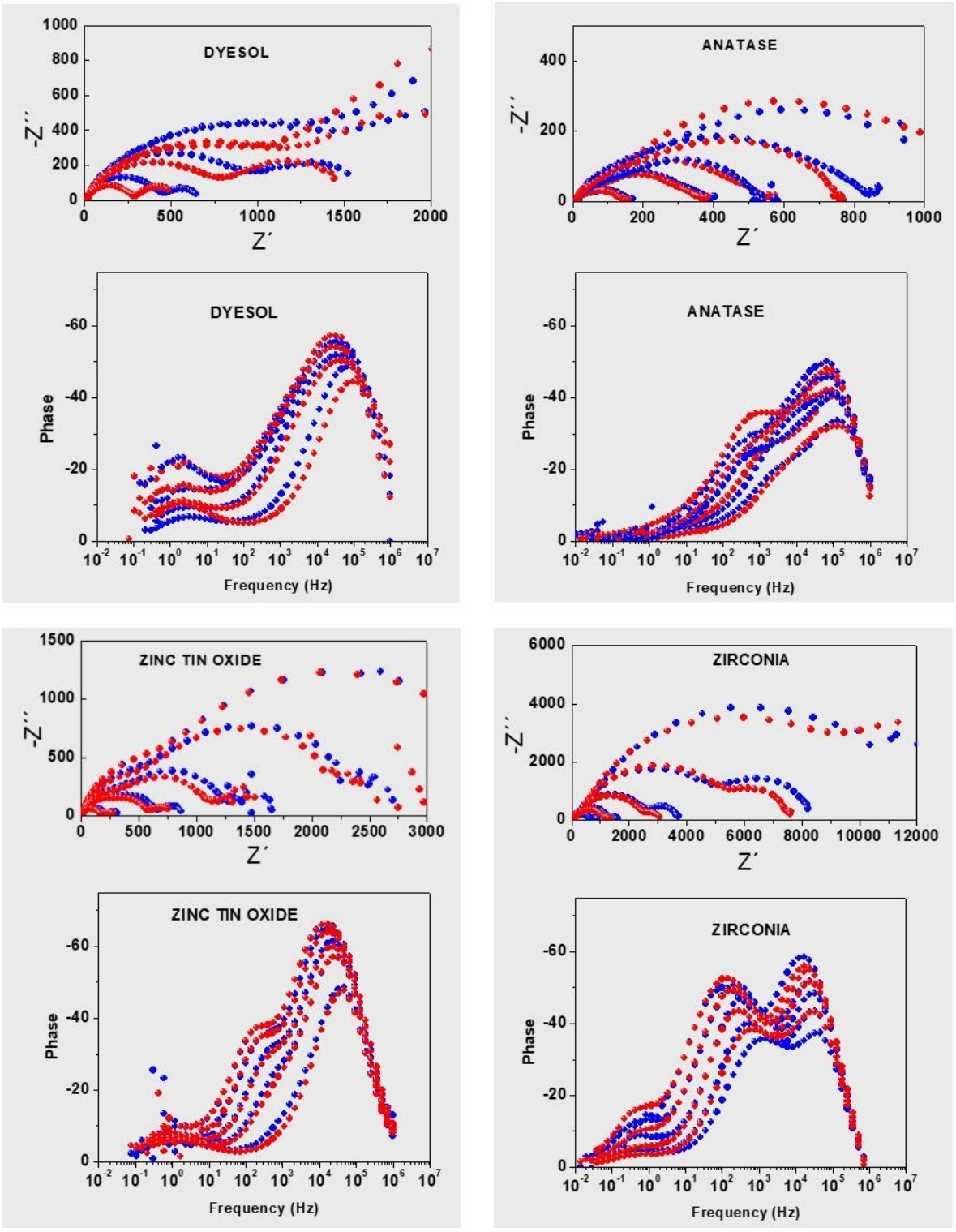

Figure 41. Nyquist and Bode frequency plots showing the impedance response of full solar cells devices with different ESCs. Red and blue lines stand for excitation under red and blue light, respectively.

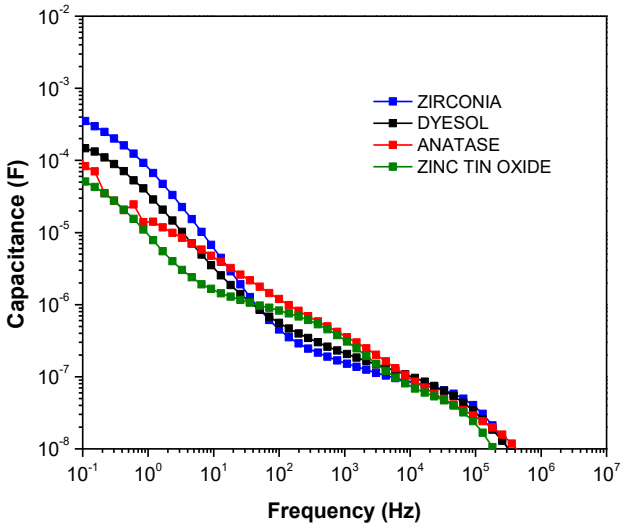

Figure 42. Apparent capacitance at 0.90 V under blue illumination as extracted from the impedance measurements for the four studied ESCs.

It is important to establish how the recombination resistance can be estimated from the impedance spectrum. To do so, the spectra can be fitted[114] to simple equivalent circuits of the tipe $-R_s-[-(R_iCPE_i)-]_{i=1-3}$, that is, as a series connection of RC elements whose number depend on the number of peaks that show up in the spectrum. However, given the complexity of the spectra, in this work we have focused on the high frequency region only. In Figure 40 results for the high frequency resistance as extracted from a simple RC fit of the high frequency peak of the impedance data are presented. The data area plotted versus the V_{OC} for both red and blue light illumination. As predicted by Eq. (5.5) an exponential behavior is clearly reproduced, with a slope that is consistent with $\beta \approx 0.5$ ($m \approx 2$), signature of Shockley-Read-Hall (trap-limited) recombination in the bulk of the perovskite.[111,112,115,116] It is important to remark that only the high frequency component of the impedance spectra reproduces the ideality factor of the V_{OC} measurements, and the similar fits of the mid frequency and low frequency signal do not lead to the correct ideality

factor. This observation can be explained based on the fact that only at high frequencies, where the ionic distribution is *frozen*, pure electronic effects (Eq. (5.2)) are taking place.

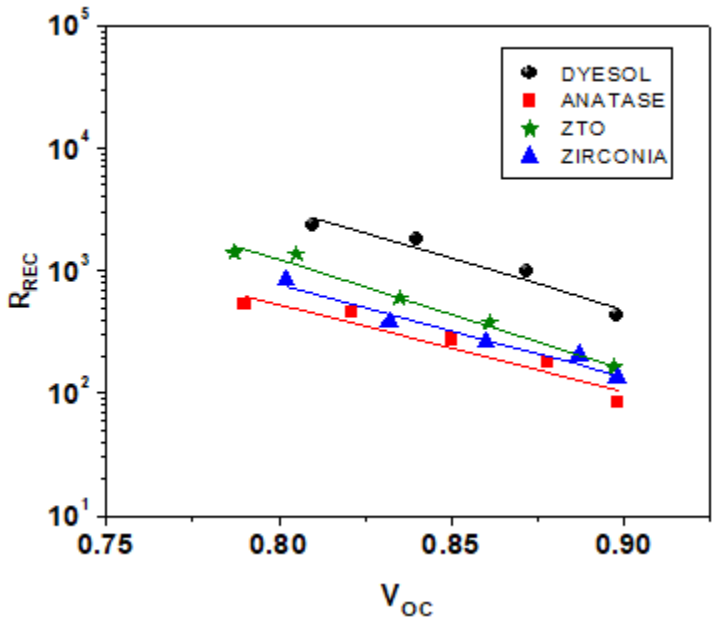

Figure 43. High frequency resistance to recombination under blue illumination for the four ESCs studied.

It is illustrative to compare the recombination resistance of the devices with different ESC materials (Figure 40). In general, a higher 1-sun V_{OC} value (Table 2) is correlated with a higher recombination resistance at the same potential in Figure 40 (corresponding to a lower recombination rate at given Fermi-level splitting). The extreme case is zirconia for which R_{HF} is the lowest. This observation indicates that surface recombination is also having an effect at open circuit if the ESC is not performing well, as it is the case of zirconia. Kirchatz et al.[116] recently discussed the relative impact of surface recombination velocities on the open-circuit photovoltage using up-to-date literature parameters. Although marginal with respect to bulk recombination, surface recombination can account for a

reduction of up to 50 mV in the V_{OC}. Experimental results also confirm that improving charge separation at the electron selective contact, for instance by passivating with a thin layer of a fullerene derivative,[107,117] results in lower hysteresis and improved photovoltaic parameters, in line with what was observed here.

Conclusions

In summary the performance of perovskite solar cells based on electron selective contacts of different chemical nature and crystal structure was measured and analyzed. From current-voltage curves, the temperature dependence of the V_{OC}, and impedance experiments under open circuit conditions, it can be concluded that for all studied contacts, except alumina, the open-circuit photovoltage is essentially the same. This suggests that the open-circuit photovoltage is governed by recombination events that take place in the bulk of the perovskite active layer and is not significantly affected by interfacial. The impact of the electron selective contact is mainly seen in the short-circuit photocurrent. Thus, a correlation is found between the charge extracting capability of each material, as derived from photoluminescence data, and the value actually achieved for the photocurrent. A material with low performance in this respect, such as zirconia, presents the lowest value of the short-circuit photocurrent and a strong hysteresis. Impedance results confirm the bulk nature of the recombination at open circuit in all devices and reveal a quite characteristic behavior at low frequencies for the zirconia-based devices, indicative of additional surface recombination, which leads to stronger hysteresis and lower photocurrent.

CHAPTER 6. EFFECT OF THE HOLE SELECTIVE CONTACT IN INVERTED PEROVSKITE SOLAR CELLS

Introduction and background

Inverted perovskite devices are the result of the successful transference of charge selective layers typically applied in organic photovoltaics to a hybrid perovskite-based device. The denomination "inverted" comes from the order in which hole selective and electron selective contacts are deposited. Contrary to the conventional configuration, the fabrication of inverted PSCs starts with the deposition of a p-type hole selective contact on a transparent conductive oxide; the perovskite absorber is deposited on top of the hole selective contact followed by the electron selective contact.

Jeng et al. were the first to report a device with an inverted configuration in 2013.[118] The structure and the band energy diagram of this device are depicted in Figure 44. The material PEDOT:PSS was used as the hole selective contact in accordance with the typical structure of OPV devices and [6,6]-phenyl C61-butyric acid methyl ester (PCBM) was used as the electron selective contact. A film of bathocuproine (BCP) was deposited on top of the electron selective contact. BCP plays the role of a buffer layer between the n-type semiconductor layer and the metal electrode.[119,120]

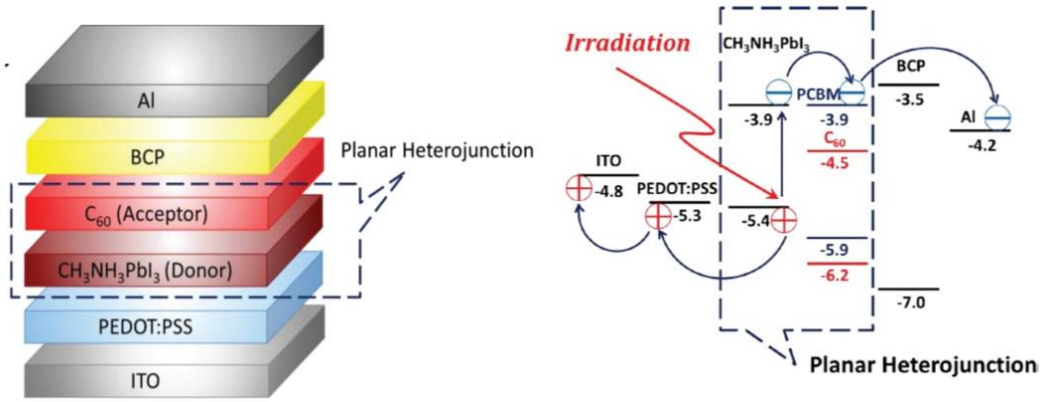

Figure 44. Structure and energy diagram of an inverted perovskite device as reported by Jang et al. subsequent modifications included the replacement of the hole selective contact PEDOT:PSS by NiO_X (Jen et al., $CH_3NH_3PbI_3$ perovskite/fullerene planar-heterojunction hybrid solar cells).[118]

The first attempts of transferring the perovskite as an absorber material into the p-i-n structures resulted in modest efficiencies of less than 10%. This was often interpreted as the result of the insufficient thickness of the perovskite film, reported at less than 100 nm on the hole selective contact.[118,121] Since then, inverted perovskite cells have benefited from the optimization of solution-based perovskite synthesis. In addition to the improved quality of the perovskite film, interface engineering, especially between the hole selective contact and the perovskite absorber, has resulted in current record efficiencies of 20.7%.[122]

The initial hole selective contact, PEDOT:PSS was characterized by the formation of thin perovskite films and poor band alignment. Both issues reflected in the current and photovoltage values being lower than the characteristic values of conventional hybrid perovskite devices. The functionalization of PEDOT:PSS reduced these limitations and the configuration of PEDOT:PSS/MAPI/PCBM for inverted perovskite solar cells reached an efficiency of 18% by 2015.[123]

However, an additional restraint of PEDOT:PSS-based devices is their stability. PEDOT:PSS is a hygroscopic material and is characterized by a high level of acidity; both of these characteristics are detrimental to the long term stability of the perovskite solar cells.[47]

In Figure 45 the variety of materials used as hole and electron selective contacts in inverted perovskite cells is presented. Although there are other organic hole selective contact, such as polythiophene and poly-TPD, with the potential to perform efficiently, organic alternatives to PEDOT:PSS are usually damaged by the solvents employed in the synthesis of the perovskite absorber and can only be applied if the perovskite is deposited by vacuum evaporation.

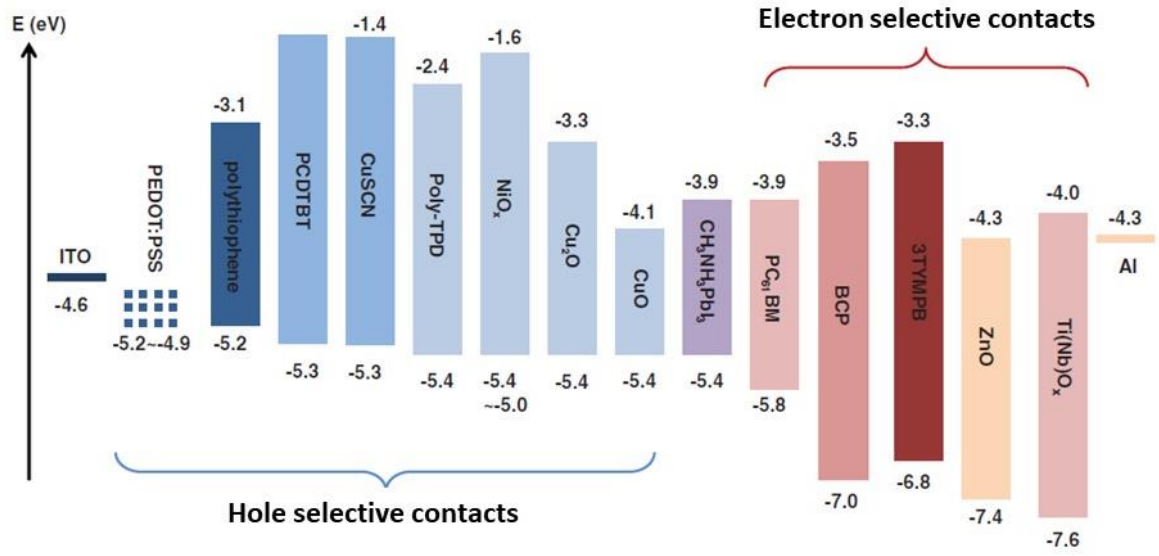

Figure 45. Materials used as hole and electron selective contacts in inverted perovskite solar cells.

Inorganic hole selective contacts such as CuO and Cu_2O have also shown good energy level alignment with the HOMO level of $CH_3NH_3PbI_3$, but they have so far only been explored for the conventional configuration of perovskite solar cells.[124,125]

One of the limitations of looking for a p-type semiconductor oxide to work as hole selective contact is the transparency of the materials once deposited as a film. The p-type oxide NiO_X has been the most successful inorganic hole selective contact applied so far in inverted perovskite solar cells. Both NiO_X and PEDOT:PSS present a higher quenching of the photoluminescence signal, evidencing their better capacity for hole extraction than the material typically used in the regular configuration of PSCs, spiro-MeOTAD.[47]

Initial studies with NiO_X exhibited the difficulty to obtain a sufficiently thick perovskite layer on the NiO_X film. Snaith an Yang et al. were the first to achieve a thicker capping layer, achieving performances of 11.5% and 9.8 %. [126] In fact, also in the field of organic photovoltaics, NiO_X has resulted in devices with good performance. In addition, stability is better when NiO_X is used when compared to PEDOT:PSS.[47]

In the work by Guo et al., it was noted that low fill factor values are obtained for the devices based on NiO_X as hole selective contact, compared to PEDOT:PSS. This was attributed to the limited p-type conductivity of NiO_X.[127,128] In this regard, mechanisms such as doping or adding functionalized layers have been explored to improve the performance of this part of the cell. [129,130]

As the vast amount of information on hybrid perovskite photovoltaics has shown, interfacial characteristics often dictate the level of performance of the devices. Research on

the NiO_X-based inverted perovskite solar cells has focused on different methods of synthesis and deposition of the NiO_X layer. [48,129,131–134] Lower values of the photovoltage in inverted perovskite solar cells is a common issue, related to the considerable density of defects or recombination centers. The reduction of non-radiative recombination has also been pursued. Some of the ways explored to achieve better performance include control of grain size and heterojunction engineering.[127,135,136] So far NiO_X has been reported in planar and mesoscopic inverted perovskite solar cells and its main advantage over PEDOT:PSS is the demonstrated superior stability. [18, 21–23] As for the advantages that inverted perovskite solar cells offer and motivate its research despite the higher efficiencies achieved by the conventional devices, these are mostly related to the lower degree of hysteresis that is often observed for the inverted configuration.

As described in Chapter 3, two of the more plausible theories to explain the origins of hysteresis are related to trapping and detrapping of charges and ion migration occurring in the perovskite film under solar cells operating conditions. It has been reported that the lower degree of hysteresis found in inverted devices may be related to the perovskite /electron selective contact (PCBM) interaction and its effect on traps and ionic migration. The deposition of PCBM is accompanied by its diffusion into the perovskite layer through the pinholes and grain boundaries during processing (spin-coating or annealing). Mobile ions in the perovskite interact with fullerene to form a fullerene halide radical, which is thought to stabilize electrostatic properties. It is also possible that the interdiffusion of the PCBM in the perovskite has a passivating effect on the defects and grain boundaries that contribute to the hysteresis. It has also been reported PCBM has a superior capacity for the extraction of electrons than TiO_2 (figure 46), the fast charge transfer between perovskite

and fullerene avoids the accumulation of charge.[139] All these factors originating from the advantageous perovskite/PCBM interaction could explain the low degree of hysteresis in inverted devices.

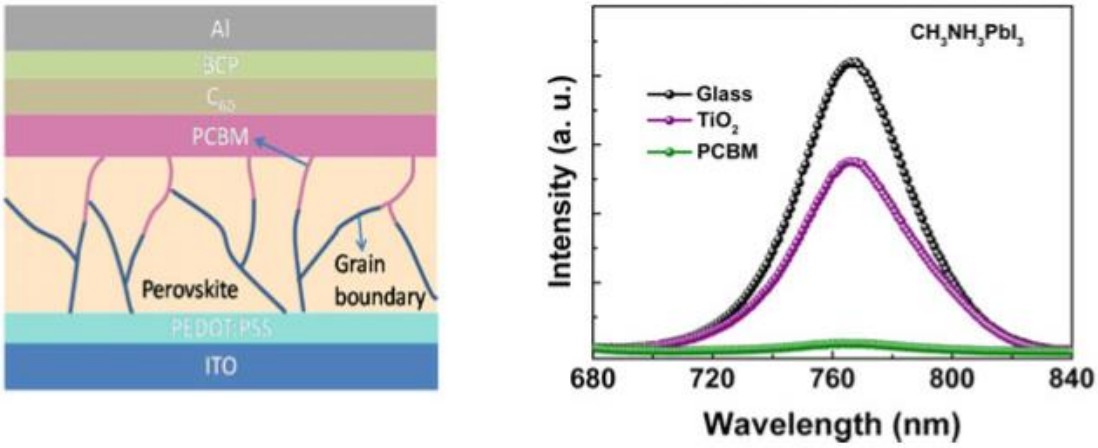

Figure 46. (Left) Schematic illustration of the interdiffusion of PCBM into the perovskite film after spin coating. (Right) Quenching of the PL signal for different interfaces. The higher quenching for the interface PCBM/perovskite relative to the interface TiO_2/perovskite is evidence of the superior electron extraction capacity of the PCBM material (Shao et al., Origin and elimination of photocurrent hysteresis by fullerene passivation in $CH_3NH_3PbI_3$ planar heterojunction solar cells) . [139]

As described in the methodology, for this part of the work, the nature of the p-type NiO_X was modified with the purpose of studying the effect of the morphology, and the general role it plays in the performance of the inverted perovskite solar cells. Planar and mesoporous configurations of the inverted device were studied using electrochemical impedance spectroscopy. Finally, a study of the hysteresis response at different scan rates was performed including the planar and mesoporous inverted solar cells studied in this chapter, as well as samples of conventional mesoporous TiO_2-based perovskite solar cells in order to compare the hysteretic behavior of both configurations.

Results

Spray pyrolysis of NiO_X film

As a first step, the spray pyrolysis method was explored as an alternative technique to spin coating to deposit NiO_X as the hole selective contact in planar inverted devices. Figure 47 summarizes the effect of different spray pyrolysis conditions on the performance parameters of the planar devices. The results of the spray pyrolysis experiments are compared with those obtained for the optimized spin coated NiO_X. It was found that the optimal conditions of deposition were 30 cycles of spray pyrolysis of a 5mM NiO_X precursor solution achieving an average performance similar to that of spin-coated NiO_X.

Although both J_{SC} anc V_{OC} improved after increasing the number of cycles of the 5 mM precursor solution but a further increase in concentration and number of cycles was detrimental to the V_{OC} and J_{SC} parameters. The average performance of the NiO_X devices prepared by spray pyrolysis was 10.3% with the best devices achieving an efficiency of 12.4%.

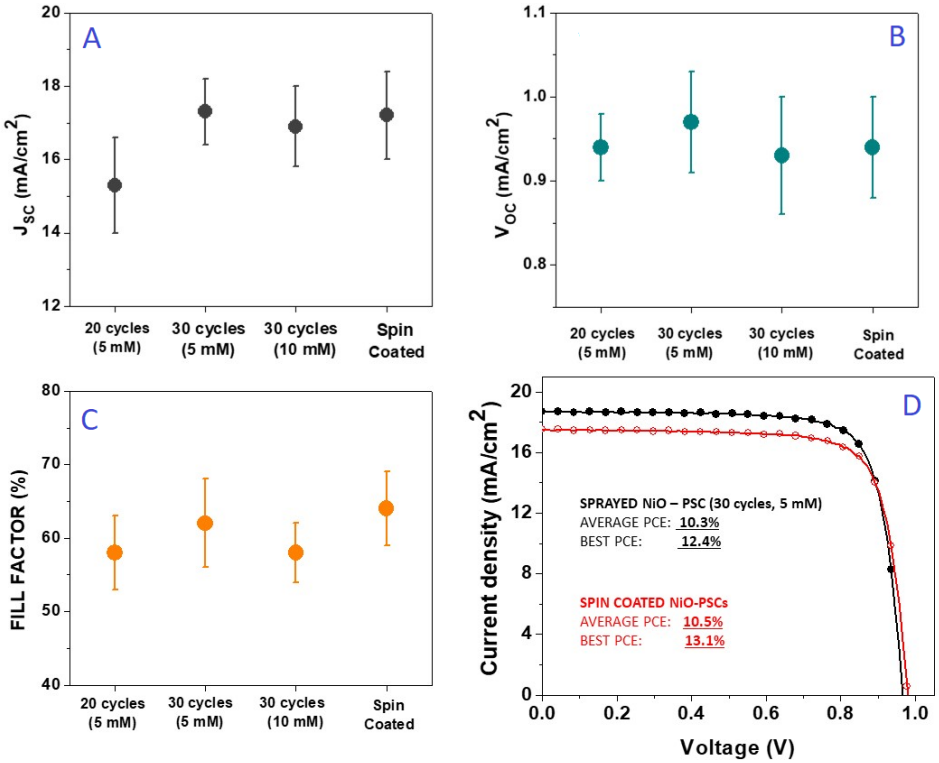

Figure 47. Average values of J_{SC}, V_{OC} as a function blocking layer deposition method and conditions. Different precursor solution concentrations and number of cycles were evaluated and compared to films prepared by spin coating. Figure D shows the J-V curves of the best cells obtained for each method.

Mesoporous NiO_X film

The p-type contact was further modified by the deposition of a mesoporous NiO_X film. The thickness of the mesoporous film was varied using dilutions of a commercial NiO_X paste. Figure 48 includes a summary of the performance as a function of the thickness of the NiO_X film. The optimal thickness was found to be approximately 240 nm.

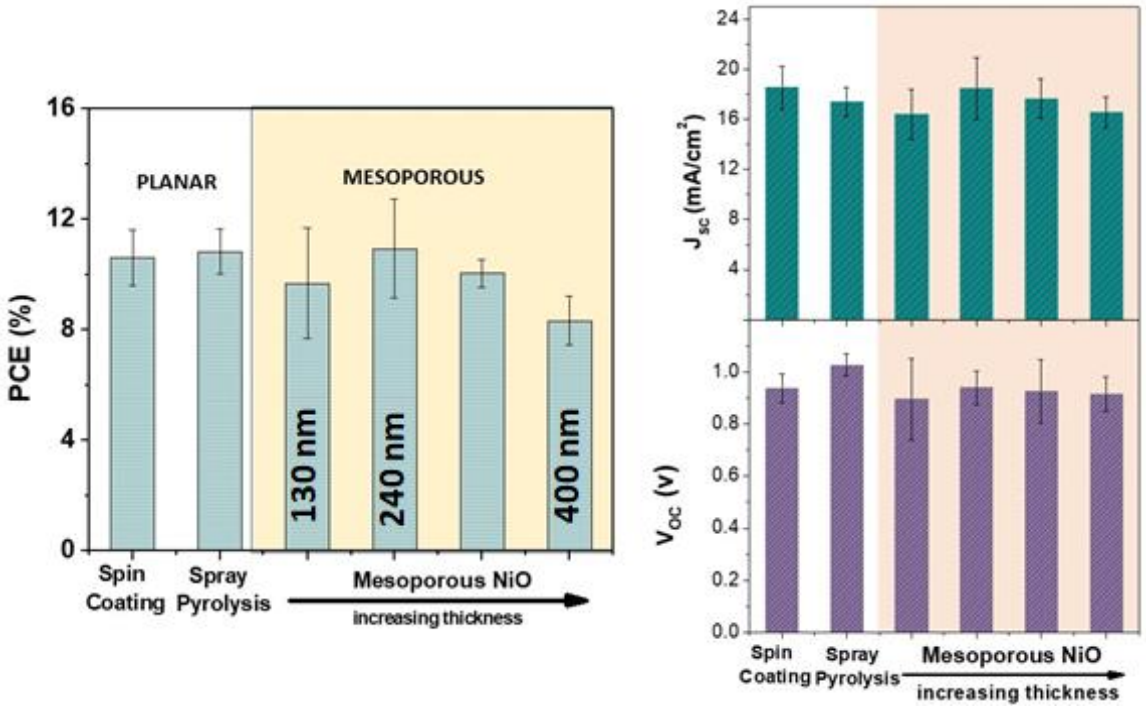

Figure 48. The optimization of the conditions of deposition of the mesoporous NiO_X film resulted in the trends showed in the figure. An optimal thickness was found for the m-NiO that was approximately 240 nm. The performance of the optimized mesoporous devices and planar devices was very similar.

To further investigate the origin of the performance differences, the morphology and the thickness of the perovskite capping layer of the perovskite deposited on top of planar and mesoporous devices was evaluated using SEM. The SEM images obtained for the perovskite deposited onto the NiO_X planar and mesoporous films showed a difference in the thickness of the perovskite absorber capping layer (Figure 49). The capping layer on the mesoporous devices had a thickness of approximately 320 nm while the MAPI film formed on top of the planar NiO_X film was approximately 230 nm. Although a slightly higher current value is found in the current of the best performing mesoporous devices (see figure 48) the average performance is very similar among mesoporous and planar devices.

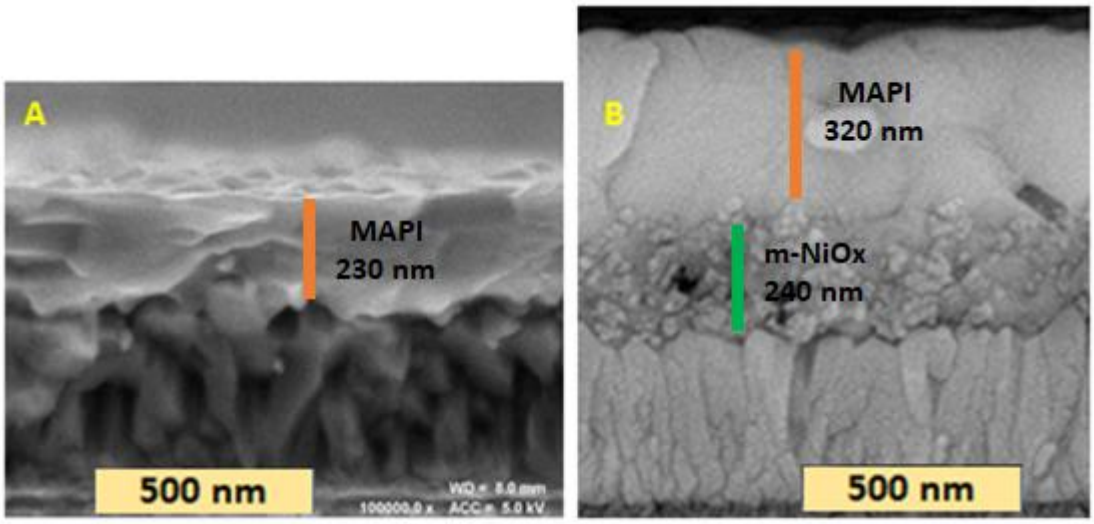

Figure 49. Cross section of (A) the MAPI film deposited on top of the compact NiO_X layer and (B) the MAPI film deposited on top of the NiO mesoporous film.

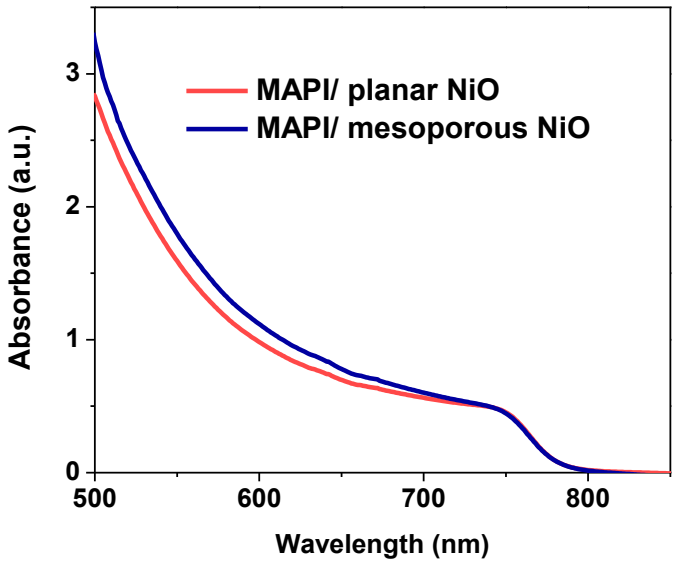

Figure 50. Absorbance spectra of the MAPI film deposited on the planar and mesoporous NiO_X films.

EIS response

To further investigate the effect of the differences in the NiO_X films in the performance of the devices, electrochemical impedance spectroscopy was performed. Figure 51 shows the Nyquist and the Bode plots obtained for the three types of device studied.

The device fabricated with a blocking layer by spin coating presents three semicircles in the Nyquist plot, while the Bode clearly shows three differentiable processes. The planar devices prepared by spray pyrolysis and the mesoporous devices do not show the three processes at different frequencies, however for the NiO_X device prepared by spray, the MF semicircle seems to be convoluted and it is difficult to differentiate between the processes occurring at different frequencies.

The semicircle found at mid-frequencies in the Nyquist plot does not have a clear origin and it does not appear for all perovskite devices. It has been ascribed to additional surface recombination processes due to poor electron extraction efficiency or related to ion migration. However, in these devices the ESC-perovskite interface has not been modified.

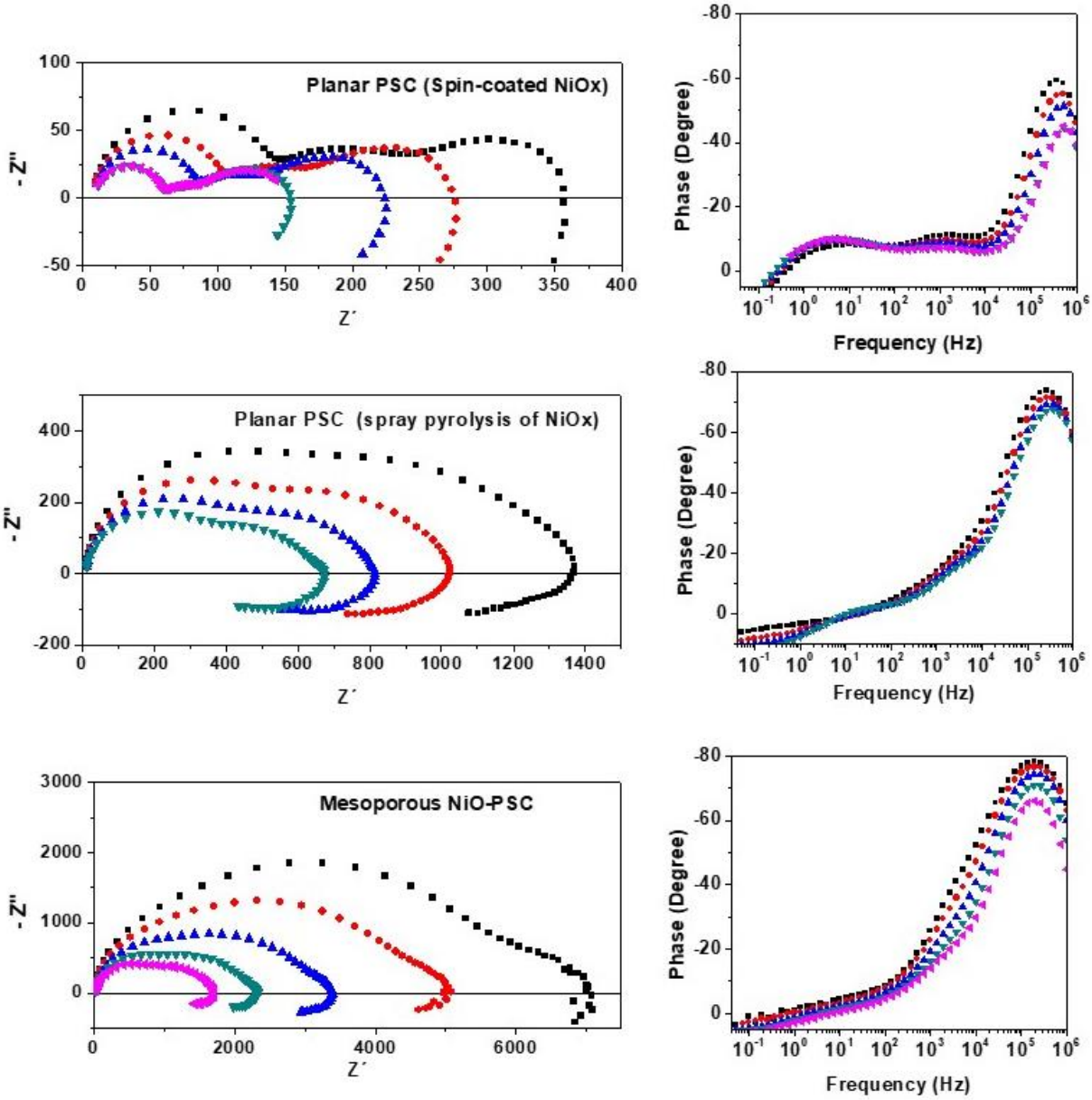

Figure 51. Nyquist and Bode plots obtained for the devices based on the three types of NiO_X selective contacts. The graphs show the impedance response at different light intensities under blue LED illumination, with the lowest intensity corresponding to the black curves.

+

Hysteresis

The hysteresis study described in this section was performed in the inverted perovskite solar cells. It consisted in a more detailed study of hysteresis, with a larger number of scan rates testes than the hysteresis study performed for the different ESC in conventional devices; for this reason, additional samples of conventional mesoporous solar cells with TiO_2 as the ESC were also fabricated and their hysteresis characterized with this procedure to be able to compare the hysteric behavior between both configurations.

As detailed in the methodology, for this part of the study, cyclic voltammetries were measured at scan rates varying from 2 mV/s to 7000 mV/s. The hysteresis index was calculated for each scan rated using the expression:

$$Hysteresis\ Index\ (HI) = 100 * \left(\frac{A_{reverse\ scan} - A_{forward\ scan}}{A_{reverse\ scan}}\right) \qquad (6.1)$$

Where *A* refers to the area under the *J-V* curve. Hysteresis is a typical behavior of perovskite solar cells and it is commonly reported that the reverse scan (V_{OC} to J_{SC}) generally results in a higher apparent performance than the forward scan, therefore, by using the expression 6.1, this typical or normal hysteresis will result in a positive hysteresis index. The opposite case of inverted hysteresis also exists but is significantly less studied.

The hysteresis of several of the best performing devices was measured according to the procedure detailed in the methodology. Regardless of the type of NiO_X used as the hole selective contact, planar and mesoporous inverted devices predominantly presented a

negative value of the hysteresis index or an "inverted" hysteresis. As for the magnitude, a small degree of hysteresis was found at the slowest scan rate values.

It is important to note that results on low or non-existent hysteresis are frequently reported for a single scan rate value. Inverted perovskite solar cells showed hysteresis in previous reports, for example, when conditions of low temperature are applied. [140]

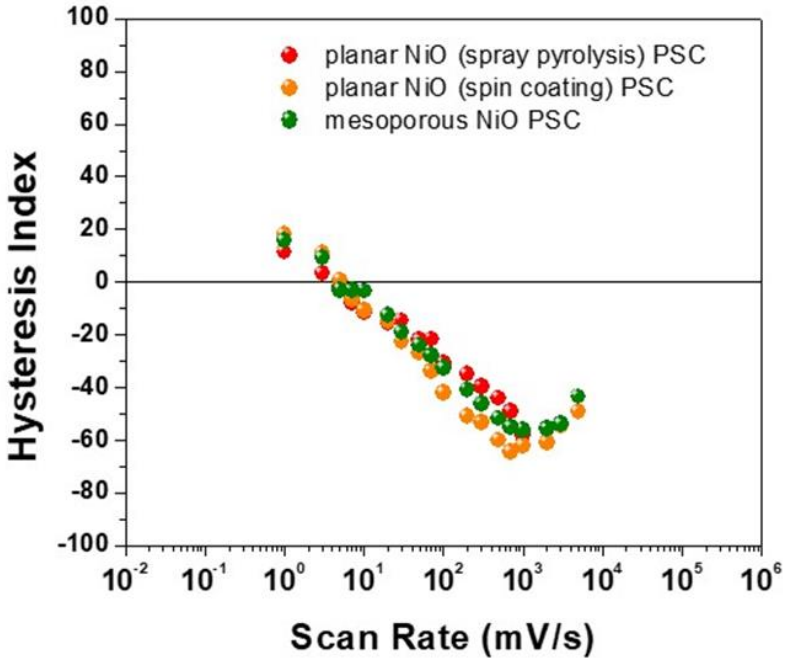

Figure 52. Hysteresis Index as a function of scan ratefor the different inverted devices prepared with mesoporous and planar NiO_X.

To get a better picture of this phenomenon, the hysteresis of conventional mesoporous TiO_2-based devices was measured under the same conditions. The results are shown in Figure 53. Despite measuring devices with similar efficiencies the behavior differs between the conventional TiO_2 cells but the main result is the predominance of normal hysteresis for

the majority of scan rates. Lower values of hysteresis were found both at very slow scans and at fast scans.

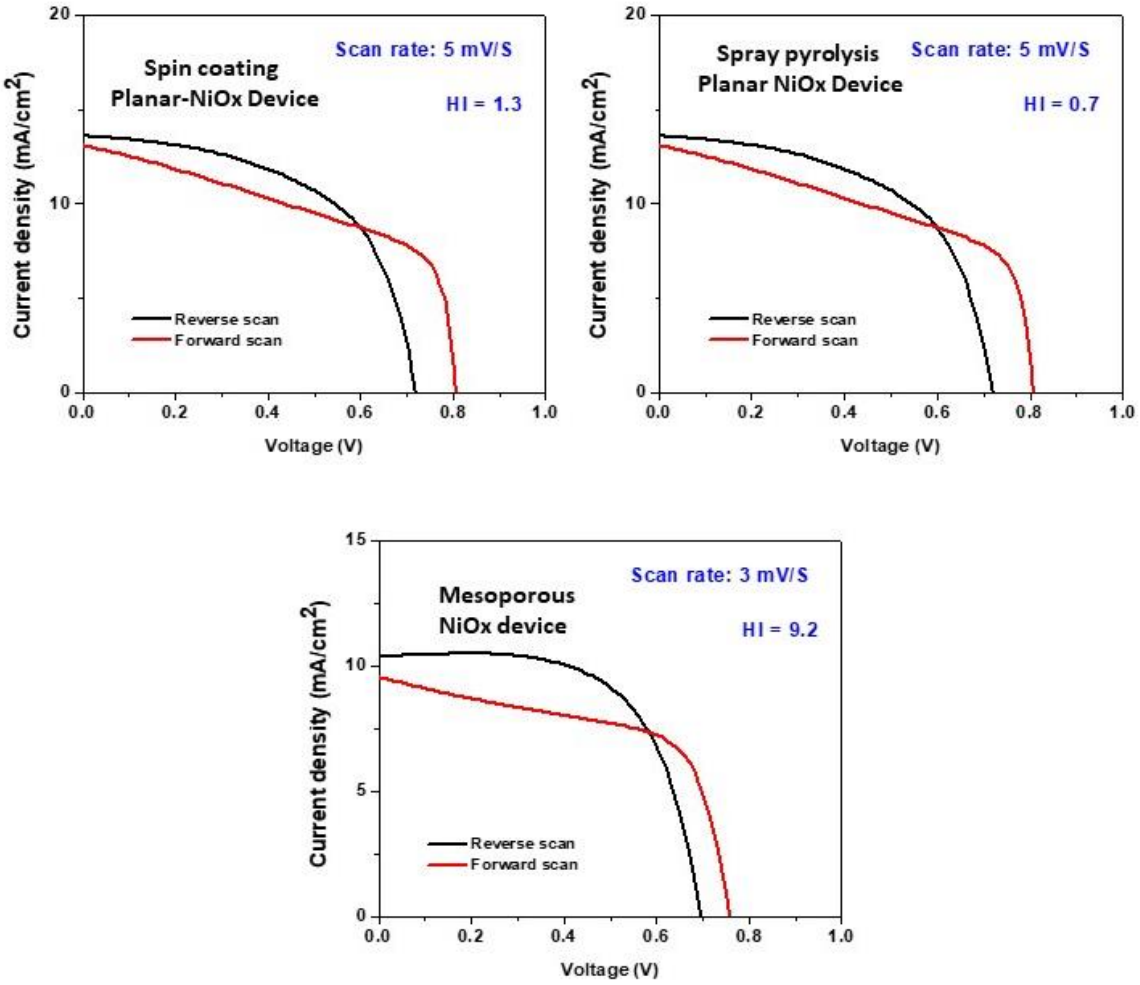

Figure 53. J-V curves showing the inverted hysteresis at slow scan rates for the three inverted configurations. The smallest values for the hysteresis index were obtained from the measurements performed at the slowest scan rates.

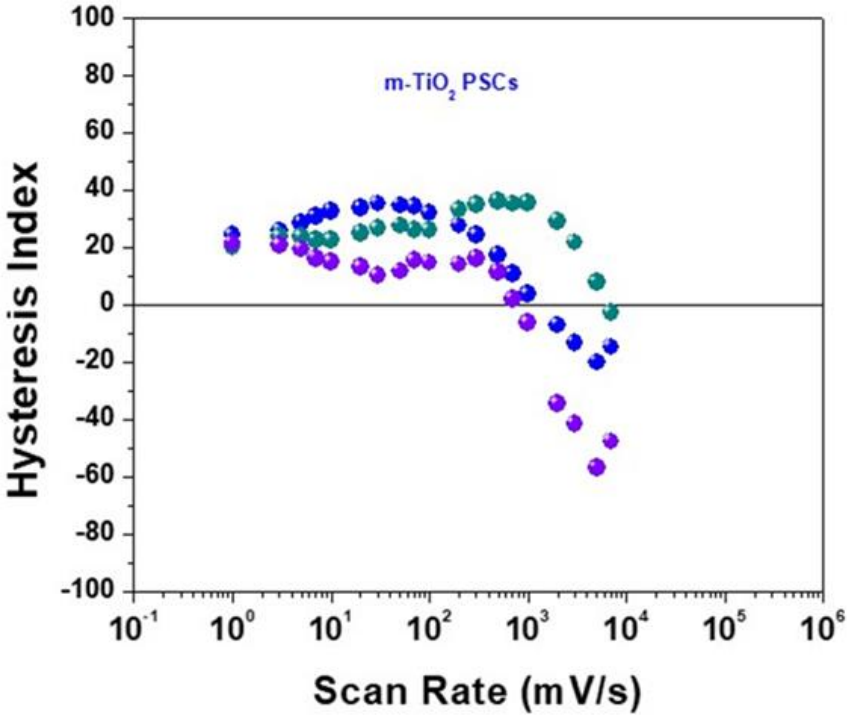

Figure 54. Hysteresis Index as a function of scan rate for samples of conventional mesoporous TiO_2-PSCs

The manifestation of the hysteresis is also different between conventional and inverted devices. Figure 54 shows the behavior of J_{SC} and the V_{OC} across the scan rate sweep. The degree of hysteresis for inverted devices is caused by the difference in voltage between the forward and the reverse scan, with the forward scans consistently showing a higher open circuit photovoltage, while the values of the short circuit current are the same in both scan directions. Conventional devices, on the other hand, have similar J_{SC} and V_{OC} at all scan rates. The degree of hysteresis in the case of conventional mesoporous devices is caused by the difference in the fill factor, which is lower for the forward scan.

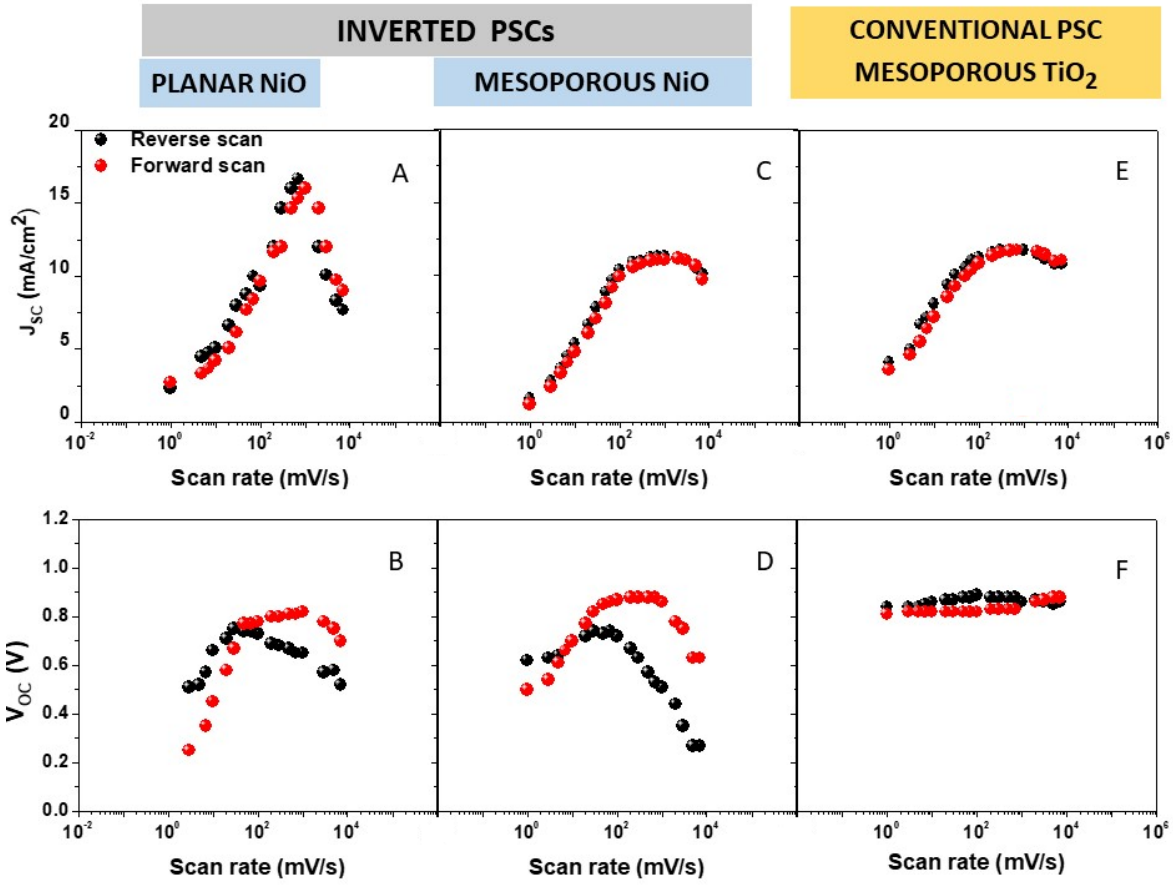

Figure 55. Evolution J_{SC} and V_{OC} with scan rate for inverted and conventional devices

Reports on inverted hysteresis are often related to measurement conditions and there is little information available related to the dependence of hysteresis upon scan rate for inverted perovskite solar cells. [77,141] There are, however, indications that the interface between the perovskite and the electron selective contact (PCBM) could be part of the explanation. Erdenebileg et al. reported inverted hysteresis when an n-doped fullerene was applied as electron selective contact in an inverted device. The anomalous inverted hysteresis was attributed to a space-charge build-up at the perovskite/ESC interface. [142,143]

The independence of the hysteresis on the nature of the HTL also points to this phenomenon origin to the perovskite/ETL interface. Although a descriptive explanation for the inverted hysteresis is out of reach based on the data obtained by this study, the results suggest that the particular interaction between PCBM and MAPI that has been pointed as beneficial for the reduction of hysteresis could also be responsible for modifying the ion migration dynamics responsible for the hysteresis, resulting in a behavior completely different from the hysteresis originating in conventional devices with a typical TiO_2/perovskite interface.

Conclusions

In summary, planar inverted perovskite solar cells have been fabricated by spray pyrolysis of the NiO_X hole selective contact. The deposition technique was optimized and efficiencies comparable to devices fabricated with spin-coated NiO_X were obtained.

Mesoporous NiO_X-inverted PSCs were fabricated by the deposition of a commercial NiO_X film on the compact NiO layers previously fabricated. The deposition method was optimized, reaching efficiencies similar to the optimized planar devices. The average efficiency of all inverted devices was between 10% and 11% with the best performing devices reaching between 12% and 13%.

The impedance response and degree of hysteresis of the three types of devices were probed to investigate the effect of varying the morphology of the p-type contact in the recombination dynamics of the inverted devices. In the impedance response, a mid-frequency process resulting in a semicircle in the Nyquist plot for the planar spin-coated

devices disappears or is convoluted with the high-frequency semicircle for the spray-deposited planar and the mesoporous devices. There is little insight on the significance of the MF semicircle in PSCs and it is not always observed in the characterization of perovskite devices. Similar to the case of anatase in the previous chapter, this semicircle could indicate an additional recombination pathway, and the modification of this response for the different inverted devices suggests that recombination dynamics are altered by the changes in the interface between the NiO_X hole selective contact and the perovskite interface, however, this is not reflected in the performance of the devices.

The hysteresis index for the inverted perovskite solar cells was found to be predominantly negative, in contrast with the normal hysteresis measured for conventional mesoporous TiO_2-devices. The interface NiO_X /MAPI have no effect on the phenomena originating hysteresis since the negative hysteresis behavior was consistent and highly reproducible among the three types of NiO_X films studied (spin coated, spray-deposited, mesoporous), instead, the interface between the MAPI/PCBM could be the cause for this markedly different behavior between inverted and conventional devices.

SUMMARY AND GENERAL CONCLUSIONS

In summary, the performance of conventional and inverted hybrid organic-inorganic metal halide perovskite solar cells based on electron and hole selective contacts of different nature has been studied and analyzed in detail.

A correlation was found between the charge extracting capability of the materials functioning as electron selective contacts in conventional devices and the photocurrent obtained in the solar cells. However, the open-circuit photovoltage is essentially the same among the electron selective materials studied because it is governed by recombination events that take place in the bulk of the hybrid perovskite active layer. The impact of the electron selective contact is hence mainly seen in the short-circuit photocurrent.

The study of the hole selective contact in inverted planar and mesoporous devices resulted in very similar performance indicating that the dynamics of this type of devices is dominated by bulk properties in the same way as for conventional devices. The difference between the mesoporous and planar morphologies of the NiO_X hole selective contact does not seem to affect the material´s capacity for charge extraction, resulting in devices with very similar current and photovoltage values.

The characterization of hysteresis resulted in very different behavior between conventional and inverted devices. Since the performance of the cells is very similar regardless of the nature of the p-type hole selective contact, it is suggested that the difference in the

performance manifested by the hysteresis could stem from the different nature of the electron selective contact/perovskite interface between inverted and conventional devices, where the ion migration dynamic is altered by the passivation of grain boundaries and defects when PCBM is used.

APPENDIX. CHAPTER 5

A5-1 Procedure followed for the fabrication of conventional mesoporous perovskite solar cells.

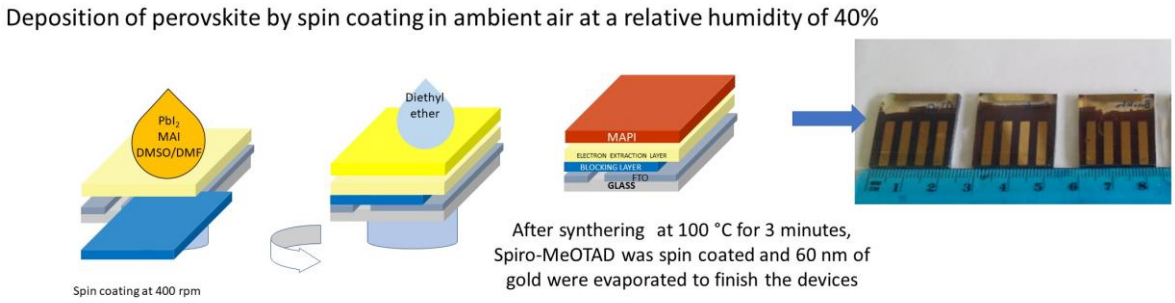

Figure 56. Fabrication of perovskite solar cells under ambient conditions.

A5-2 Short circuit current box plots - conventional mesoporous solar cells.

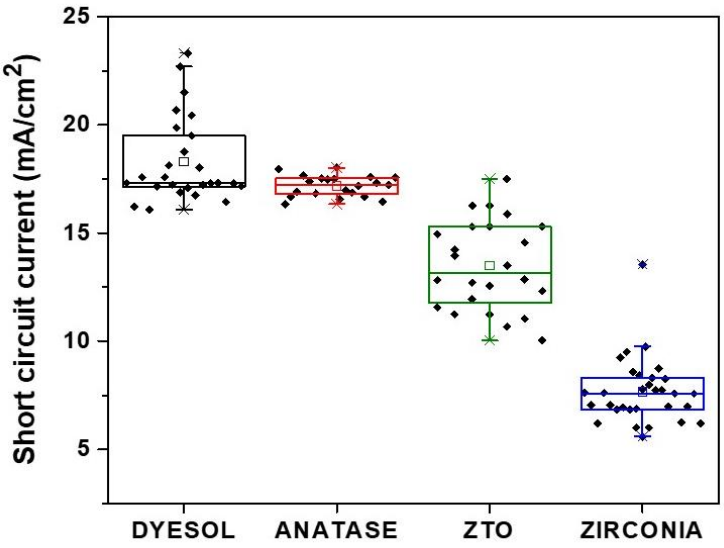

Figure 57. Short circuit current box plots show the distribution of perovskite solar cells with different electron selective contacts.

A5-3 Blocking layers deposited by spray pyrolysis and atomic layer deposition (ALD)

Before substituting TiO_2 blocking layers deposited by spray pyrolysis with blocking layers deposited by ALD, an experiment was carried out to study the possible effect of this variation in the performance of the devices. A group of solar cells with the configuration FTO/compact TiO_2/ mesoporous TiO_2 (Dyesol)/MAPI/Spiro-OMeTAD/Au was fabricated to test both types of compact layers. The compact layers and the devices were fabricated following the experimental procedures previously described.

The J-V curves obtained for the fabricated devices are shown in Figure 57. The performance of the devices summarized in Table S1 shows that the average values of the photovoltaic parameters were not significantly affected by the type of compact layer used.

PSCs	J_{SC} [mA/cm^2]	V_{OC} [V]	PCE [%]	FF [%]
SPRAY PYROLYSIS	17.1 ± 0.9	1.02 ± 0.02	12.4 ± 0.8	71 ± 5
ALD	16.7 ± 0.6	1.04 ± 0.02	12.5 ± 0.9	72 ± 6

Table 3. Average performance of mesoporous MAPI-perovskite solar cells fabricated with compact layers deposited by spray pyrolysis and ALD.

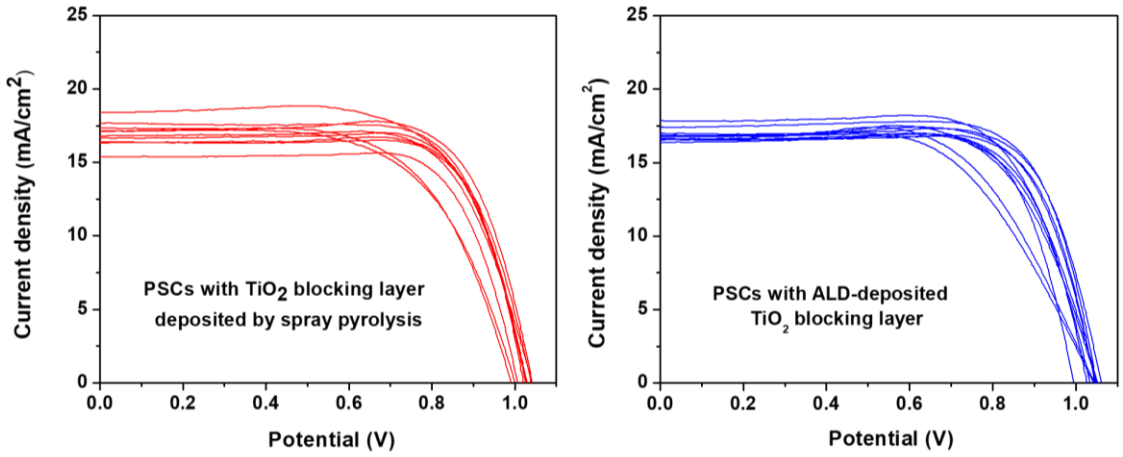

Figure 58. J-V curves of solar cells based on TiO_2 compact layers deposited by different methods: (left) spray pyrolysis and (right) ALD

A5-4. XRD patterns of the synthesized ESCs

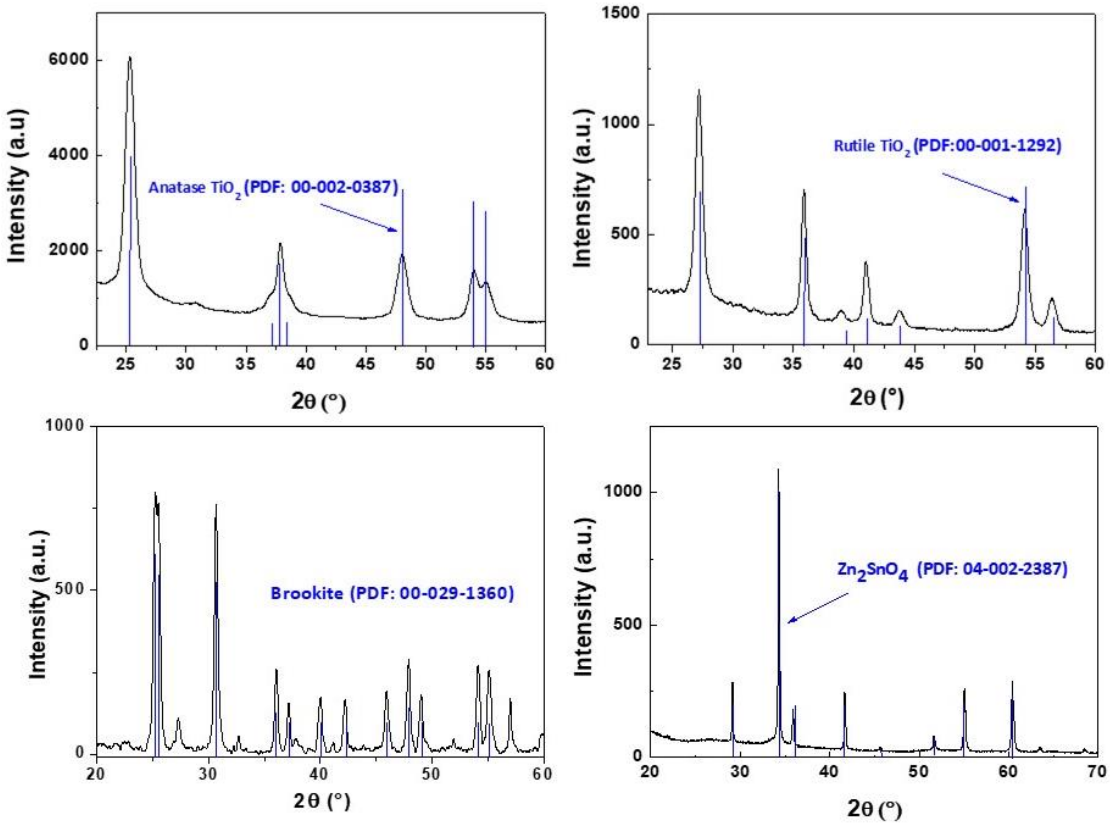

Figure 59. XRD patterns obtained for the microwave-synthesized materials: anatase, rutile, brookite and zinc stannate.

A5-5 SEM - Morphology of the ESCs

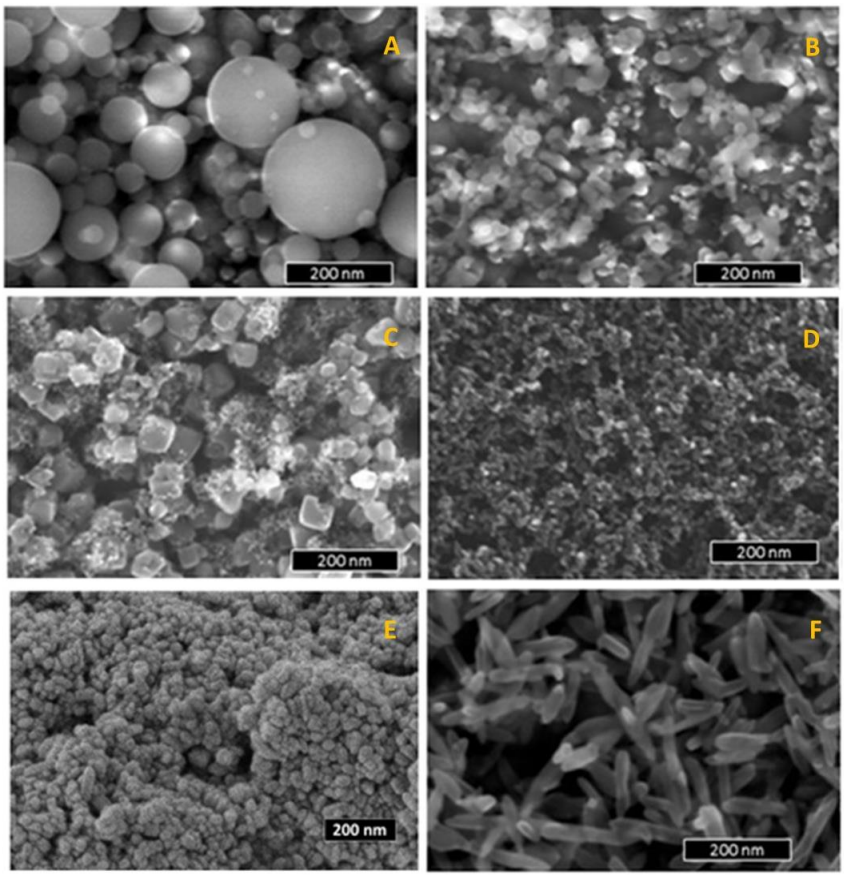

Figure 60. Morphology observed by SEM of the different electron selective contacts studied: (A) Al_2O_3, (B) ZrO_2, (C) Zn_2SnO_4, (D) Anatase (TiO_2), (E) Brookite (TiO_2) and (F) Rutile (TiO_2).

REFERENCES

1. Smil, V. " Energy Transitions: History, Requirements, Prospects". (ABC-CLIO, 2010).
2. Mcneill, J. "*Something new under the sun: an environmental history of the world in the 20th century."* (W. W. Norton & Company, 2001).
3. Mann, M. E., Bradley, R. S. & Hughes, M. K. Global-scale temperature patterns and climate forcing over the past six centuries. *Nature* **392**, 779 (1998).
4. Melillo, Jerry M. *Climate change impacts in the United States: the third national climate assessment*. Government Printing Office, 2014.
5. Intergovernmental Panel on Climate Change. G*lobal Warming of 1.5° C: An IPCC Special Report on the Impacts of Global Warming of 1.5° C Above Pre-industrial Levels*, 2018.
6. *World Energy Resources*, World Energy Council, 2016.
7. Adib, R., Murdock, H.E., Appavou, F., Brown, A., Epp, B., Leidreiter, A., Lins, C., Murdock, H.E., Musolino, E., Petrichenko, K. and Farrell, T.C., 2015. Renewables 2015 global status report. *Paris: REN21 Secretariat*.
8. SENER. Available at: https://www.gob.mx/sener.
9. *La industria solar fotovoltaica y fototérmica en México*. Proméxico, Deutsche Gesellschaft Für Internationale Zusammenarbeit (GIZ), Instituto De Energías Renovables (IER) – UNAM.
10. Memming, R. *Semiconductor Electrochemistry* (Wiley, 2001).
11. Sze, S. M. & Ng, K. K. *Physics of Semiconductor Devices* (John Wiley & Sons, 2006).
12. Nelson, J. *Physics of Solar Cells* (World Scientific Publishing Company, 2003).
13. Johnston, M. B. & Herz, L. M. Hybrid Perovskites for Photovoltaics: Charge-Carrier Recombination, Diffusion, and Radiative Efficiencies. *Accounts of Chemical Research* **49**, 146–154 (2016).
14. Basore, P. A. Defining terms for crystalline silicon solar cells. *Progress in photovoltaics: research and applications* **2**, 177–179 (1994).
15. Green, M. A.; Emery, K.; Hishikawa, Y.; Warta, W. & Dunlop, E. D. Solar cell efficiency tables (Version 45). *Progress in photovoltaics: research and applications* **23**, 1–9 (2015).
16. *Photovoltaics Report.* Fraunhofer Institute for Solar Energy Systems, ISE with support of PSE Conferences & Consulting GMBH (2019).
17. O'regan, B. & Grätzel, M. A low-cost, high-efficiency solar cell based on dye-sensitized colloidal TiO_2 films. *Nature* **353**, 737 (1991).

18. Green, M. A. & Bremner, S. P. Energy conversion approaches and materials for high-efficiency photovoltaics. *Nature materials*, **16**, 23–34 (2017).

19. Baikie, T., Fang; Y.; Kadro, J.M.; Schreyer, M.; Wei, F.; Mhaisalkar, S.G.; Graetzel, M. and White, T.J.. Synthesis and crystal chemistry of the hybrid perovskite $(CH_3NH_3)PbI_3$ for solid-state sensitised solar cell applications. *Journal of Materials Chemistry A* **1**, 5628–5641 (2013).

20. Niu, G.; Guo, X. & Wang, L. Review of recent progress in chemical stability of perovskite solar cells. *Journal of Materials Chemistry A* **3**, 8970–8980 (2015).

21. Weber, D. $CH_3NH_3PbX_3$, A Pb(II)-System with cubic perovskite structure. *Zeitschrift für Naturforschung B **33,*** 1443–1445 (1978).

22. Onoda-Yamamuro, N.; Matsuo, T., & Suga, H. Dielectric study of $CH_3NH_3PbX_3$ (X= Cl, Br, I). *Journal of Physics and Chemistry of Solids*, **53(7)**, 935-939 (1992).

23. Onoda-Yamamuro, N., Yamamuro, O., Matsuo, T., & Suga, H. pT phase relations of $CH_3NH_3PbX_3$ (X= Cl, Br, I) crystals. *Journal of Physics and Chemistry of Solids*, **53(2)**, 277-281 (1992).

24. Niemann RG, Kontos AG, Palles D, Kamitsos EI, Kaltzoglou A, Brivio F, Falaras P, Cameron PJ. Halogen effects on ordering and bonding of $CH_3NH_3^+$ in $CH_3NH_3PbX_3$ (X= Cl, Br, I) hybrid perovskites: a vibrational spectroscopic study. *The Journal of Physical Chemistry C* **120(5),** 2509-19 (2016).

25. Weller, M. T., Weber, O. J., Henry, P. F., Pumpo, M. Di & Hansen, T. C. Complete structure and cation orientation in the perovskite photovoltaic methylammonium lead iodide between 100 and 352 K . *Chemical Communications, **51(20)***, 4180–4183 (2015).

26. Xiao, Z., Dong, Q., Bi, C., Shao, Y. & Yuan, Y. Solvent Annealing of Perovskite-Induced Crystal Growth for Photovoltaic-Device Efficiency Enhancement. *Advanced Materials, **26(37)***, 6503–6509 (2014).

27. Lee, M. M., Teuscher, J., Miyasaka, T., Murakami, T. N. & Snaith, H. J. Efficient Hybrid Solar Cells Based on Meso-Superstructured Organometal Halide Perovskites. *Science* **338**, 643–647 (2012).

28. Zhao, J., Wang, A., Green, M. A., & Ferrazza, F. 19.8% efficient "honeycomb" textured multicrystalline and 24.4% monocrystalline silicon solar cells. *Applied Physics Letters*, ***73*(14)**, 1991-1993, (1998).

29. Geng, W., Zhang, L., Zhang, Y., Lau, W. & Liu, L. First-Principles Study of Lead Iodide Perovskite Tetragonal and Orthorhombic Phases for Photovoltaics. J*ournal of Physical Chemistry C*, ***118*(34)**, 19565-19571, (2014).

30. Stoumpos, C. C., Malliakas, C. D. & Kanatzidis, M. G. Semiconducting tin and lead iodide perovskites with organic cations: phase transitions, high mobilities, and near-infrared photoluminescent properties. *Inorganic chemistry*, **52**, 9019–9038 (2013).

31. Hao, F., Stoumpos, C. C., Chang, R. P. H. & Kanatzidis, M. G. Anomalous Band Gap Behavior in Mixed Sn and Pb Perovskites Enables Broadening of Absorption Spectrum in Solar Cells. *Journal of the American Chemical Society, **136*(22)**, 8094-

8099, (2014).

32. Ansari, M. I. H., Qurashi, A. & Nazeeruddin, M. K. Frontiers, opportunities, and challenges in perovskite solar cells: A critical review. *Journal of Photochemistry and Photobiology C: Photochemistry Reviews* **35**, 1–24 (2018).

33. Zhu, H., Miyata, K., Fu, Y., Wang, J. & Joshi, P. P. Screening in crystalline liquids protects energetic carriers in hybrid perovskites. *Science*, **353**, 1409–1414 (2016).

34. Frost, J. M. & Walsh, A. What Is Moving in Hybrid Halide Perovskite Solar Cells ? *Accounts of chemical research*, ***49*(3)**, 528-535, (2016).

35. Domanski, K., Roose, B., Matsui, T., Saliba, M., Turren-Cruz, S.H., Correa-Baena, J.P., Carmona, C.R., Richardson, G., Foster, J.M., De Angelis, F. and Ball, J.M. Migration of cations induces reversible performance losses over day/night cycling in perovskite solar cells. *Energy & Environmental Science,* **10**, 604–613 (2017).

36. Bi, D., Luo, J., Zhang, F. & Magrez, A. Morphology Engineering : A Route to Highly Reproducible and High Efficiency Perovskite Solar Cells. *ChemSusChem* **10(7)** 1624–1630 (2017).

37. Burschka, J., Pellet, N., Moon, S. J., Humphry-Baker, R., Gao, P., Nazeeruddin, M. K., & Grätzel, M. Sequential deposition as a route to high-performance perovskite-sensitized solar cells. *Nature* **499**, 316–319 (2013).

38. Ahn, N., Son, D. Y., Jang, I. H., Kang, S. M., Choi, M., & Park, N. G. Highly Reproducible Perovskite Solar Cells with Average Efficiency of 18.3% and Best Efficiency of 19.7% Fabricated via Lewis Base Adduct of Lead(II) Iodide. *Journal of the American Chemical Society* **137**, 8696–8699 (2015).

39. Rahimnejad, S., Kovalenko, A., Forés, S. M., Aranda, C. & Guerrero, A. Coordination Chemistry Dictates the Structural Defects in Lead Halide Perovskites. *ChemPhysChem* **17(18)**, 2795–2798 (2016).

40. Longo, G., Degen, M. J., Sessolo, M. & Bolink, H. J. Perovskite solar cells prepared by flash evaporation. *Chemical Communications **51*(34)**, 7376–7378 (2015).

41. Eperon, G.E., Habisreutinger, S.N., Leijtens, T., Bruijnaers, B.J., van Franeker, J.J., deQuilettes, D.W., Pathak, S., Sutton, R.J., Grancini, G., Ginger, D.S. and Janssen, R.A.,. The Importance of Moisture in Hybrid Lead Halide Perovskite Thin Film Fabrication. *ACS Nano* **9**, 9380–9393 (2015).

42. Aranda, C., Cristobal, C., Shooshtari, L., Li, C., Huettner, S., & Guerrero, A. Formation criteria of high efficiency perovskite solar cells under ambient conditions. *Sustainable Energy Fuels* **1**, 540–547 (2017).

43. Kojima, A., Teshima, K., Shirai, Y., & Miyasaka, T. Organometal Halide Perovskites as Visible- Light Sensitizers for Photovoltaic Cells. *ournal of the American Chemical Society* **131**, 6050–6051 (2009).

44. NREL Best Research-Cell Efficiency Chart https://www.nrel.gov/pv/cell-efficiency.html (accessed april 2019)

45. Stranks, S.D., Eperon, G.E., Grancini, G., Menelaou, C., Alcocer, M.J., Leijtens, T.,

Herz, L.M., Petrozza, A. and Snaith, H.J., 2013. Electron-hole diffusion lengths exceeding 1 micrometer in an organometal trihalide perovskite absorber. *Science **342***, 341-344 (2013).

46. Etgar L., Hole-transport material-free perovskite-based solar cells. *MRS Bulletin*, ***40*(8)**, 674-680. (2015)

47. Xia, F., Wu, Q., Zhou, P., Li, Y., Chen, X., Liu, Q., Zhu, J., Dai, S., Lu, Y. and Yang, S. Efficiency enhancement of inverted structure perovskite solar cells via oleamide doping of PCBM electron transport layer. *ACS applied materials & interfaces*, ***7*(24)**,13659-13665.(2015)

48. Zhu, Z., Bai, Y., Zhang, T., Liu, Z., Long, X., Wei, Z., Wang, Z., Zhang, L., Wang, J., Yan, F. and Yang, S. High-performance hole-extraction layer of sol-gel-processed nio nanocrystals for inverted planar perovskite solar cells. *Angewandte Chemie - International Edition* **53**, 12571–12575 (2014).

49. Yin, X., Yao, Z., Luo, Q., Dai, X., Zhou, Y., Zhang, Y., Zhou, Y., Luo, S., Li, J., Wang, N. and Lin, H. High Efficiency Inverted Planar Perovskite Solar Cells with Solution- Processed NiO. *ACS applied materials & interfaces* ***9*(3)**, 2439-2448 (2017).

50. Ye, S., Rao, H., Zhao, Z., Zhang, L., Bao, H., Sun, W., Li, Y., Gu, F., Wang, J., Liu, Z. and Bian, Z. A Breakthrough Efficiency of 19.9% Obtained in Inverted Perovskite Solar Cells by Using an Efficient Trap State Passivator Cu(thiourea)I. *Journal of the American Chemical Society* **139**, 7504–7512 (2017).

51. Wehrenfennig, C., Eperon, G. E., Johnston, M. B., Snaith, H. J. & Herz, L. M. High charge carrier mobilities and lifetimes in organolead trihalide perovskites. *Advanced Materials* **26**, 1584–1589 (2014).

52. Wang, T., Daiber, B., Frost, J.M., Mann, S.A., Garnett, E.C., Walsh, A. and Ehrler, B. Indirect to direct bandgap transition in methylammonium lead halide perovskite. *Energy & Environmental Science **10*(2)**, 509-515 (2016).

53. Ziang X, Shifeng L, Laixiang Q, Shuping P, Wei W, Yu Y, Li Y, Zhijian C, Shufeng W, Honglin D, Minghui Y. Refractive index and extinction coefficient of $CH_3NH_3PbI_3$ studied by spectroscopic ellipsometry. *Optical Materials Express* **5**, 29 (2015).

54. Bi, D., Yang, L., Boschloo, G., Hagfeldt, A. & Johansson, E. M. J. Effect of different hole transport materials on recombination in $CH_3NH_3PbI_3$ perovskite-sensitized mesoscopic solar cells. *Journal of Physical Chemistry Letters* **4**, 1532–1536 (2013).

55. Salado, M., Idigoras, J., Calio, L., Kazim, S., Nazeeruddin, M.K., Anta, J.A. and Ahmad, S. Interface Play between Perovskite and Hole Selective Layer on the Performance and Stability of Perovskite Solar Cells. *ACS Applied Materials & Interfaces* **8**, 34414–34421, (2016).

56. Juarez-Perez, E.J., Wuβler, M., Fabregat-Santiago, F., Lakus-Wollny, K., Mankel, E., Mayer, T., Jaegermann, W. and Mora-Sero, I. Role of the Selective Contacts in the Performance of Lead Halide Perovskite Solar Cells. *The Journal of Physical*

Chemistry Letters **5**, 680–685 (2014).

57. Guerrero A, Garcia-Belmonte G, Mora-Sero I, Bisquert J, Kang YS, Jacobsson TJ, Correa-Baena JP, Hagfeldt A. Properties of Contact and Bulk Impedances in Hybrid Lead Halide Perovskite Solar Cells Including Inductive Loop Elements. *The Journal of Physical Chemistry C* **120**, 8023–8032 (2016).

58. Song, J., Zheng, E., Bian, J., Wang, X.F., Tian, W., Sanehira, Y. and Miyasaka, T. Low-temperature SnO_2 -based electron selective contact for efficient and stable perovskite solar cells. *Journal of Materials Chemistry A* **3**, 10837–10844 (2015).

59. Chowdhury TH, Kaneko R, Kayesh ME, Akhtaruzzaman M, Sopian KB, Lee JJ, Islam A. Nanostructured NiO x as hole transport material for low temperature processed stable perovskite solar cells. *Materials Letters* **223**, 109–111 (2018).

60. Al-Ghamdi, A. A., Mahmoud, W. E., Yaghmour, S. J. & Al-Marzouki, F. M. Structure and optical properties of nanocrystalline NiO thin film synthesized by sol-gel spin-coating method. *Journal of Alloys and Compounds* **486**, 9–13 (2009).

61. Lin, Q., Armin, A., Nagiri, R.C.R., Burn, P.L. and Meredith, P. Electro-optics of perovskite solar cells. *Nature Photonics* **9**, 106, (2015).

62. D'innocenzo, V., Grancini, G., Alcocer, M.J., Kandada, A.R.S., Stranks, S.D., Lee, M.M., Lanzani, G., Snaith, H.J. and Petrozza, A. Excitons versus free charges in organo-lead tri-halide perovskites. *Nature communications* **5**, 3586 (2014).

63. Hirasawa, M., Ishihara, T., Goto, T., Uchida, K. & Miura, N. Magnetoabsorption of the lowest exciton in perovskite-type compound $(CH_3NH_3)PbI_3$. *Physica B: Condensed Matter* **201**, 427–430 (1994).

64. Tanaka, K., Takahashi, T., Ban, T., Kondo, T., Uchida, K. and Miura, N. Comparative study on the excitons in lead-halide-based perovskite. *Solid state communications* **127**, 619–623, (2003).

65. Ishihara, T., Optical properties of PbI-based perovskite structures. *Journal of luminescence **60***, 269-274 (1994).

66. Cadelano, M., Saba, M., Sestu, N., Sarritzu, V., Marongiu, D., Chen, F., Piras, R., Quochi, F., Mura, A. and Bongiovanni, G. Photoexcitations and Emission Processes in Organometal Trihalide Perovskites. *Perovskite Materials-Synthesis, Characterisation, Properties, and Applications*. IntechOpen, (2016).

67. Herz, L. M. Charge-Carrier Dynamics in Organic-Inorganic Metal Halide Perovskites. *Annual review of physical chemistry **67***, 65-89. (2016)

68. Piatkowski, P., Cohen, B., Ramos, J. & Nunzio, D. Direct monitoring of ultrafast electron and hole dynamics in perovskite solar cells. *Physical Chemistry Chemical Physics* **17**, 14674–14684 (2015).

69. Wetzelaer, G. A. H., Scheepers, M., Sempere, A. M. & Momblona, C. Trap-Assisted Non-Radiative Recombination in Organic-Inorganic Perovskite Solar Cells. *Advanced Materials* **27**, 1837–1841 (2015).

70. Noel, N.K., Stranks, S.D., Abate, A., Wehrenfennig, C., Guarnera, S., Haghighirad, A.A., Sadhanala, A., Eperon, G.E., Pathak, S.K., Johnston, M.B. and Petrozza, A.

Lead-free organic–inorganic tin halide perovskites for photovoltaic applications. *Energy & Environmental Science* **7**, 3061–3068 (2014).

71. McMeekin, D.P., Sadoughi, G., Rehman, W., Eperon, G.E., Saliba, M., Hörantner, M.T., Haghighirad, A., Sakai, N., Korte, L., Rech, B. and Johnston, M.B. A mixed-cation lead mixed-halide perovskite absorber for tandem solar cells. *Science* **351**, 151–155 (2016).

72. Noel, N.K., Stranks, S.D., Abate, A., Wehrenfennig, C., Guarnera, S., Haghighirad, A.A., Sadhanala, A., Eperon, G.E., Pathak, S.K., Johnston, M.B. and Petrozza, A. High-efficiency solution-processed perovskite solar cells with millimeter-scale grains. *Science* **347**, 522–525 (2015).

73. Yamada, Y., Nakamura, T., Endo, M., Wakamiya, A. & Kanemitsu, Y. Photocarrier recombination dynamics in perovskite $CH_3NH_3PbI_3$ for solar cell applications. *Journal of the American Chemical Society* **136**, 11610–3 (2014).

74. Milot, R. L., Eperon, G. E., Snaith, H. J., Johnston, M. B. & Herz, L. M. Temperature-Dependent Charge-Carrier Dynamics in $CH_3NH_3PbI_3$ Perovskite Thin Films. *Advanced Functional Materials* 6218–6227 (2015).

75. Wehrenfennig, C., Liu, M., Snaith, H. J., Johnston, M. B. & Herz, L. M. Charge-carrier dynamics in vapour-deposited films of the organolead halide perovskite $CH_3NH_3PbI_{3-x}Cl_x$. *Energy & Environmental Science* **7**, 2269–2275 (2014).

76. Pockett, A., Eperon, G.E., Sakai, N., Snaith, H.J., Peter, L.M. and Cameron, P.J. Microseconds, milliseconds and seconds: Deconvoluting the dynamic behaviour of planar perovskite solar cells. *Physical Chemistry Chemical Physics* **19**, 5959–5970 (2017).

77. De Bastiani, M., Dell'Erba, G., Gandini, M., D'Innocenzo, V., Neutzner, S., Kandada, A.R.S., Grancini, G., Binda, M., Prato, M., Ball, J.M. and Caironi, M. Ion migration and the role of preconditioning cycles in the stabilization of the J-V characteristics of inverted hybrid perovskite solar cells. *Advanced Energy Materials* **6**, 1–9 (2016).

78. Kim, H. S. & Park, N. G. Parameters affecting I-V hysteresis of CH3NH3PbI3 perovskite solar cells: Effects of perovskite crystal size and mesoporous TiO2 layer. *Journal of Physical Chemistry Letters* **5**, 2927–2934 (2014).

79. Miller, D.W., Eperon, G.E., Roe, E.T., Warren, C.W., Snaith, H.J. and Lonergan, M.C. Defect states in perovskite solar cells associated with hysteresis and performance. *Applied Physics Letters **109***, 153902, (2016).

80. Contreras, L., Idígoras, J., Todinova, A., Salado, M., Kazim, S., Ahmad, S. and Anta, J.A. Specific cation interactions as the cause of slow dynamics and hysteresis in dye and perovskite solar cells: a small-perturbation study. *Physical Chemistry Chemical Physics.* **18**, 31033–31042 (2016).

81. Sanchez, R.S., Gonzalez-Pedro, V., Lee, J.W., Park, N.G., Kang, Y.S., Mora-Sero, I. and Bisquert, J. Slow Dynamic Processes in Lead Halide Perovskite Solar Cells. Characteristic Times and Hysteresis. The journal of physical chemistry letters ***5***, 2357-2363, (2014).

82. Frost, J.M., Butler, K.T., Brivio, F., Hendon, C.H., Van Schilfgaarde, M. and Walsh, A. Atomistic Origins of High-Performance in Hybrid Halide Perovskite Solar Cells. (2014). *Nano letters* ***14*****(5)**, pp.2584-2590. 2014

83. Singh, S., Li, C., Panzer, F., Narasimhan, K.L., Graeser, A., Gujar, T.P., Köhler, A., Thelakkat, M., Huettner, S. and Kabra, D. Effect of Thermal and Structural Disorder on the Electronic Structure of Hybrid Perovskite Semiconductor $CH_3NH_3PbI_3$. *The journal of physical chemistry letters* ***7***, 3014-3021. (2016).

84. Green, M. A., Ho-baillie, A. & Snaith, H. J. The emergence of perovskite solar cells. *Nature Photonics* **8**, 506–514 (2014).

85. Rivkin, B., Fassl, P., Sun, Q., Taylor, A.D., Chen, Z. and Vaynzof, Y. Effect of Ion Migration-Induced Electrode Degradation on the Operational Stability of Perovskite Solar Cells. *ACS Omega* **3**, 10042–10047 (2018).

86. Shao, Y., Fang, Y., Li, T., Wang, Q., Dong, Q., Deng, Y., Yuan, Y., Wei, H., Wang, M., Gruverman, A. and Shield, J. Grain boundary dominated ion migration in polycrystalline organic-inorganic halide perovskite films. *Energy and Environmental Science* **9**, 1752–1759 (2016).

87. Li, X., Irvine, S. J. C., Mcgehee, M. D. & Barnes, R. F. Environmental Science Interpretation of inverted photocurrent transients in organic lead halide perovskite solar cells : proof of the field screening by mobile ions and determination of the space charge layer widths *Energy & Environmental Science* ***10***, 192–204 (2017).

88. Eames, C., Frost, J.M., Barnes, P.R., O'regan, B.C., Walsh, A. and Islam, M.S. Ionic transport in hybrid lead iodide perovskite solar cells. *Nature communications* ***6***, 7497. (2015).

89. hang, Y., Liu, M., Eperon, G.E., Leijtens, T.C., McMeekin, D., Saliba, M., Zhang, W., de Bastiani, M., Petrozza, A., Herz, L.M. and Johnston, M.B. Charge selective contacts, mobile ions and anomalous hysteresis in organic–inorganic perovskite solar cells. *Materials Horizons* ***2***, 315-322 (2015).

90. Azpiroz, J. M., Mosconi, E., Bisquert, J. & De Angelis, F. Defect migration in methylammonium lead iodide and its role in perovskite solar cell operation. *Energy and Environmental Science* **8**, 2118–2127 (2015).

91. Yuan, Y. & Huang, J. Ion Migration in Organometal Trihalide Perovskite and Its Impact on Photovoltaic E ffi ciency and Stability. *Accounts of chemical research, 49*, 286-293. (2016).

92. Reenen, S. Van, Kemerink, M. & Snaith, H. J. Modeling Anomalous Hysteresis in Perovskite Solar Cells. *The journal of physical chemistry letters* **6**, 3808-3814 (2015).

93. Snaith, H.J., Abate, A., Ball, J.M., Eperon, G.E., Leijtens, T., Noel, N.K., Stranks, S.D., Wang, J.T.W., Wojciechowski, K. and Zhang, W. Anomalous hysteresis in perovskite solar cells. *Journal of Physical Chemistry Letters* **5**, 1511–1515 (2014).

94. Contreras-Bernal, L., Salado, M., Todinova, A., Calio, L., Ahmad, S., Idígoras, J. and Anta, J.A. Origin and Whereabouts of Recombination in Perovskite Solar Cells. *Journal of Physical Chemistry C* **121**, 9705–9713 (2017).

95. Richardson, G., O'Kane, S.E., Niemann, R.G., Peltola, T.A., Foster, J.M., Cameron, P.J. and Walker, A.B. Can slow-moving ions explain hysteresis in the current–voltage curves of perovskite solar cells? *Energy & Environmental Science* **9**, 1476–1485 (2016).

96. Idígoras, J., Contreras-Bernal, L., Cave, J.M., Courtier, N.E., Barranco, Á., Borras, A., Sánchez-Valencia, J.R., Anta, J.A. and Walker, A.B. The Role of Surface Recombination on the Performance of Perovskite Solar Cells: Effect of Morphology and Crystalline Phase of TiO_2 Contact. *Advanced Materials Interfaces* **5**, 1801076 (2018).

97. Grätzel M. Solar Cells Based on Sol–Gel Films. Handbook of Sol-Gel Science and Technology. Springer, Cham (2017)

98. Reyes-Coronado, D., Rodríguez-Gattorno, G., Espinosa-Pesqueira, M.E., Cab, C., de Coss, R.D. and Oskam,. Phase-pure TiO_2 nanoparticles: anatase , brookite and rutile. *Nanotechnology* **19(14)**, 145605. (2008)

99. Ruiz-León, D., Avila, R. E. & Venegas, C. J. Synthesis and electrical characterization of zinc stannate (ZTO) prepared by hydrothermal method. *Journal of the Chilean Chemical Society* **60**, 3029–3032 (2015).

100. Aharon, S., Dymshits, A., Rotem, A. & Etgar, L. Temperature dependence of hole conductor free formamidinium lead iodide perovskite based solar. J*ournal of Materials Chemistry A* ***3*****(17)**, 9171–9178 (2015).

101. Aharon, S., Gamliel, S., Cohen, B. El & Etgar, L. Depletion region effect of highly efficient hole conductor free CH_3NH_3 PbI_3 perovskite solar cells. *Physical Chemistry Chemical Physics*, **16**, 10512–10518 (2014).

102. Christians, J. A., Fung, R. C. M. & Kamat, P. V. An Inorganic Hole Conductor for Organo-Lead Halide Perovskite Solar Cells. Improved Hole Conductivity with Copper Iodide. *Journal of the American Chemical Society* **136**, 758–764 (2014).

103. Pydzińska, K., Karolczak, J., Kosta, I., Tena-Zaera, R., Todinova, A., Idígoras, J., Anta, J.A. and Ziółek, M. Determination of Interfacial Charge-Transfer Rate Constants in Perovskite Solar Cells. *ChemSusChem* **9**, 1647–1659 (2016).

104. Ravishankar, S., Gharibzadeh, S., Roldán-Carmona, C., Grancini, G., Lee, Y., Ralaiarisoa, M., Asiri, A.M., Koch, N., Bisquert, J. and Nazeeruddin, M.K. Influence of Charge Transport Layers on Open-Circuit Voltage and Hysteresis in Perovskite Solar Cells. *Joule* **2**, 788–798 (2018).

105. Kim, H.-S. & Park, N.-G. Parameters Affecting I–V Hysteresis of $CH_3NH_3PbI_3$ Perovskite Solar Cells: Effects of Perovskite Crystal Size and Mesoporous TiO_2 Layer. *The Journal of Physical Chemistry Letters* **5**, 2927–2934 (2014).

106. Park, N. G., Lagemaat, J. van de & Frank, A. J. Comparison of dye-sensitized rutile- and anatase-based TiO2 solar cells. *Journal of Physical Chemistry B* **104**, 8989–8994 (2000).

107. Wojciechowski, K., Stranks, S.D., Abate, A., Sadoughi, G., Sadhanala, A., Kopidakis, N., Rumbles, G., Li, C.Z., Friend, R.H., Jen, A.K.Y. and Snaith, H.J. Heterojunction Modification for Highly Efficient Organic–Inorganic Perovskite

Solar Cells. *ACS Nano* **8**, 12701–12709 (2014).

108. Manser, J. S., Christians, J. A. & Kamat, P. V. Intriguing Optoelectronic Properties of Metal Halide Perovskites. *Chemical Reviews* (2016).

109. Chen, B., Yang, M., Priya, S. & Zhu, K. Origin of J–V Hysteresis in Perovskite Solar Cells. *The Journal of Physical Chemistry Letters* **7**, 905–917 (2016).

110. Ravishankar S, Almora O, Echeverría-Arrondo C, Ghahremanirad E, Aranda C, Guerrero A, Fabregat-Santiago F, Zaban A, Garcia-Belmonte G, Bisquert J. Surface Polarization Model for the Dynamic Hysteresis of Perovskite Solar Cells. *The Journal of Physical Chemistry Letters* **8**, 915–921 (2017).

111. Contreras-Bernal, L., Salado, M., Todinova, A., Calio, L., Ahmad, S., Idígoras, J. and Anta, J.A. Origin and Whereabouts of Recombination in Perovskite Solar Cells. *Journal of Physical Chemistry C* **121**, 9705–9713 (2017).

112. Leong WL, Ooi ZE, Sabba D, Yi C, Zakeeruddin SM, Graetzel M, Gordon JM, Katz EA, Mathews N. Identifying Fundamental Limitations in Halide Perovskite Solar Cells. *Advanced Materials* **28**, 2439–2445 (2016).

113. Zarazua, I., Han, G., Boix, P.P., Mhaisalkar, S., Fabregat-Santiago, F., Mora-Seró, I., Bisquert, J. and Garcia-Belmonte, G. Surface Recombination and Collection Efficiency in Perovskite Solar Cells from Impedance Analysis. *The Journal of Physical Chemistry Letters* **7**, 5105–5113 (2016).

114. Todinova, A., Contreras-Bernal, L., Salado, M., Ahmad, S., Morillo, N., Idígoras, J. and Anta, J.A. Towards universal approach to the analysis of impedance spectra of perovskite solar cells. Equivalent circuits and empirical analysis. *ChemElectroChem **4***, 2891-2901 (2017)

115. Tress, W., Yavari, M., Domanski, K., Yadav, P., Niesen, B., Baena, J.P.C., Hagfeldt, A. and Graetzel, M. Interpretation and evolution of open-circuit voltage, recombination, ideality factor and subgap defect states during reversible light-soaking and irreversible degradation of perovskite solar cells. *Energy & Environmental Science* **11**, 155–165 (2018).

116. Kirchartz, T., Krückemeier, L. & Unger, E. L. Research Update: Recombination and open-circuit voltage in lead-halide perovskites. *APL Materials* **6**, 100702 (2018).

117. Li, Y., Zhao, Y., Chen, Q., Yang, Y., Liu, Y., Hong, Z., Liu, Z., Hsieh, Y.T., Meng, L., Li, Y. and Yang, Y. Multifunctional Fullerene Derivative for Interface Engineering in Perovskite Solar Cells. *Journal of the American Chemical Society* **137**, 15540–15547 (2015).

118. Jeng, J.Y., Chiang, Y.F., Lee, M.H., Peng, S.R., Guo, T.F., Chen, P. and Wen, T.C $CH_3NH_3PbI_3$ perovskite/fullerene planar-heterojunction hybrid solar cells. *Advanced Materials **25*****(27)**, 3727-3732 (2013).

119. Chen, C., Zhang, S., Wu, S., Zhang, W., Zhu, H., Xiong, Z., Zhang, Y. and Chen, W. Effect of BCP buffer layer on eliminating charge accumulation for high performance of inverted perovskite solar cells. *RSC Advances* **7**, 35819–35826 (2017).

120. Yuan, D.X., Yuan, X.D., Xu, Q.Y., Xu, M.F., Shi, X.B., Wang, Z.K. and Liao, L.S.

A solution-processed bathocuproine cathode interfacial layer for high-performance bromine-iodine perovskite solar cells. *Physical Chemistry Chemical Physics* **17**, 26653–26658 (2015).

121. Sun, S., Salim, T., Mathews, N., Duchamp, M., Boothroyd, C., Xing, G., Sum, T.C. and Lam, Y.M. The origin of high efficiency in low-temperature solution-processable bilayer organometal halide hybrid solar cells. *Energy & Environmental Science* **7**, 399–407 (2014).

122. Liu, X., Cheng, Y., Liu, C., Zhang, T., Zhang, N., Zhang, S., Chen, J.S., Xu, Q., Ouyang, J. and Gong, H. 20.7% Highly Reproducible Inverted Planar Perovskite Solar Cells with Enhanced Fill Factor and Eliminated Hysteresis. *Energy & Environmental Science* **12**, 1622-1633 (2019)

123. Heo, J. H., Han, H. J., Kim, D., Ahn, T. K. & Im, S. H. Hysteresis-less inverted $CH_3NH_3PbI_3$ planar perovskite hybrid solar cells with 18.1% power conversion efficiency. *Energy & Environmental Science* **8**, 1602–1608 (2015).

124. Qin, P., Tanaka, S., Ito, S., Tetreault, N., Manabe, K., Nishino, H., Nazeeruddin, M.K. and Grätzel, M. Inorganic hole conductor-based lead halide perovskite solar cells with 12.4% conversion efficiency. *Nature communications* **5**, 3834 (2014).

125. Christians, J. A., Fung, R. C. M. & Kamat, P. V. An inorganic hole conductor for organo-lead halide perovskite solar cells. Improved hole conductivity with copper iodide. *Journal of the American Chemical Society* **136**, 758–764 (2013).

126. Hu, Z., Miao, J., Liu, M., Yang, T., Liang, Y., Goto, O. and Meng, H. Enhanced performance of inverted perovskite solar cells using solution-processed carboxylic potassium salt as cathode buffer layer. *Organic Electronics: physics, materials, applications* **45**, 97–103 (2017).

127. Wang, K.C., Jeng, J.Y., Shen, P.S., Chang, Y.C., Diau, E.W.G., Tsai, C.H., Chao, T.Y., Hsu, H.C., Lin, P.Y., Chen, P. and Guo, T.F. p-type Mesoscopic Nickel Oxide/ Organometallic Perovskite Heterojunction Solar Cells. *Scientific reports* **4** 4756. (2014).

128. Jeng, J.Y., Chen, K.C., Chiang, T.Y., Lin, P.Y., Tsai, T.D., Chang, Y.C., Guo, T.F., Chen, P., Wen, T.C. and Hsu, Y.J. Nickel oxide electrode interlayer in $CH_3NH_3PbI_3$ perovskite/PCBM planar-heterojunction hybrid solar cells. *Advanced Materials* **26**, 4107–4113 (2014).

129. Xie, Y., Lu, K., Duan, J., Jiang, Y., Hu, L., Liu, T., Zhou, Y. and Hu, B. Enhancing Photovoltaic Performance of Inverted Planar Perovskite Solar Cells by Cobalt-Doped Nickel Oxide Hole Transport Layer. *ACS applied materials & interfaces* ***10*****(16)**, 14153-14159 (2018).

130. Tang, J., Jiao, D., Zhang, L., Zhang, X., Xu, X., Yao, C., Wu, J. and Lan, Z. High-performance inverted planar perovskite solar cells based on e ffi cient hole-transporting layers from well-crystalline NiO nanocrystals. *Solar Energy* **161**, 100–108 (2018).

131. Kwon, U., Kim, B., Nguyen, D. C., Park, J. & Ha, N. Y. Solution-Processible Crystalline NiO Nanoparticles for High- Performance Planar Perovskite Photovoltaic

Cells. *Scientific reports* ***6***, 30759. (2016).

132. Hu, Z., Chen, D., Yang, P., Yang, L., Qin, L., Huang, Y. and Zhao, X . Applied Surface Science Sol-gel-processed yttrium-doped NiO as hole transport layer in inverted perovskite solar cells for enhanced performance. *Applied Surface Science* **441**, 258–264 (2018).

133. Zhang, H., Cheng, J., Lin, F., He, H., Mao, J., Wong, K.S., Jen, A.K.Y. and Choy, W.C. Pinhole-Free and Surface-Nanostructured NiO. A*CS nano* ***10*****(1)**, pp.1503-1511. (2016).

134. Yang, Q., Sha, J., Ma, X. & Yang, D. Synthesis of NiO nanowires by a sol-gel process. *Materials Letters* **59**, 1967–1970 (2005).

135. Corani, A., Li, M., Shen, P., Chen, P. & Guo, T. Ultrafast Dynamics of Hole Injection and Recombination in Organometal Halide Perovskite Using Nickel Oxide as p-Type Contact Electrode. *The journal of physical chemistry letters* **7(7)**, 1096-1101 (2016).

136. Zhang, H., Cheng, J., Lin, F., He, H., Mao, J., Wong, K.S., Jen, A.K.Y. and Choy, W.C.. Measurement and modelling of dark current decay transients in perovskite solar cells. *Journal of Materi. als Chemistry C* **5**, 452–462 (2017).

137. Xu, X., Liu, Z., Zuo, Z., Zhang, M., Zhao, Z., Shen, Y., Zhou, H., Chen, Q., Yang, Y. and Wang, M. Hole Selective NiO Contact for Efficient Perovskite Solar Cells with Carbon Electrode. *Nano Letters* **15**, 2402–2408 (2015).

138. Wang KC, Shen PS, Li MH, Chen S, Lin MW, Chen P, Guo TF. Low-temperature sputtered nickel oxide compact thin film as effective electron blocking layer for mesoscopic NiO/$CH_3NH_3PbI_3$ perovskite heterojunction solar cells. *ACS Applied Materials and Interfaces* **6**, 11851–11858 (2014).

139. Shao, Y., Xiao, Z., Bi, C., Yuan, Y. & Huang, J. Origin and elimination of photocurrent hysteresis by fullerene passivation in $CH_3NH_3PbI_3$ planar heterojunction solar cells. *Nature Communications* **5**, 1–7 (2014).

140. Bryant, D., Wheeler, S., O'Regan, B.C., Watson, T., Barnes, P.R., Worsley, D. and Durrant, J. Observable Hysteresis at Low Temperature in 'hysteresis Free' Organic-Inorganic Lead Halide Perovskite Solar Cells. *Journal of Physical Chemistry Letters* **6**, 3190–3194 (2015).

141. Rong, Y., Hu, Y., Ravishankar, S., Liu, H., Hou, X., Sheng, Y., Mei, A., Wang, Q., Li, D., Xu, M. and Bisquert, J. Tunable hysteresis effect for perovskite solar cells. *Energy and Environmental Science* **10**, 2383–2391 (2017).

142. Erdenebileg, E., Scholz, L. E., Hofacker, A., Koerner, C. & Leo, K. Very Small Inverted Hysteresis in Vacuum-Deposited Mixed Organic–Inorganic Hybrid Perovskite Solar Cells. *Energy Technology* **5**, 1606–1611 (2017).

143. Wu F, Pathak R, Chen K, Wang G, Bahrami B, Zhang WH, Qiao Q. Inverted Current −Voltage Hysteresis in Perovskite Solar Cells. ACS Energy Letters **3**, 2457-2460 (2018).